

A FORMAL EVALUATION OF STORM TYPE VERSUS STORM MOTION

A Thesis presented to the faculty of the Graduate School at the
University of Missouri-Columbia

In Partial Fulfillment
of the Requirements for the Degree
Master of Science

by
JOSÉ MIRANDA

Dr. Neil I. Fox, Thesis Supervisor

MAY 2008

The undersigned, appointed by the dean of the Graduate School, have examined the thesis entitled

A FORMAL EVALUATION OF STORM TYPE VERSUS STORM MOTION

presented by José Miranda,

a candidate for the degree of master of science,

and hereby certify that, in their opinion, it is worthy of acceptance.

Assistant Professor Neil I. Fox

Associate Professor Anthony R. Lupo

Professor Christopher K. Wikle

DEDICATED TO NORMA BERRY

JUNE 14, 1924-DECEMBER 2, 2007

AN INSPIRATION TO THOSE WHO SHE BLESSED WITH HER PRESENCE

ACKNOWLEDGEMENTS

I would like to start off by thanking the Department of atmospheric science at the University of Missouri-Columbia. My advisor, Neil I. Fox, also deserves many thanks in providing me the guidance I needed to complete this publication and giving me the opportunity to continue my education. Also, many thanks go to Dr. Patrick Market and Dr. Anthony Lupo for teaching me what I know today in the field of atmospheric science as well as spending their time and effort solving problems, both small and large, that have come up along the way.

I would also like to acknowledge the organizations that funded this research. Thanks go to the National Science Foundation and the University of Missouri-Columbia Research Council for the approval to conduct research on the topic of thunderstorm motion.

Furthermore, I would not have written this thesis without the help of many undergraduate and graduate students within the department of atmospheric science. Steven Lack's guidance, especially with his statistical classifier, George Limpert's guidance with WDSS-II and an assortment of other weather and non-weather related programs and banter, Ali Koleiny and Chris Melick's uncanny ability to distract me from the rigors of my research, Rachel Redburn, Willie

Gilmore, Mark Dahmer, Christopher Foltz, Brian Pettegrew, Larry Smith, Amy Becker, Melissa Chesser, and Neville Miller, among others, all deserve thanks for providing needed insight, and reminding me why I want to enter this profession.

Most of all, the largest amount of thanks and appreciation go out to my family and friends. My undergraduate mentor, Christopher Straub, my high-school mentor, Michael Dager, and my college cross-country teammates at Elizabethtown. My best friend, Adam Arker, who has given me the inspiration to "go for it", and genuinely love what you do. My family, my mother, father, brother, there will never be enough thanks and gratitude that will ever be expressed from me for your love, support, and advice in making major decisions in my life. There were times when it was really, really tough and times when I wanted to quit but you were there. I love you all.

Finally, this thesis is dedicated to the two people who are my life, my world, and the reason you are reading this sentence right now, my wife Melissa and daughter Cheyenne. I owe everything I have done, and give credit for being able to make it through graduate school, to these two wonderful people. It was hard to become a parent and as a couple complete our education, but it is of the utmost importance to do so. No one else can sympathize with my

experiences like Melissa, and it is her will, thirst, and quest for knowledge that inspires me every day. I will be there for you like you were for me when you write your master's thesis. I love you!

Chey-Chey, daddy wrote a big book! Maybe someday you will understand. If you don't, that's cool too.

COMMITTEE IN CHARGE OF CANDIDACY

Assistant Professor Neil I. Fox
Chairperson and Advisor

Associate Professor Anthony R. Lupo

Associate Professor Christopher K. Wikle

TABLE OF CONTENTS

ACKNOWLEDGEMENTS.....	ii
COMMITTEE IN CHARGE OF CANDIDACY.....	v
LIST OF FIGURES.....	ix
LIST OF TABLES.....	xiv
ABSTRACT.....	xvi
CHAPTER 1: INTRODUCTION	1
1.1 STATEMENT OF THESIS.....	2
CHAPTER 2: LITERATURE REVIEW.....	5
2.1 FORECASTING STORM MOTION.....	5
2.2 STORM TYPE CLASSIFICATION.....	13
2.3 FORECASTING SUPERCELL MOTION.....	14
2.4 FORECASTING SQUALL-LINE MOTION.....	17
2.5 FORECASTING MULTI-CELL MOTION.....	20
CHAPTER 3: METHODOLOGY.....	25
3.1 STUDY FOCUS.....	25
3.1.1 Area of Study.....	25
3.1.2 Selection of Storm Cells.....	26
3.2 DATA.....	28
3.3 PROCEDURE.....	29
CHAPTER 4: CASE STUDIES.....	32
4.1 SUPERCELL EVENTS.....	32
4.1.1 12 March 2006: Pleasant Hill, MO region.....	32

4.1.2	2-3 April 2006: Little Rock, AR & Memphis, TN regions.....	33
4.1.3	21-22 April 2007: Amarillo, TX region.....	34
4.1.4	28-29 March 2007: Amarillo, TX region.....	35
4.1.5	4 May 2003: Pleasant Hill, MO region.....	36
4.1.6	7 April 2006: Memphis, TN region.....	37
4.2	SQUALL-LINE EVENTS.....	38
4.2.1	19-20 July 2006: Saint Charles, MO region.....	38
4.2.2	21 July 2006: Saint Charles, MO region.....	39
4.2.3	9 July 2004: Hastings, NE region.....	40
4.2.4	2-3 May 2003: Atlanta, GA region.....	41
4.2.5	19 October 2004: Nashville, TN region.....	42
4.2.6	6 November 2005: Saint Charles, MO region.....	43
4.3	MULTI-CELL EVENTS.....	44
4.3.1	6-7 August 2005: Fort Worth, TX region.....	44
4.3.2	19-20 June 2006: Jackson, MS region.....	45
4.3.3	2 July 2006: Tampa Bay, FL region.....	46
4.3.4	28 July 2006: State College, PA region.....	47
4.3.5	5 July 2004: Baltimore, MD & Washington, DC regions.....	48
4.3.6	13 June 2004: Memphis, TN region.....	49
4.4	SUMMARY OF CASES.....	49
CHAPTER 5: RESULTS.....		51
5.1	CLASSIFICATION OF CELLS WITH PARAMETER INFORMATION BY STATISTICAL CLASSIFIER.....	51
5.2	COMPARISON OF PARAMETERS BY CELL TYPE.....	56

5.3 STORM SPEED.....	63
5.4 PERFORMANCE OF ISOTHERMAL WIND METHOD.....	65
5.4.1 Direction of Motion of Supercells.....	65
5.4.2 Direction of Motion of Linear Convective Systems.....	70
5.4.3 Direction of Motion of Multicells.....	73
5.5 COMPARISON OF ISOTHERMAL WIND METHOD VERSUS OTHER PREDICTIVE CELL METHODS.....	76
5.6 ERRORS.....	83
5.7 DISCUSSION.....	87
CHAPTER 6: SUMMARY AND CONCLUSIONS.....	91
6.1 SUMMARY.....	91
6.2 FUTURE WORK.....	94
APPENDIX A.....	97
APPENDIX B.....	107
REFERENCES.....	111

LIST OF FIGURES

Figure	Page
Figure 2.1 Example of storm data runs-2D case. Shading indicates grid points where the reflectivity exceeds T_z (from Dixon and Weiner, 1993).....	7
Figure 2.2 Storm merger (from Dixon and Weiner, 1993).....	9
Figure 2.3 Illustration of the advective component (V_{CL}) and the propagation component ($V_{PROP} = -V_{LLJ}$) as the vector sum of MBE movement (V_{MBE}). The angles ψ and ϕ are used in the calculation of V_{MBE} and the dashed lines are the 850-300 mb thickness pattern to the environmental flow (from Corfidi et al. 1996).....	19
Figure 2.4 Idealized depiction of squall-line formation (from Bluestein and Jain, 1985).....	20
Figure 2.5 Thermodynamic stability and wind shear parameters for storms documented in Marwitz (1972).....	23
Figure 2.6 Multi-cell motion with the environmental winds (Marwitz 1972)...	24
Figure 2.7 Multi-Cell motion to the right of the environmental winds (Marwitz 1972).....	24
Figure 2.8 Multi-cell motion to the left of the environmental winds (Marwitz 1972).....	24
Figure 3.1 Radar site locations (thirteen sites) for the eighteen cases in the study. Locations are approximate.....	30
Figure 4.1 A radar composite reflectivity image from the National Weather Service EAX radar site at 2045 UTC on 12 March 2006. The radar site is located southeast of Kansas City near Jackson County, MO. The "five-state" supercell is the cell furthest to the south in the image, along the Kansas/Missouri border.....	34

Figure 4.2 A radar composite reflectivity image from the National Weather Service NQA radar site at 2347 UTC on 2 April 2006. The supercell that hit the town of Caruthersville, MO is indicated with the letter "A". The radar site is located northeast of Memphis near Shelby County, TN.....	35
Figure 4.3 A radar composite reflectivity image from the National Weather Service AMA radar site at 0032 UTC on 22 April 2007. The radar site is located northwest of Amarillo near Potter County, TX.....	36
Figure 4.4 A radar composite reflectivity image from the National Weather Service AMA radar at 0016 UTC on 29 March 2007. The arrow points to the left-moving supercell.....	37
Figure 4.5 A radar composite reflectivity image from the National Weather Service TWX radar site at 2135 UTC on 4 May 2003. The left-moving supercell in this case is indicated with the letter "B". The radar site is located south of Topeka near Wabaunsee County, KS.....	38
Figure 4.6 A radar composite reflectivity image from the National Weather Service NQA radar site at 1728 UTC on 7 April 2006.....	39
Figure 4.7 A radar composite reflectivity image from the National Weather Service LSX radar site at 0006 UTC on 20 July 2006. The radar site is located southwest on Saint Louis near Saint Charles County, MO.....	40
Figure 4.8 A radar composite reflectivity image from the National Weather Service LSX radar site at 1509 UTC on 21 July 2006.....	41
Figure 4.9 A radar composite reflectivity image from the National Weather Service UEX radar site at 0443 UTC on 9 July 2004. The radar site is located south of Hastings near Webster County, NE.....	42
Figure 4.10 A radar composite reflectivity image from the National Weather Service FFC radar site at 0111 UTC on 3 May 2003. The radar site is located southeast of Atlanta near Henry County, GA.....	43
Figure 4.11 A radar composite reflectivity image from the National Weather Service OHX radar site at 0415 UTC on 19 October 2004. The radar site is located northwest of Nashville near Robertson County, TN.....	44
Figure 4.12 A radar composite reflectivity image from the National Weather Service LSX radar site at 0244 UTC on 6 November 2005.....	45
Figure 4.13 A radar composite reflectivity image from the National Weather Service FWS radar site at 2133 UTC on 6 August 2005. The radar site is located south of Fort Worth near Johnson County, TX.....	46

Figure 4.14 A radar composite reflectivity image from the National Weather Service DGX radar site at 2030 UTC on 19 June 2006. The radar site is located east of Jackson near Brandon in Rankin County, MS.....	47
Figure 4.15 A radar composite reflectivity image from the National Weather Service TBW radar site at 1829 UTC on 2 July 2006. The main outflow boundary is indicated with arrows. The radar site is located south of Tampa in Hillsborough County, Florida.....	48
Figure 4.16 A radar composite reflectivity image from the National Weather Service CCX radar site at 1659 UTC on 28 July 2006. The radar is located west of State College in Centre County, PA.....	49
Figure 4.17 A radar composite reflectivity image from the National Weather Service LWX radar site at 1948 UTC on 5 July 2004. The two cells mentioned in the case study description are indicated with arrows. The radar is located northwest of Sterling near Loudoun County, VA.....	50
Figure 5.1 Cell classification tree for the 53 cells in the study.....	53
Figure 5.2 A box-and-whisker plot of Mean-Layer Convective Available Potential Energy (MLCAPE) values for cells tested in the study (n=53). Y-axis indicates MLCAPE values in J kg^{-1}	57
Figure 5.3 A box-and-whisker plot of Vorticity Generation Parameter (VGP) values for cells tested in the study (n=53). Y-axis indicates VGP values.....	58
Figure 5.4 A box-and-whisker plot of 0-3 kilometer Storm Relative Helicity values for cells tested in the study (n=53). Y-axis indicates SRH values (m^2s^{-2}).....	60
Figure 5.5 A box-and-whisker plot of mean 0-6 kilometer wind shear values for cells tested in the study (n=53). Y-axis indicates wind shear values (kts).....	61
Figure 5.6 Illustration of velocities of cells tested in the study versus Isothermal winds. Y=X trendline indicates the equality of the -20, -10, and 0°C isothermal wind velocities to supercell, linear, or multicell velocities respectively.....	64
Figure 5.7 Same as Figure 5.14 for A) supercells, B) linear cells, and C) multicells.....	65
Figure 5.8 A comparison between the Actual Storm Direction of Motion(degrees) and -20°C isothermal wind (degrees) for cells tracked in supercell cases. The solid line is a trendline of equality.....	67

Figure 5.9 A comparison between the Actual Storm Direction of Motion (degrees) and -10°C isothermal wind (degrees) for cells tracked in supercell cases. The solid line is a trendline of equality.....	68
Figure 5.10 A comparison between the Actual Storm Direction of Motion (degrees) and 0°C isothermal wind (degrees) for cells tracked in supercell cases. The solid line is a trendline of equality.....	69
Figure 5.11 A comparison between the Actual Storm Direction of Motion (degrees) and -20°C isothermal wind (degrees) for cells tracked in linear cases. The solid line is a trendline of equality. Values over 360 degrees are cell motions near the 0/360 degree direction discriminator, with 360 degrees added for continuity.....	71
Figure 5.12 A comparison between the Actual Storm Direction of Motion (degrees) and -10°C isothermal wind (degrees) for cells tracked in linear cases. The solid line is a trendline of equality. Values over 360 degrees are cell motions near the 0/360 degree direction discriminator, with 360 degrees added for continuity.....	72
Figure 5.13 A comparison between the Actual Storm Direction of Motion (degrees) and 0°C isothermal wind (degrees) for cells tracked in linear cases. The solid line is a trendline of equality. Values over 360 degrees are cell motions near the 0/360 degree direction discriminator, with 360 degrees added for continuity.....	73
Figure 5.14 A comparison between the Actual Storm Direction of Motion (degrees) and -20°C isothermal wind (degrees) for cells tracked in multicell cases. The solid line is a trendline of equality. Values over 360 degrees are cell motions near the 0/360 degree direction discriminator, with 360 degrees added for continuity.....	74
Figure 5.15 A comparison between the Actual Storm Direction of Motion (degrees) and -10°C isothermal wind (degrees) for cells tracked in multicell cases. The solid line is a trendline of equality. Values over 360 degrees are cell motions near the 0/360 degree direction discriminator, with 360 degrees added for continuity.....	75
Figure 5.16 A comparison between the Actual Storm Direction of Motion (degrees) and 0°C isothermal wind (degrees) for cells tracked in multicell cases. The solid line is a trendline of equality.....	76
Figure 5.17 A comparison between the Actual Storm Direction of Motion (degrees) and -20°C isothermal wind (degrees) for cells tracked in supercell cases. The red line is the $y=x$ trendline, while the blue/black line is the line of best fit.....	79

Figure 5.18 A comparison between the Actual Storm Direction of Motion (degrees) and -10°C isothermal wind (degrees) for cells tracked in linear cases. The red line is the $y=x$ trendline, while the blue line is the line of best fit. Values over 360 degrees are cell motions near the 0/360 degree direction discriminator, with 360 degrees added for continuity.....80

Figure 5.19: A comparison between the Actual Storm Direction of Motion (degrees) and 0°C isothermal wind (degrees) for cells tracked in multicell cases. 360 degrees is added in some cases for continuity. The red line is the Y=X trendline, while the blue line is the line of best fit.....81

LIST OF TABLES

Table	Page
Table 4.1 Cases and their identified cells (n=53) used for classification in the study.....	49
Table 5.1 The three classification types used within the classification tree study.....	52
Table 5.2 Selected output fields for multicells used in the study. VGP is a dimensionless parameter.....	54
Table 5.3 Selected output fields for supercells used in the study. VGP is a dimensionless parameter.....	55
Table 5.4 Selected output fields for linear cells used in the study. VGP is a dimensionless parameter.....	56
Table 5.5 Indicates the statistical values of MLCAPE for the three types of convective systems. MLCAPE values have different levels of variability for each type.....	57
Table 5.6 Indicates the statistical values of VGP for the three types of convective systems. VGP values have different levels of variability for each type.....	59
Table 5.7 Indicates the statistical values of SRH for the three types of convective systems. Supercells tend to have the highest SRH values....	60
Table 5.8 Indicates the statistical values of wind shear for the three types of convective systems. Supercells tend to have the strongest wind shear.....	62
Table 5.9 Rankings of the three different types of storms for selected parameters in the study.....	63
Table 5.10 Comparison of the standard deviation (in degrees) and mean squared error (in degrees squared) for the Isothermal Wind Method as opposed to the LB04 0-6 kilometer mean-wind method. While the standard deviation is lower for LB04, MSE is lower for the Isothermal Wind Method.....	77

Table 5.11 Comparison of the standard deviation (in degrees) and mean squared error (in degrees squared) for the Isothermal Wind Method as opposed to the C96 mean 850-300 mb wind method. Standard deviation and mean square error are smaller for the Isothermal Wind Method.....	78
Table 5.12 Comparison of the standard deviation (in degrees) and mean squared error (in degrees squared) for the Isothermal Wind Method as opposed to the M72 0-10 km mean wind method. The correlation coefficient is more predictive with less error using the Isothermal Wind Method.....	79
Table 5.13 Storm direction algorithms for the three types of storms.....	80
Table 5.14 Range of isothermal levels (hPa) for selected isotherms in the study.....	83
Table 6.1 Cases used in the study.....	90

ABSTRACT

In order to predict the location of heavy storm-generated rainfall that could produce flash flooding, forecasters want to know with what velocity a storm will move. However, few systems exist in meteorology where a storm is classified by type, and subsequently, forecast for motion. This publication focuses on identifying the ambient environmental characteristics typical of several types of severe convective storms.

Three types of severe convective storms are examined: supercell, linear, and multicell. Severe storm parameters for each type of system are collected, and ambient winds at critical levels are compiled to obtain a wind profile for eighteen total cases throughout the eastern United States. Previous studies have shown that supercell thunderstorms move with the anvil-level winds; linear storms with the 500-hPa wind; and multi-cellular storms with the lowest level winds. However, the findings of this study show that there is more complexity to predicting storm motion and, in many instances, careful selection of the level(s) of the wind to use is critical. By comparing actual storm motion in the 18 cases to isothermal wind motion at -20, -10, and 0°C, a more definitive correlation of storm type versus storm motion is obtained with less error than previous methods in the field of atmospheric science.

Chapter 1

Introduction

In the field of atmospheric science, storm motion has been a topic defined by a vast amount of research from numerous agencies. However, associating conclusively storm motion with storm type has shown to be one of the least researched topics in the field. Two of the most widely used nowcasting programs used in atmospheric science (the Spectral Prognosis scheme, or S-PROG, and Warning Decision and Support System-Integrated Information, or WDSS-II) intuitively use storm motion to make nowcasts of precipitation and storm intensity. These programs could be further enhanced by classifying severe convective storms by type and subsequently forecasting the motion of the storms from this information---along with existing environmental conditions.

Being able to determine whether storm type is a determining factor in storm motion has several practical results. Forecasters can warn the public in specific areas about certain severe weather threats, giving those warned more time to prepare for potential hazards. Second, applications to industry/business are also affected by storm motion, as the livelihood of many occupations are determined by the amount, intensity, and location of rain, hail, tornadoes, and other

weather phenomena. Third, storm type forecasts of storm motion can be used to provide another critical measure of uncertainty, as existing environmental conditions can be documented and “databased” to give forecasters a better idea of the growth, decay, merging, or splitting of storms in certain environmental conditions.

1.1 Statement of Thesis

The purpose of this study is to determine if storm motion is an advantageous method of classifying storm type. This will help forecasters make specialized nowcasts of convective weather conditions in a given area. By looking at three different types of cases with a statistical classifier, we can determine if the classifier can delineate types of storms based on their conditions which will be explored in the study.

Forecasters presently notify the public of severe weather conditions by noting current surface observations and using extrapolations of cell motion through various modes of radar imagery. Programs that forecasters currently use to track severe storms have no regard for storm type or environmental situations. These programs generally also use “standard” levels (850 mb, 700 mb, etc.) which may not be representative of the actual cloud-layer or vertical structure of every storm, yet are convenient for access. By knowing which

conditions are conducive to certain types of storms using information related to isothermal-level winds, forecasters will be aided in determining the future motion of those storms, and thus, give a better forecast of severe weather conditions for a given area. The objectives of this study are to:

- Determine the pre-existing meteorological conditions associated with three different types of severe convective storm systems (supercell, linear, multi-cell).
- Determine if the statistical classifier can delineate these types based on said meteorological conditions, and finally;
- Determine if storm motion can be more accurately predicted by the success of the statistical classifier in correctly indicating the convective mode of storms at storm genesis.

The main hypothesis to be tested in the study is that pre-existing dynamic and thermodynamic conditions (convective available potential energy, shear, etc.) will be different for each convective mode, and will therefore affect the motion of the storms in those modes. A secondary hypothesis is since the convective modes will have different environmental conditions, the statistical classifier will be able to note these differences and successfully

identify supercell, linear, and multi-cell convective systems. The success of the hypotheses will generate more accurate storm motion forecasts by the classification of storm type.

Chapter 2

Literature Review

Determining whether storm type is an important criterion for storm motion has far-reaching effects. Not only is it difficult operationally to delineate between and correctly predict storm type and motion, it is also difficult from an artificial intelligence standpoint. The implications of an erroneous nowcast of storm motion on the time scale of 0-60 minutes can be the difference between a forecast of tranquil weather or potentially severe/damaging weather conditions, with arising complications for emergency management personnel, government officials, and the public alike. For a comprehensive examination of relevant literature of the topic, this chapter will examine the research conducted thus far concerning the general motion characteristics of storms. Next, the specific motion characteristics of three types of storms; supercell, squall-line, and discrete multicell will be explored.

2.1 Forecasting Storm Motion

A great amount of time and effort has been invested to predict storm motion. In order for forecasters to predict storm motion, one must identify the location of the storm cells at initiation. The

Thunderstorm Identification, Tracking, Analysis, and Nowcasting system, or TITAN as explained in Dixon and Weiner (1993) gives a storm definition as a contiguous region that exhibits reflectivities above a given threshold (T_z), and the volume which exceeds a threshold (T_v). For individual convective cells, T_z equals 40-50 dBZ, while T_z for convective storms equals 30-40 dBZ (these thresholds can be adjusted by the user/forecaster). To identify storms, contiguous regions above T_z were needed. This was done by 1) identifying contiguous sequences of points (referred to in Dixon and Weiner (1993) as runs) in one of the two-dimensional principal directions (x or y direction) for which the reflectivity exceeds T_z and 2) group runs that are adjacent. This process is summarized in Figure 2.1:

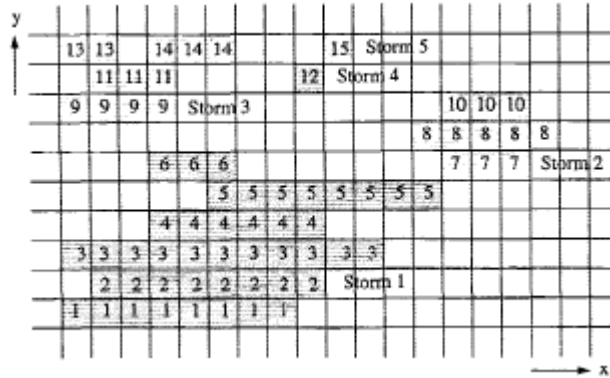


Figure 2.1: Example of storm data runs-2D case. Shading indicates grid points where the reflectivity exceeds T_z (from Dixon and Weiner, 1993).

The question then turns from storm identification to storm tracking. TITAN searches for the optimum set of storm paths by the following method, which will hereafter be referred to as the “optimal

set" method: a storm i at t_1 has state $\mathbf{S}_{1i} = \bar{X}_{z1i}, \bar{Y}_{z1i}, \mathbf{V}_{1i}$ and storm j at t_2 has state $\mathbf{S}_{2j} = \bar{X}_{z2j}, \bar{Y}_{z2j}, \mathbf{V}_{2j}$. Suppose too that there are n_1 storms at t_1 and n_2 storms at t_2 . The cost C_{ij} (in units of distance) of changing state \mathbf{S}_{1i} to state \mathbf{S}_{2j} is defined as:

$$C_{ij} = w_1 d_p + w_2 d_v, \text{ where} \quad (2.3)$$

$$d_p = [(x_{z1i} - x_{z2j})^2 + (y_{z1i} - y_{z2j})^2]^{\frac{1}{2}} \text{ (assumption 1),} \quad (2.4)$$

$$\text{and } d_v = \left| (V_{1i})^{\frac{1}{3}} - (V_{2j})^{\frac{1}{3}} \right| \text{ (assumption 2).} \quad (2.5)$$

(Dixon and Weiner 1993).

d_p is a measure of the difference of position (i.e., the distance moved), d_v is a measure of the difference in volume (also in units of distance, because of the cube root), and w_1 and w_2 are weights (Dixon and Weiner 1993). Assumption 1 implies that the correct set will include paths that are shorter than longer. Assumption 2 implies that the correct set will join storms of similar characteristics (size, shape, etc.). Mergers and splits are handled by TITAN with the matching algorithm by matching zero elements in the rows and columns of the domain. Forecast track vectors are then drawn for the two storms, as shown in Figure 2.2:

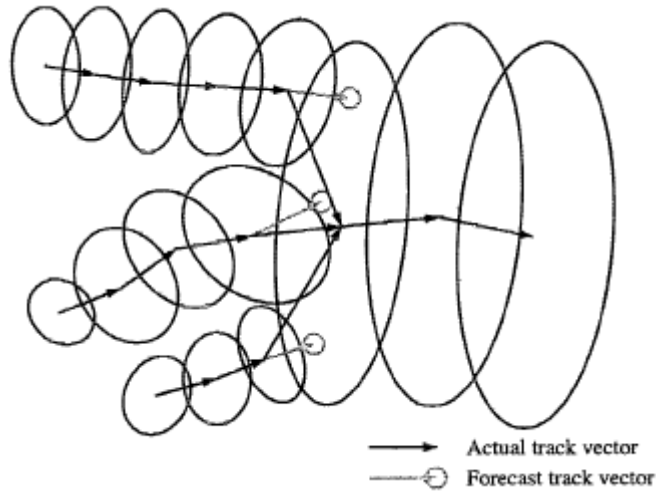


Figure 2.2: Storm merger (from Dixon and Weiner, 1993).

The following assumptions were made by Dixon and Weiner (1993) to formulate the storm forecast algorithm:

- A storm tends to move along a straight line.
- Storm growth or decay follows a linear trend.
- Random departures from the above behavior occur.

The forecast ellipse assumes that the orientation of the storm remains constant---an assumption later refined in future nowcasting systems.

The WSR-88D SCIT (Storm Cell Identification and Tracking) algorithm as described in Johnson *et al.* (1998) was developed to identify, characterize, track, and forecast the short-term movement of storm cells identified in three dimensions. MR-SCIT, a centroid-based cell identification and diagnosis algorithm described by Lakshmanan *et al.* (2002), worked by overlapping the 2D features of the WSR-88D SCIT system and running them on multiple sites to create a 3D system

of overlapped data sets from these radars. This allowed a more complete vertical analysis of storms where data was poor. The information from multiple radars was used to identify and track individual storm cells. Multiple radar data was detailed by Lynn and Lakshmanan (2002), in terms of “virtual volume” scans, with the latest elevation scan of data replacing the one from a previous volume scan (Lakshmanan *et al.* 2002).

Vertical and time association was performed at five-minute intervals which enables updating of the multiple-radar data. The virtual volumes containing data from the latest radar scan were combined to produce a vertical cross-section representing storm cells. Cell-based information such as POSH (Probability of Significant Hail) and hail size were also diagnosed by Lakshmanan *et al.* (2002) using the 2D to 3D combined multiple radar data system, as well as storm environment data from mesoscale models. Storm cells were tracked in time, and 30-minute nowcasts were made.

Three-dimensional storm identification begins with one-dimensional data processing to identify storm segments in the radial reflectivity data. A storm segment was saved in the Johnson *et al.* (1998) study if its radial length was greater than a preset threshold, usually around 1.9 km. WDSS then repeated the process using seven different reflectivity thresholds (60, 55, 50, 45, 40, 35, and 30 dBZ).

After the last radial of the elevation scan was analyzed, individual storm segments were combined into 2D storm components based on their proximity to one another (Johnson *et al.* 1998). This proximity is based on a 1.5 degree or closer azimuthal location and overlap in range of usually 2 kilometers. It was defined in the Johnson *et al.* (1998) study that storms must have two components and an area larger than 10 square kilometers. After 2D scans are made, 3D storm cells were made by merging two or more 2D storm components at different elevation angles. Scans were then made in an eliminatory process at 5, 7.5 and 10 km to see if two storm centroids were within these distances. The result is a 2D and 3D “snapshot” of a storm cell centroid; the storm cells are then ranked by their vertically integrated liquid water value (VIL) (Johnson *et al.* 1998). This method, however, has some drawbacks including poor temporal resolution (5-minute updates), and the fact that the algorithm uses data based from individual radars. Some attempts are being made to resolve these issues, including creating polar grids using a virtual volume value each time the radar scans, and a second method, computing VIL on multi-radar grids using 1 km grid spacing (Lakshmanan *et al.* 2002).

Storm cells identified in two consecutive volume scans are associated temporally to determine the cell track (Johnson *et al.* 1998). If the time difference is greater than 20 minutes, the second

scan is not attempted. This can happen due to malfunctions in the radar or interrupted communications. Using the centroid locations from the previous volume scan, a “guess” at the next location is created with the next volume scan (Johnson *et al.* 1998). To “guess”, WDSS uses the storm motion vector of the previous volume scan or a default motion vector if no previous one is detected. The motion vector of the storm is determined by using an average of all the storm cells’ motion vectors in the interface, or user input of the average 0-6-km wind speed and direction vectors of the cell. Next, the distance between the centroid of each cell and the “guess” of the next successive volume scan is calculated; if the distance is less than the threshold value, the distance between the new cell and all possible matches are determined (Johnson *et al.* 1998). The match with the smallest distance is considered the time-association of the detected cell. The motion vector is then calculated for the new cell by using a linear least squares fit of the storms’ current and up to 10 previous locations (see Figure 2). Each of the locations is given equal weight (Johnson *et al.* 1998). Once the tracking process is completed, data is tabulated for up to 10 previous volume scans.

Fox and Wilson (2005) and Jankowski (2006) found that the WSR-88D SCIT system works well with storms moving along linear paths. However, precipitation systems more often than not move in a

non-linear fashion, and the SCIT system provides no measurement of uncertainty within the forecast. Fox *et al.* (2007) concluded that the forecast motion is dependent upon the choice of precipitation area that is delineated. Micheas *et al.* (2007) used idealized elliptical cells to decompose the error contributions of various attributes such as orientation, size, and translation in a Procrustes verification scheme useful for a more robust verification solution.

By implementing a user-defined threshold of size and intensity for the object, the scheme identifies forecast objects (i.e. storm cells) of reflectivity. The cells in the forecast field are then matched to the cells in the observed field. The information on the error based on size, translation, and rotation are combined with error based on intensity values via a penalty function. The Micheas *et al.* (2007) forecast scheme begins shape analysis once matching is accomplished. The forecast object is overlaid onto its corresponding observed field and a fit is performed using the equation:

$$\hat{z}^j = \hat{c}_{jk} + \hat{r}_{jk} e^{i\hat{\phi}_{jk}} z^{kj}. \quad (2.1)$$

Equation 2.1 is known as the full Procrustes fit, the superposition of z^{kj} onto z^j where the first component c is the translation term, r is the dilation term and ϕ is the rotational component. Micheas *et al.* (2007) used these terms to incorporate the residual sum of squares (RSS) term in the penalty function:

$$D = RSS_k + SS_{avg}^k + SS_{min}^k + SS_{max}^k \quad (2.2)$$

The other components in the penalty function are the errors based on intensity differences between the forecast and observed object summed for the entire domain, thus, the lower the penalty, the better the forecast solution. It is interesting to note that case 14 in the Lack *et al.* (2007) study, a likely linear case, performed the best with the lowest penalty function.

2.2 Storm Type Classification

As the Micheas *et al.* (2007) verification scheme assesses the shape of the storm cell Lack *et al.* (2007) developed this in combination with near-storm environment parameters to objectively identify storm type using a decision tree. An automated rainfall system classification procedure with attributes that explore the characterization of the changing aspects of rainfall patterns can be an important technique to minimize the error of determining storm type (Baldwin *et al.* 2005). This was tested in recent work by comparing the results of automated various cluster analysis with a human expert classification of three storm types: linear, cellular, and stratiform, as well as two classes: convective and non-convective (Baldwin *et al.* 2005). Rainfall systems were defined as contiguous areas of precipitation, and the distribution of the random sample of objects was

scrutinized with respect to summary statistics to ensure a sample representative of the population.

2.3 Forecasting Supercell Motion

Supercells are defined similar to Moller *et al.* (1994): convective storms with mesocyclones or mesoanticyclones. Pinto *et al.* (2007) defined supercells as storms with areal coverage greater than 50 square kilometers and a peak reflectivity greater than 50 dBZ. Forecasters have spent the latter half of the twentieth century trying to obtain a better understanding of supercell propagation in relation to winds at multiple levels.

Two components are largely responsible for supercell motion as defined by Bunkers *et al.* (2000) --- (i) advection of the storm by a representative mean wind, and (ii) propagation away from the mean wind either toward the right or to the left of the vertical wind shear--- due to internal supercell dynamics. Knowledge of supercell motion has become widely known recently as anvil-level storm-relative flow has been used to discriminate among types of supercells (Rasmussen and Straka 1998). Thus, reliable prediction of supercell motion prior to supercell development is one key to improving severe weather forecasts. Extensive research was conducted in the mid-20th century pertaining to thunderstorm motion. It was generally observed that

non-severe thunderstorms moved with a representative mean wind, while stronger, larger, and long-lived thunderstorms moved slower and to the right of the mean wind (Bunkers *et al.* 2000). Under the assumption that supercell motion can be described by the sum of both an advective component and a propagation component---the equation for the motion of a right-moving supercell (V_{RM}) according to Bunkers *et al.* (2000) can be defined as

$$V_{RM} = V_{mean} + D \left[\frac{\hat{V}_{shear} \times \hat{k}}{\hat{V}_{shear}} \right] \quad (2.4)$$

The mean wind vector (or advective component) is given by V_{mean} , the vertical wind shear vector is given by V_{shear} , and D represents the magnitude of the deviation of the supercell motion from the mean wind. By reversing the cross product in Eq. (2.4), the equation for the motion of a left moving supercell (V_{LM}) can be similarly expressed in vector form as

$$V_{LM} = V_{mean} - \left[\frac{\hat{k} \times \hat{V}_{shear}}{\hat{V}_{shear}} \right]. \quad (2.5)$$

Bunkers *et al.* (2000) proposed an “internal dynamics” method for predicting both right and left-moving supercell motion. This is done by using the following procedure (for the northern hemisphere):

- The 0-6 km non-pressure-weighted mean wind is plotted;
- The 0-0.5 to 5.5-6km vertical wind-shear vector is drawn;

- cA line that both is orthogonal to the shear and passes through the mean wind is drawn;
- The right-moving supercell 7.5 m s^{-1} from the mean wind along the orthogonal line to the right of the vertical wind shear is located, and
- The left-moving supercell 7.5 m s^{-1} from the mean wind along the orthogonal line to the left of the vertical wind shear is located.

From Bunkers *et al.* (2000)

Left moving supercells have been observed, most notably by Lindsey and Bunkers (2004), contrary to most observed convective systems. Lindsey and Bunkers examined the differences between left-movers and their counterparts with respect to evolution, anvil orientation, and interaction with right-moving supercells, inferring that "...the left-moving supercell of velocity 13 m/s faster than the right-moving supercell in the case, when it interacted with it, disrupted its rotation." Thus, left-moving supercells involved in merger scenarios may have a disorganizing effect on their right-moving counterparts. This is consistent with earlier research on the effects of storm mergers on tornadogenesis (Finley *et al.* 2001).

The left mover in the Lindsey and Bunkers (2004) case affected its right counterpart thermodynamically and dynamically in numerous ways:

"...since the left mover progressed through the inflow of the right mover, it likely altered both the thermodynamics of the inflow and the ambient wind field into which the right mover progressed. The left mover intersected the forward flank of the right mover, so the anticyclonic rotating updraft of the left mover may have destructively interfered with the cyclonic rotating updraft of the right mover, resulting in less net rotation and therefore storm disorganization."

Anvil orientations were calculated for 479 right-moving supercells and compared to a theoretical left-moving supercell similar to the one looked at in the specific case study by Lindsey and Bunkers (2004). The median difference of anvil orientation for left and right-moving supercells was 54° (Lindsey and Bunkers 2004).

2.4 Forecasting Squall-line Motion

The squall line has been defined loosely as a linearly oriented mesoscale convective system (Maddox, 1980; Bluestein and Jain 1985), hereafter known as MCS. Corfidi *et al.* (1996) defined MCS motion as a vector sum of an advective component, and a propagation component, stated as the *Corfidi vector*. Thus, Corfidi *et al.* (1996) modeled MCS core motion as the vector sum of a vector representing cell advection by the mean-cloud-layer wind and a vector representing

new cell development directed anti-parallel to the low-level jet (Fig. 2.3).

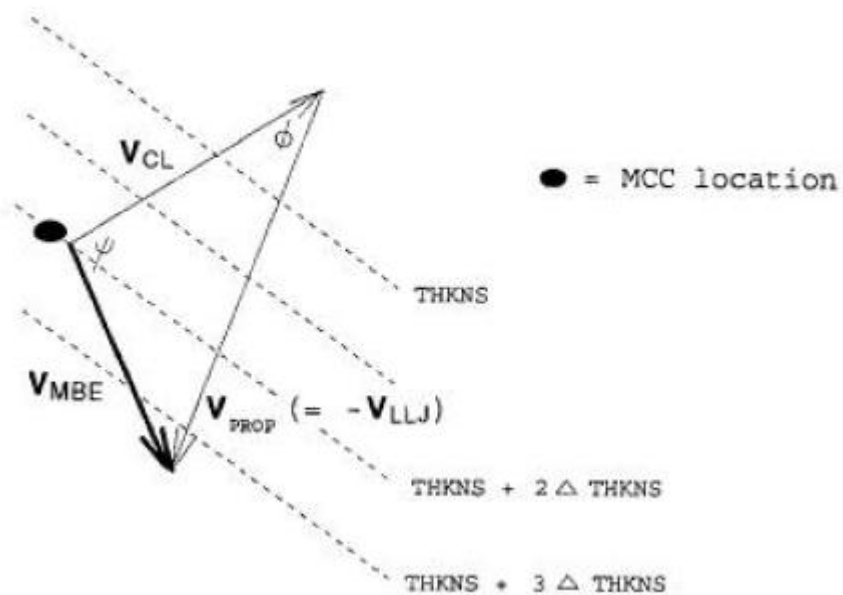


Figure 2.3: Illustration of the advective component (\mathbf{V}_{CL}) and the propagation component ($\mathbf{V}_{\text{PROP}} = -\mathbf{V}_{\text{LLJ}}$) as the vector sum of MBE movement (\mathbf{V}_{MBE}). The angles ψ and ϕ are used in the calculation of \mathbf{V}_{MBE} and the dashed lines are the 850-300 mb thickness pattern to the environmental flow (from Corfidi et al. 1996).

Corfidi et al. (1996) also studied the movement of radar-observed Mesobeta-scale Convective Elements (MBEs). The centroid location of the MBE was plotted at each time step to observe movement. A straight best-fit line from storm initiation to storm decay was then found to find the mean speed and direction of the MBEs' movement. A second method of determining MBE movement is the vector difference of the mean flow in the cloud layer and the low level-jet being:

$$V_{MBE} = V_{CL} - V_{LL}. \quad (2.6)$$

The hypothesis in Corfidi *et al.* (1996) was correct; the advective component is dictated by the mean cloud layer and the propagation component has a tendency to propagate towards the low-level jet. This was suitable for operational use and provided insight in forecasting MCS motion (Jankowski, 2006). This study will look at the importance of motion vector differencing with storm type.

Squall lines can be broken down further into four distinct categories: broken line, back-building, broken areal, and embedded areal (Fig 2.4).

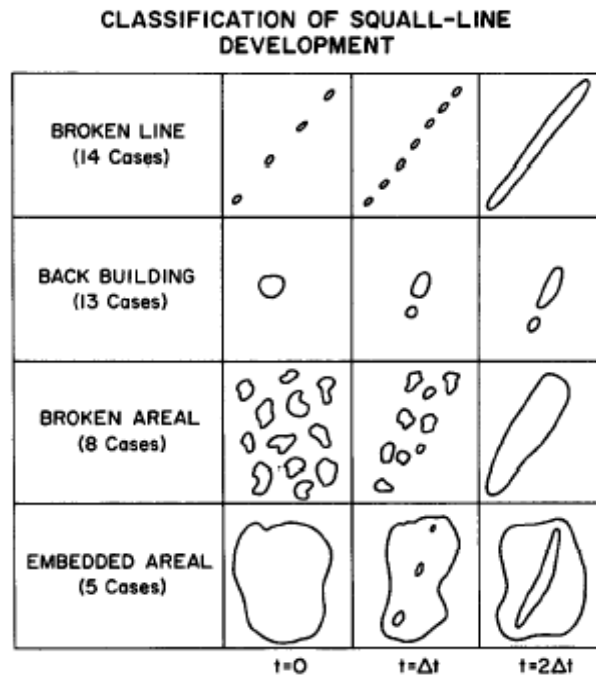


Figure 2.4: Idealized depiction of squall-line formation (from Bluestein and Jain, 1985).

Bluestein and Jain (1985) defined squall line motion as oriented along the mean wind in the lowest 1 km, at a large angle to the wind in the lowest part of the middle troposphere, and at an angle of 30-40° from the shear somewhere in the upper troposphere. Therefore, squall lines fall into the steering category proposed by Moncrieff (1978); each type has a mean steering level (MSL) with respect to line motion around 6 or 7 km above the surface. Cells tend to move along the line, with a little component against line motion (fig. 2.4): (Bluestein and Jain 1985). Charba and Sasaki (1971) found that linear storm systems displace towards the right of the mean wind even though individual cells may move in the direction of the ambient upper-level winds. This displacement occurs as new cells develop upstream from existing cells towards the right-flank, low-level inflowing current (Charba and Sasaki 1971), thus occurring when winds veer with height.

2.5 Forecasting Multi-Cell Motion

The National Weather Service (NWS) has defined multicell thunderstorms as clusters of at least 2-4 short-lived cells. Each cell generates a cold air outflow; these individual outflows combine to form a large gust front. Convergence along the gust front allows new storms to develop; the cells move roughly with the mean wind at first,

but then deviate significantly from the mean wind due to new cell development along the gust front. Fovell and Tan (1996) defined multicells as a family of cells within a cross section of the idealized squall-line, each representing a different stage in the life cycle.

Research pertaining to multi-cellular thunderstorms has been conducted for decades, with Browning and Ludham (1960) existing as the first significant study of storms of a multi-cellular nature. Browning and Ludham (1960) worked with a series of aligned cells near Wokingham, England in which new cells periodically developed on the right flank, moved with the storm complex, and dissipated on the left flank. This form of discrete propagation caused deviant motion towards the right flank. Chisholm (1966) analyzed two multi-cell storms in Alberta, which deviated towards the right flank by discrete propagation while individual cells within the storm complex moved in the direction of the environmental winds. The environmental conditions for the storms are noted here in figure 2.5:

Case study	ΔT_{s00} (°C)	Veering in sub- cloud (deg)	Mean wind in subcloud (deg/ m sec ⁻¹)	Mean wind from surface to 10 km (deg/ m sec ⁻¹)	Storm motion (deg/ m sec ⁻¹)	Shear in cloud layer (sec ⁻¹)	Propagation Individual cells	Propagation Discrete
Browning and Ludlam (1960)	+1	160	150/08	210/21	225/18	2.5×10^{-3}	No Propagation	Right
Chisholm (1966) 18 July 1964	+4	40	240/07	235/26	250/12	—	No Propagation	Right
Chisholm (1966) 21 July 1964	+4	-90	250/06	230/17	250/10	—	No Propagation	Right
Alhambra storm 12 July 1969	+2	30	020/30	245/11	300/09	2.0	Right	Right
Rimbey storm 16 July 1969	+4	30	150/04	240/11	240/11	2.0	Left	Right
Benalto storm 17 July 1968	+3	45	150/04	265/07	305/09	1.5	Right	Right
Sylvan lake storm* 25 July 1968	+6	80	010/04	275/13	315/16	2.0	Right	Right
Carstairs storm 17 July 1969	+4	120	250/03	265/15	295/12	4.0	Right	Right
Butte storm 11 July 1970	+7	10	140/06	235/16	310/07	4.5	Right	Right

* This storm has been synthesized in detail by Chisholm (1970).

Figure 2.5: Thermodynamic stability and wind shear parameters for storms documented in Marwitz (1972).

The mean wind speed in the sub-cloud layer noted by Browning and Ludham (1960) was less than or equal to 8 meters per second. By comparison, the mean wind speed in the sub-cloud layer for supercells was noted by Marwitz (1972) as 10-17 meters per second. The extreme instability values for the two types of storms were similar, but the minimum values were substantially smaller for multi-cellular storms. It was concluded in Marwitz (1972) that the distinguishing characteristic of the environment which produced multi-cell storms was light winds in the sub-cloud layer. Marwitz (1972) also included models of typical right, left, and no deviate motion from the environmental winds, seen in figures 2.6, 2.7, and 2.8:

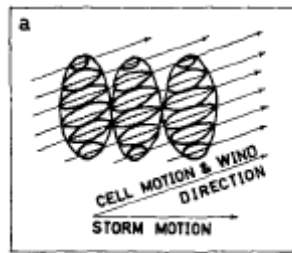


Figure 2.6: Multi-cell motion with the environmental winds (Marwitz 1972).

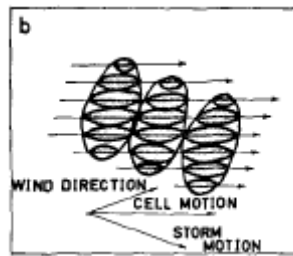


Figure 2.7: Multi-Cell motion to the right of the environmental winds (Marwitz 1972).

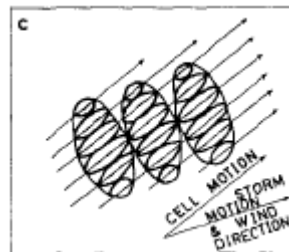


Figure 2.8: Multi-cell motion to the left of the environmental winds (Marwitz 1972).

By examining pertinent research, one can conclude that several factors will determine the ultimate motion of a severe convective storm. By documenting and classifying individual cells, one can infer the general track of the cells, as well as evaluate the overall effectiveness of nowcasting systems in forecasting those cells' motions. Thus, with a better classification and evaluation system for

storm type, one can better infer storm motion, improving forecasts and reducing error.

Chapter 3

Methodology

3.1 Study Focus

Storm motion can be affected by several factors such as the relative timeframe of the storm in its life cycle, splitting, merging, propagation into stable or unstable air masses, and the relative location of the cell in the parent storm system. For this study, storm motion will be measured in meteorological coordinates (0° indicates from the north, 90° indicates from the east, etc.) unless otherwise stated. This study will attempt to determine if storm motion can be more accurately predicted by classifying storm type at genesis and knowing the meteorological conditions associated with those types.

3.1.1 Area of Study

Three different geographical regions of the United States exist as the area of focus for this study. Eighteen (18) storm systems are contained in the three regions classified as eastern, Midwestern, and southern. The eastern region contains cases in the states of Pennsylvania (PA) and Virginia (VA). The Midwestern region contains cases from Missouri (MO), Kansas (KS) and Nebraska (NE), while the southern region contains cases from Tennessee (TN), Texas (TX),

Georgia (GA), Mississippi (MS), and Florida (FL). Three regions are used to apply information learned in the study to different sections of the country. The eighteen cases are broken down into three categories defined by the convective mode of storms in the cases: supercell, linear, and multi-cell. Within the events, ambient wind profiles/conditions are noted, and individual cells are identified and tracked for motion.

3.1.2 Selection of Storm Cells

The first category of case studies consisted of events with supercell characteristics, in which a selection procedure needed to be utilized. Storm cells in this category were picked based on their size. The statistical classifier used in the study allowed a user-defined threshold for the objects, in which supercells smaller than 500 km² (Lack 2007) in any case were discarded.

Storm cells within this category were selected also based on a user-defined threshold of reflectivity, similar to the Pinto *et al.* (2007) peak reflectivity threshold of 50 dBZ. If the cell on four consecutive scans (~20 min) maintained a peak reflectivity of higher than 50 dBZ, it was included in the study. The use of four scans was determined based on a modified Bunkers *et al.* (2000) definition for two reasons: first, most supercells last shorter than 2 hours; some supercells

(rarely) last less than 10 minutes, and, four scans also implies that storm tracking is possible, and above all else, reliable.

The second category of case studies consisted of events with squall-line characteristics, in which individual convective cells within the squall-line were tracked for motion as well as the squall-line itself. Squall-lines in the category were selected based on the Bluestein and Jain (1985) definition of related or similar echoes that form a pattern exhibiting a length-to-width ratio of at least 5:1, greater than or equal to 50 km long, and persisting for longer than 15 minutes (or 3 volume scans). These features were chosen because of their consideration to be mesoscale as well as their increased probability of containing cells with lifecycles relevant to the study as described above.

The third category of case studies consisted of events with multi-cell characteristics, in which cells at different points in their life-cycles are tracked for motion. Multi-cells in this category were selected based on their life cycle of less than 1 hour as described by Fovell and Tan (1996) and their user-defined size (roughly 50-100km²). Cells in this category were also selected based on a user-defined threshold of reflectivity greater than 30 dBZ as most thunderstorms with multi-cell characteristics rarely produce heavy rainfall (in excess of 50 dBZ) for more than 15 minutes. If the cell maintained a peak reflectivity

greater than 30 dBZ for more than 3 consecutive volume scans, it was included in the study.

3.2 Data

Radar data for each case were collected from the National Climate and Data Center (NCDC) in the form of level II NEXRAD data and processed through radar display software called the Warning Decision Support System-Integrated Information (WDSS-II). WDSS-II utilizes a National Severe Storms Laboratory (NSSL) algorithm similar to Johnson *et al.* (1998) which identifies an individual storm's location, movement, and other characteristics within a cell table.

Storm environment data were collected from the NCDC in the form of Rapid Update Cycle-252 (RUC-252) 20 km resolution data for all eighteen cases. The data were compiled in the "grib" file format, in which WDSS-II converts the grib files to text files using the "GribtoNetCDF" command. Boundaries were specified in the GribtoNetCDF command to match the radar Cartesian 256 X 256 km grid, allowing the model data for each case to be overlaid on grids of radar reflectivity.

3.3 Procedure

To track cells for motion and speed a number of steps had to be completed. Radar data were analyzed from the following National Weather Service (NWS) radar sites (Fig. 3.1): Kansas City, MO (EAX), Memphis, TN (NQA), Amarillo, TX (AMA), Saint Louis, MO (LSX), Hastings, NE (UEX), Atlanta, GA (FFC), Nashville, TN (OHX), Fort Worth, TX (FWS), Jackson, MS (JAN), Tampa Bay, FL (TBW), State College, PA (CCX), Sterling, VA (LWX), and Columbus Air Force Base, MS (GWX).



Figure 3.1: Radar site locations (thirteen sites) for the eighteen cases in the study. Locations are approximate.

Storm motion and velocity was tabulated for each cell in each case by averaging the 5-minute SCIT centroid motion values (in

WDSS-II) during the life of the cell. Near-storm environments are derived from model data ingested into WDSS-II. In the specific case of RUC-model isothermal winds, the values were taken from the specific 20 X 20 km “center” of the cell. From the model data several parameters were tabulated for each cell which included height of 0, -10, and -20°C isotherms; mean wind speed from surface to 6 kilometers (measured in knots); storm motion (direction measured in degrees, speed measured in knots); shear from 0-6 kilometers (measured in $\text{m s}^{-1} \text{ km}^{-1}$); propagation (left or right in the case of supercells and multicells, and direction in the linear cases); mean-layer convective available potential energy (MLCAPE; measured in J kg^{-1}), 0-3-km storm relative helicity (SRH; measured in $\text{m}^2 \text{ s}^2$), the u and v-wind components at the 0, -10, and -20°C isotherms (measured in knots), and the dimensionless Vorticity Generation Parameter (VGP), which is defined in Rasmussen and Blanchard (1998) as

$$\text{VGP} = [S(\text{CAPE})]^{\frac{1}{2}} \quad (3.1)$$

where (S) is the mean shear in the column. These parameters were chosen from the Marwitz (1972) multicell study and the Lack *et al.* (2007) cell classification study for their usefulness for all storm types. Comparisons of the parameters were then made between cases and similarities/differences were noted.

The cases were subsequently analyzed with a cell identification script in MATLAB with the previous parameter information included. The “numberID_simp.m” file identifies the individual cell to be analyzed, while the “identifycells.m” file lists cells that match the size criteria in a “finalarray” function. The script also produces images of each convective system for easy reference. Scripts for the files are included in the appendix. With these calculations, the success of the classifier in identifying convective systems of different types was analyzed.

The 0, -10, and -20°C isotherms, as well as their u and v-wind components, were chosen because of their proximity to the cloud layer steering winds (Marwitz 1972) as well as their variability in height in different cases, and subsequent, lack of upper and lower height boundaries. The mean wind speed from the surface to 6 kilometers was chosen as a parameter to compare with the speed of propagation of the individual convective system. The shear from 0-6 kilometers was chosen to note pre-existing environmental conditions prior to storm genesis and to note trends among storms of different types. Propagation, MLCAPE, 0-3 kilometer SRH, and VGP were noted for the same reason.

Chapter 4

Case Studies

Eighteen storm events were selected for this study from a range of geographical regions within the continental United States. Storm events were divided into three different categories: supercell, squall-line, and multi-cell with six events in each category. The basis for the categories was the appearance of the storms and the orientation of the storm systems (discrete, linear, or clustered). The following sections will describe these events in detail.

4.1 Supercell Events

4.1.1 12 March 2006: Pleasant Hill, MO region

The National Weather Service (NWS) WSR-88D radar located in Pleasant Hill, MO recorded a supercell event during the period 1900 UTC 12 March 2006 to 2230 UTC 12 March 2006. Two supercells are of note in this event: the first being the “five-state” supercell, which tracked across northeastern Oklahoma, Kansas, Missouri, Illinois, and northwestern Indiana before finally dissipating 17.5 hr after genesis. The second supercell formed just to the north of the five state supercell and eventually merged with it near the Missouri-Illinois

border. Figure 4.1 shows four distinct supercells moving northeast through Missouri on 12 March 2006 that produced several tornadoes.

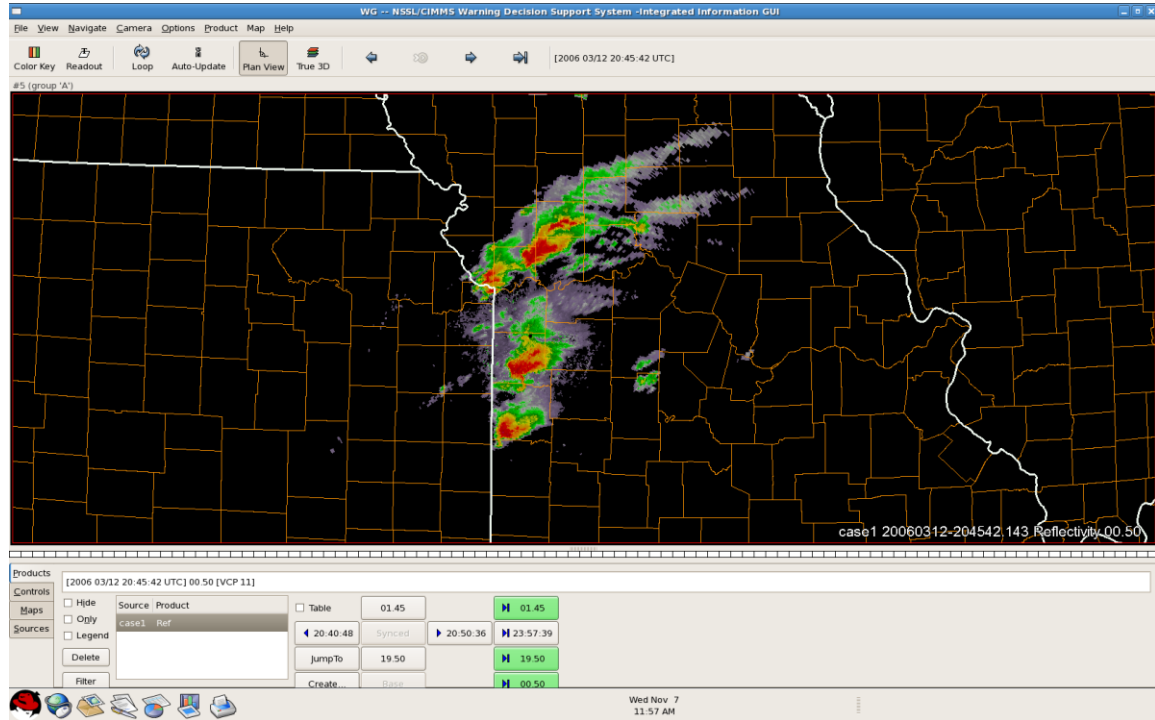


Figure 4.1: A radar composite reflectivity image from the National Weather Service EAX radar site at 2045 UTC on 12 March 2006. The radar site is located southeast of Kansas City near Jackson County, MO. The “five-state” supercell is the cell furthest to the south in the image, along the Kansas/Missouri border.

4.1.2 2-3 April 2006: Memphis, TN region

This event occurred over two separate regions on 2 April 2006 as discrete supercells merged and formed a squall line that stretched from western Illinois south through eastern and southeastern Missouri. In this case, a discrete supercell on the southwestern flank of the squall line was responsible for an F2 tornado that hit the town of Caruthersville, MO, just to the north of the NQA radar site (around

2350 UTC 2 April 2006). This study will focus on the period of 2130 UTC 2 April to 0200 UTC 3 April. Figure 4.2 shows four supercells moving east through sections of Missouri, Arkansas, and Tennessee.

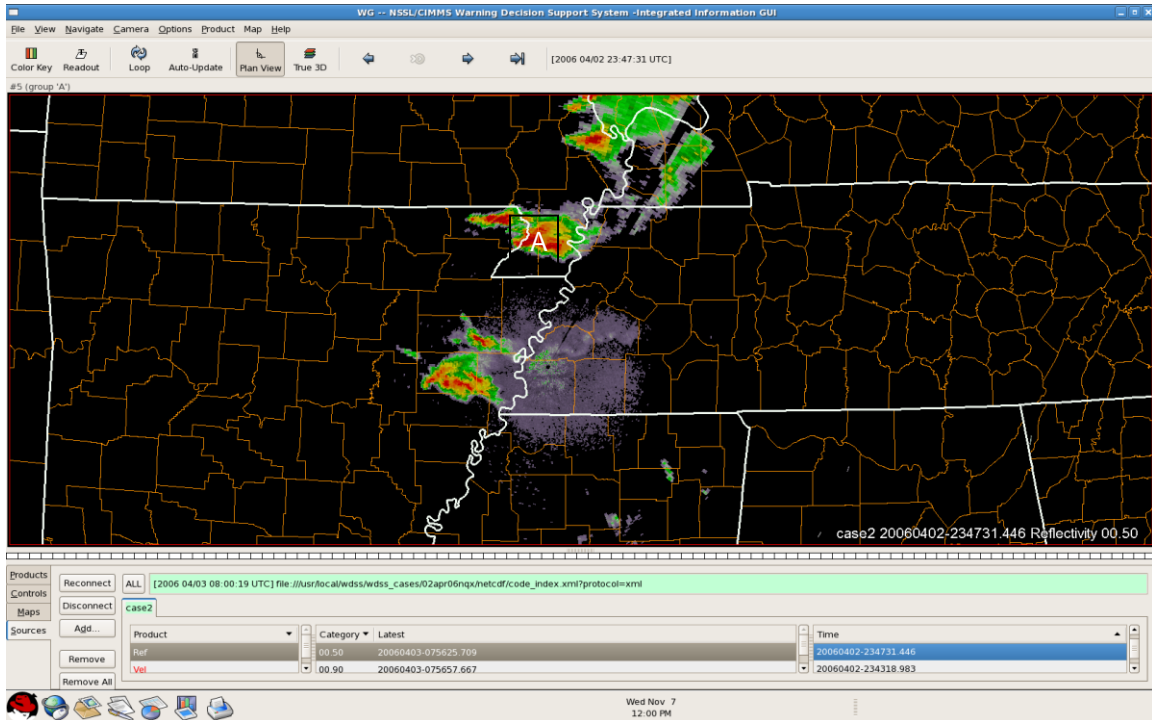


Figure 4.2: A radar volume scan from the National Weather Service NQA radar site at 2347 UTC on 2 April 2006. The supercell that hit the town of Caruthersville, MO is indicated with the letter "A". The radar site is located northeast of Memphis near Shelby County, TN.

4.1.3 21-22 April 2007: Amarillo, TX region

An upper-level low pressure system which moved out of the intermountain west into the Great Plains was responsible for this event which occurred near Amarillo, TX from 2200 UTC 21 April 2007 to 0300 UTC 22 April 2007. Numerous supercells on the southwestern flank of an east-moving squall-line are portrayed on the AMA radar image (see figure 4.3). Maturing over the city, the supercells

produced several reports of property damage. Figure 4.3 shows numerous supercells tracking to the north-northeast towards the city of Amarillo.

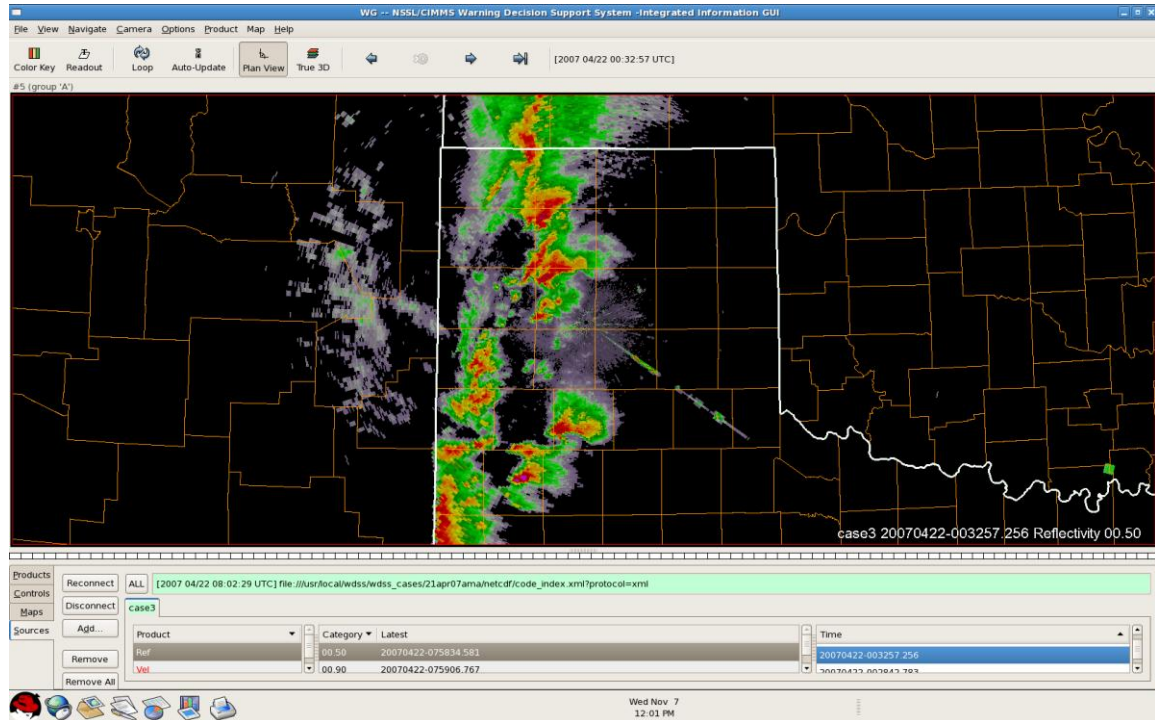


Figure 4.3: A radar composite reflectivity image from the National Weather Service AMA radar site at 0032 UTC on 22 April 2007. The radar site is located northwest of Amarillo near Potter County, TX.

4.1.4 28-29 March 2007: Amarillo, TX region

The AMA radar located in Amarillo, TX observed a left-moving supercell of note from 2100 UTC 28 March 2007 to 0330 UTC 29 March 2007. The storm-relative motion of the supercell was north-northwest; it generated from another supercell which was moving to the northeast. The left-moving supercell, however, proved to be much weaker than the parent supercell which produced numerous tornado reports in the panhandle of Texas. Figure 4.4 shows five supercells

moving through the panhandle of Texas that produced numerous confirmed tornadoes.

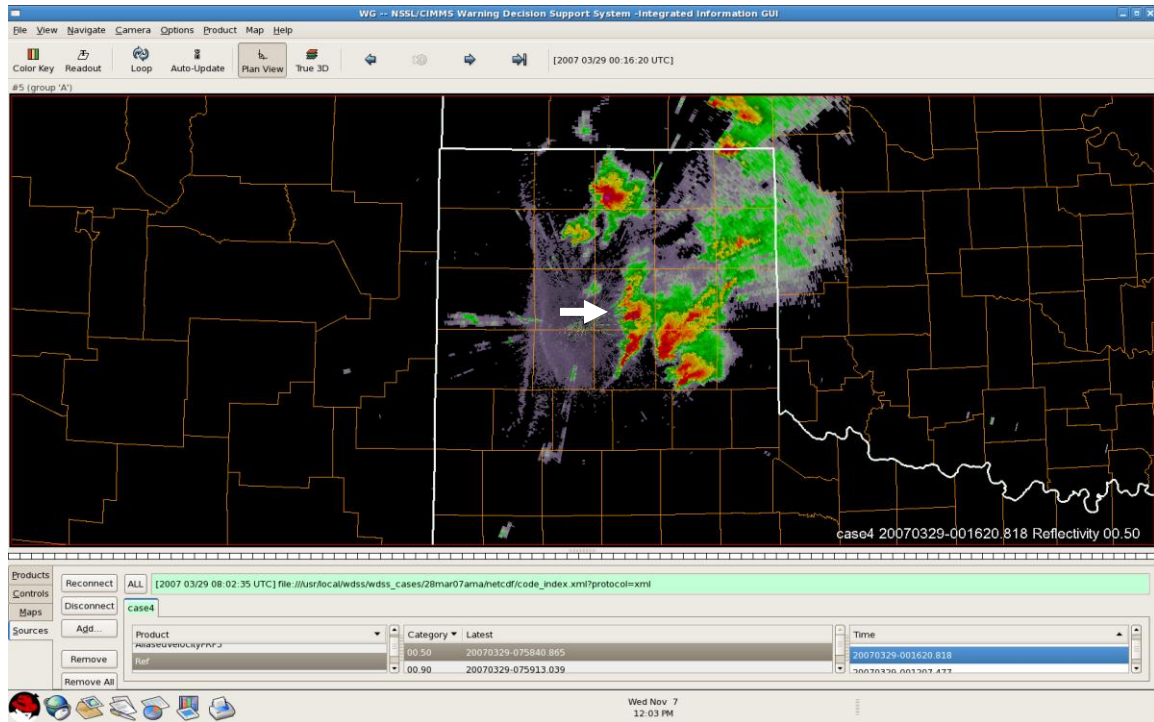


Figure 4.4: A radar composite reflectivity image from the National Weather Service AMA radar site at 0016 UTC on 29 March 2007. The arrow points to the left-moving supercell.

4.1.5 4 May 2003: Topeka, KS region

The TWX radar located in Topeka, KS recorded one of the most prolific severe weather outbreaks in history. The 4 May 2003 event was responsible for 86 confirmed tornadoes. A persistent 500-mb trough had entrenched itself over the western United States, while southeasterly to northerly flow at critical levels (1000mb; 850 mb respectively) enhanced wind shear. The supercell examined in this case from 2030 UTC 4 May to 2330 UTC 4 May produced numerous

tornadoes in and around the Kansas City, MO area as a left-moving supercell merged with another, right-moving supercell. Figure 4.5 shows five supercells moving into Missouri shortly after 2130 UTC 4 May 2003.

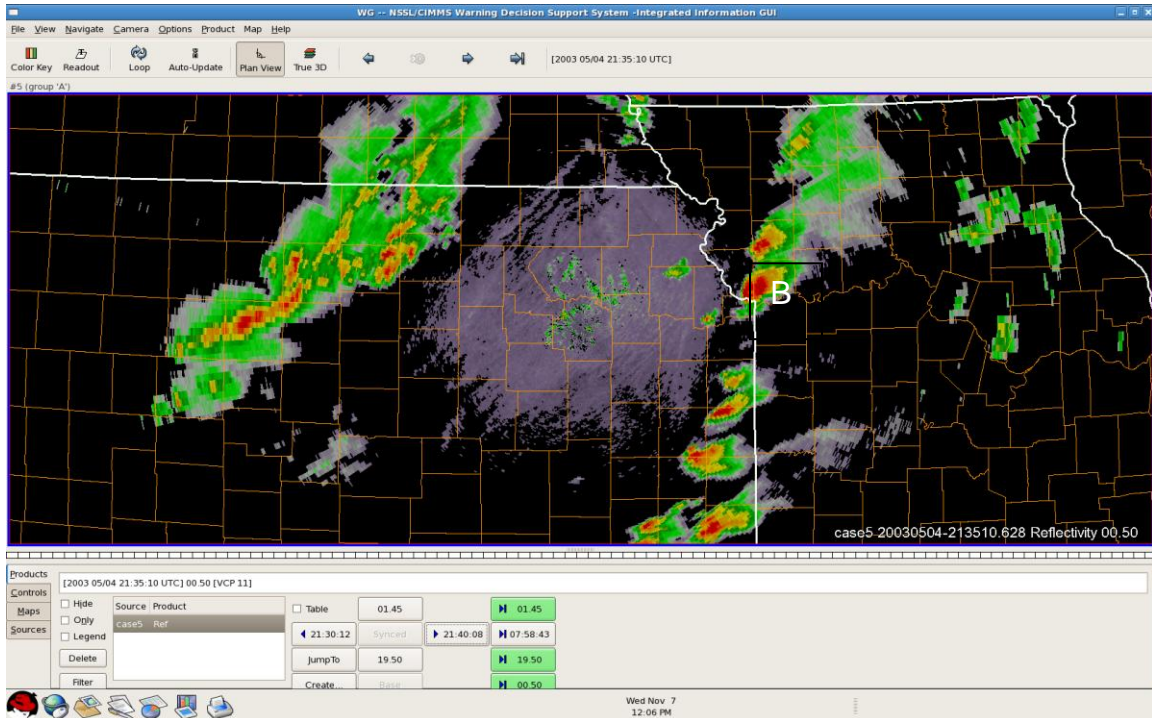


Figure 4.5: A radar composite reflectivity image from the National Weather Service TWX radar site at 2135 UTC on 4 May 2003. The left-moving supercell in this case is indicated with the letter "B". The radar site is located south of Topeka near Wabaunsee County, KS.

4.1.6 7 April 2006: Memphis, TN region

The NQA radar site (Memphis, TN) recorded several supercells which moved across the same area over a seven-hour period (1430 UTC to 2130 UTC) during the day of 7 April 2006. As a result, severe flooding affected areas in central Tennessee, with numerous reports of tornadoes as the storms tracked east-northeast. Figure 4.6 shows five

supercells east of Memphis on 7 April 2006. The existence of the cells over the same region for several hours served as a catalyst for flooding in the region.

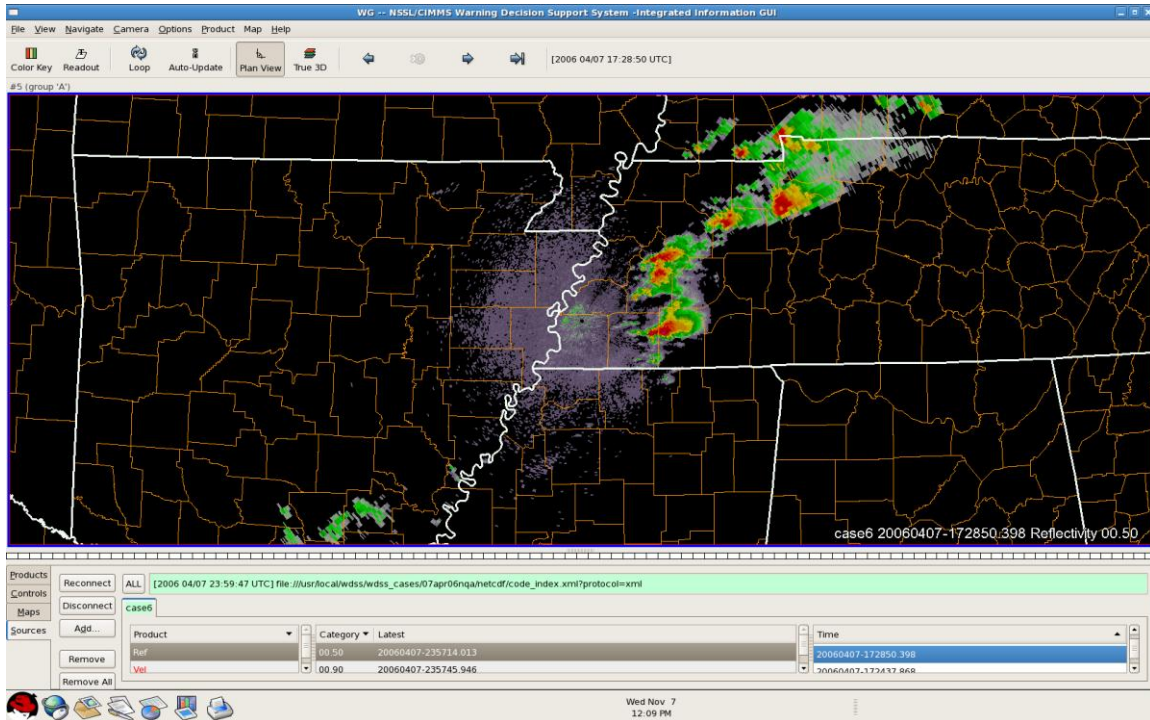


Figure 4.6: A radar composite reflectivity image from the National Weather Service NQA radar site at 1728 UTC on 7 April 2006.

4.2 Squall-line events

4.2.1 19-20 July 2006: Saint Louis, MO region

The NWS WSR-88D radar located in St. Louis, MO (LSX) recorded a southerly moving squall-line (or derecho) that tracked directly across the metropolitan St. Louis area from 2230 UTC on 19 July to 0230 UTC 20 July 2006. The region at the time experienced unseasonable warmth, with highs near 100°F with dewpoints at or above 70°F. The squall-line initiated well to the north as an MCS near

the Minnesota-Iowa border before traveling clockwise with the 500-mb flow into the St. Louis area at 0045 UTC 20 July 2006. Figure 4.7 shows the easily seen derecho moving through the Saint Louis metropolitan area.

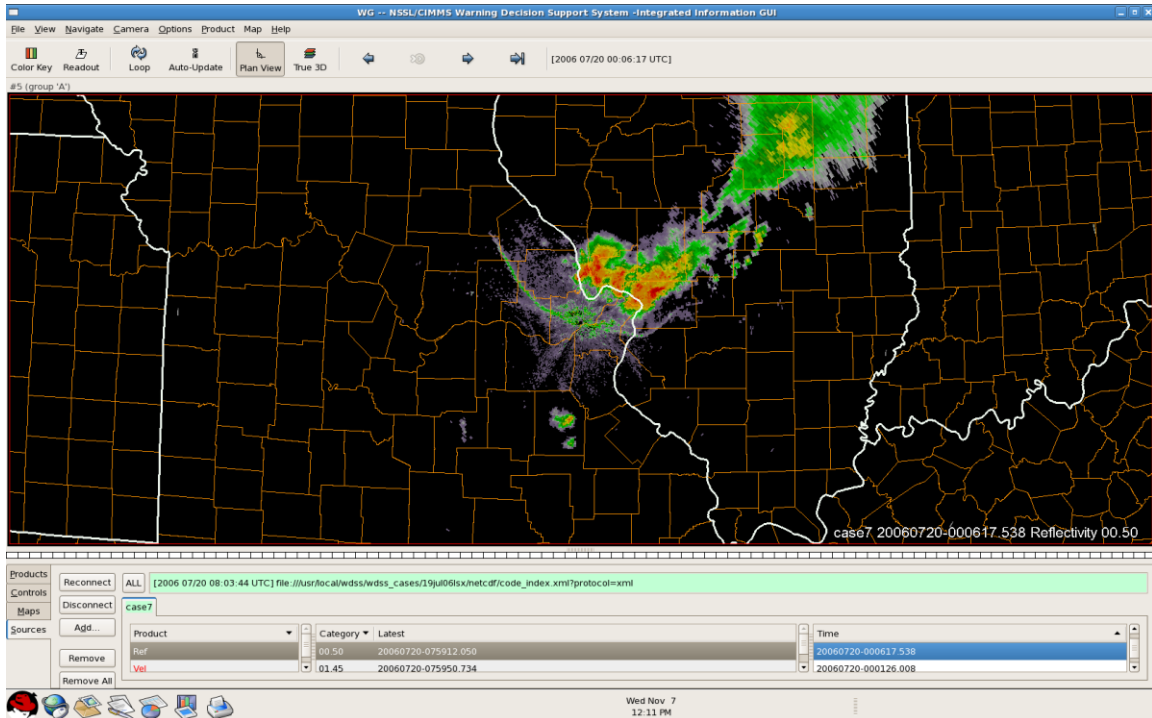


Figure 4.7: A radar composite reflectivity image from the National Weather Service LSX radar site at 0006 UTC on 20 July 2006. The radar site is located southwest of Saint Louis near Saint Charles County, MO.

4.2.2 21 July 2006: Saint Louis, MO region

The LSX radar site recorded another squall-line with many of the same characteristics as the case described in 4.2.1 roughly 48 hours later (1330 UTC 21 July 2006 to 1730 UTC 21 July 2006) in the St. Louis metropolitan area. The squall-line associated with this case moved from west to east across the area in accordance with the

orientation of a stationary front through the region. Figure 4.8 shows the bowing line segment moving towards the Saint Louis area late in the morning on 21 July 2006.

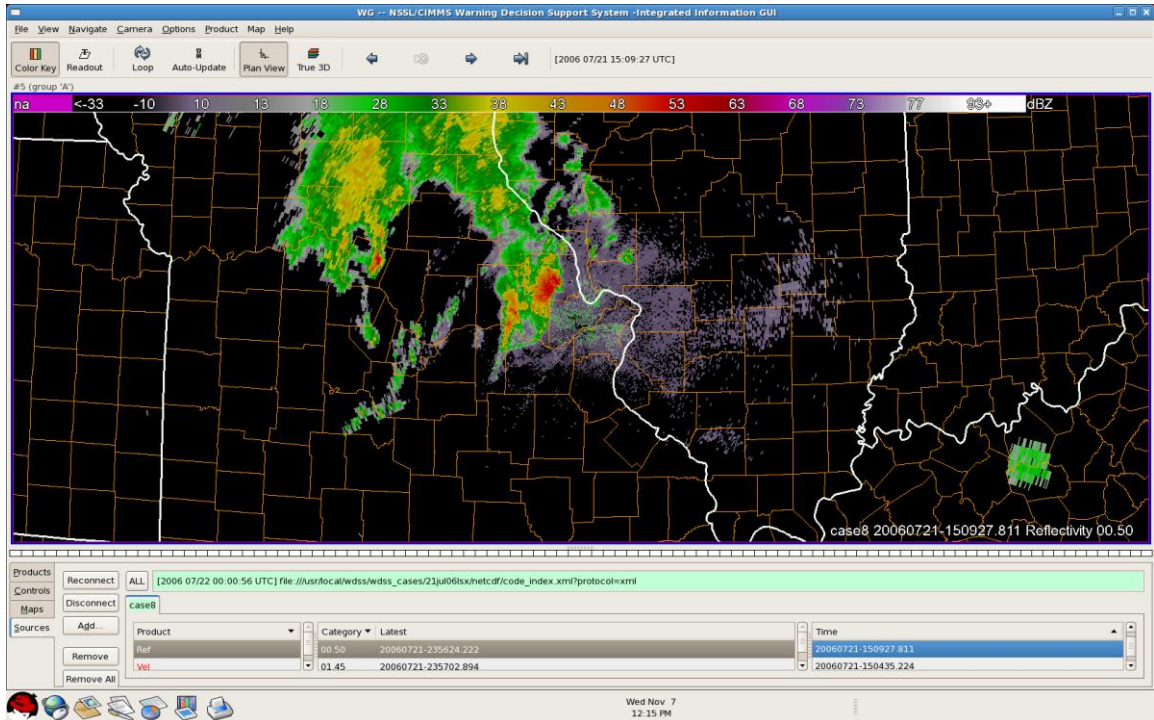


Figure 4.8: A radar composite reflectivity image from the National Weather Service LSX radar site at 1509 UTC on 21 July 2006.

4.2.3 9 July 2004: Hastings, NE region

The third case of this type was recorded at the Hastings, Nebraska radar site (UEX) from 0230 UTC to 0700 UTC on 9 July 2004. A squall-line associated with an outflow boundary from a disintegrating cold front moved southeast through the area, producing widespread damage to mostly rural areas. The Hastings case is of note because it is a classic case of broken areal squall-line development as outlined by

Bluestein and Jain (1985). Figure 4.9 shows the squall-line moving southeast towards the radar site.

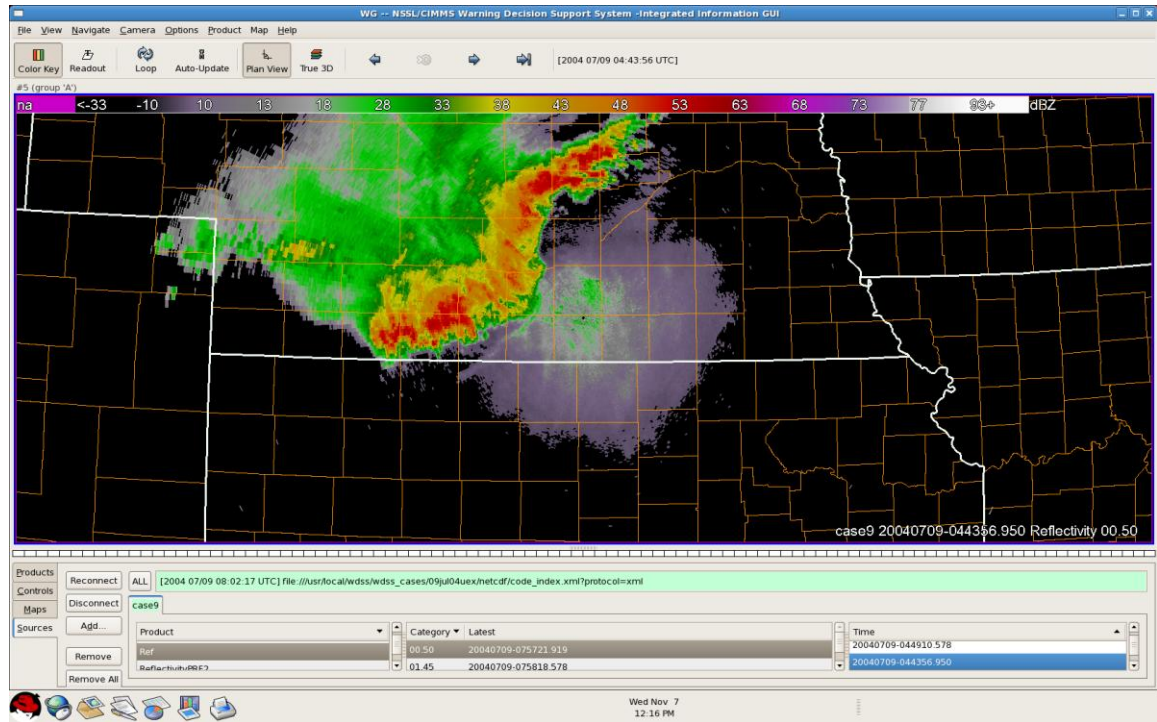


Figure 4.9: A radar composite reflectivity image from the National Weather Service UEX radar site at 0443 UTC on 9 July 2004. The radar site is located south of Hastings near Webster County, NE.

4.2.4 2-3 May 2003: Atlanta, GA region

The FFC radar observed two different squall-lines moving in different directions during the period 1830 UTC 2 May 2003 to 0130 UTC 3 May 2003 which originated from discrete supercell development to the west. Outflow boundaries played a key role in storm motion, as the first squall-line moved directly to the east (to the left of the 500-mb flow) while the second squall-line moved to the south-southeast (to the right of the 500mb flow) approximately 2-3 hours later. Figure

4.10 shows both squall-lines tracking through central Georgia on 2 May 2003.

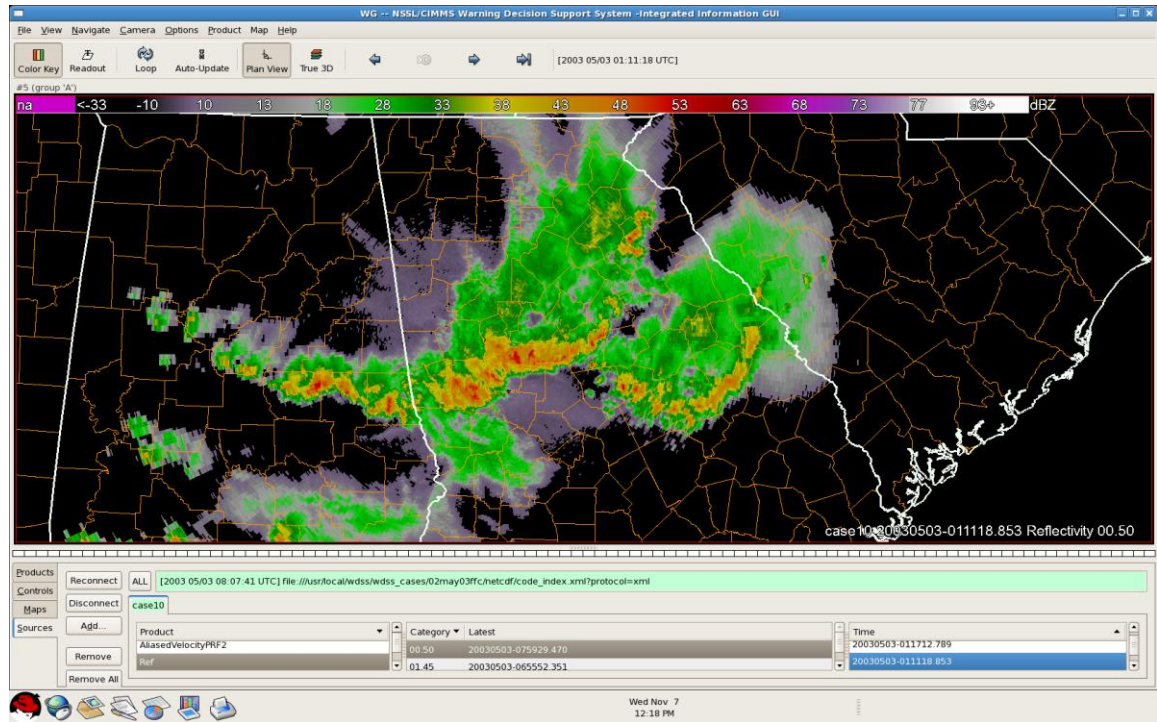


Figure 4.10: A radar composite reflectivity image from the National Weather Service FFC radar site at 0111 UTC on 3 May 2003. The radar site is located southeast of Atlanta near Henry County, GA.

4.2.5 19 October 2004: Nashville, TN region

The OHX radar located in Nashville, Tennessee recorded a fall-season squall-line event from 0130 UTC to 1100 UTC on 19 October 2004. The squall-line originated as discrete supercells moving east with the 500-mb mean wind over southeastern Missouri, merging to form a squall-line in the overnight hours of 19 October 2004 near Nashville, TN. Figure 4.11 shows the line with bow echoes moving southeast during the overnight hours on 19 October 2004.

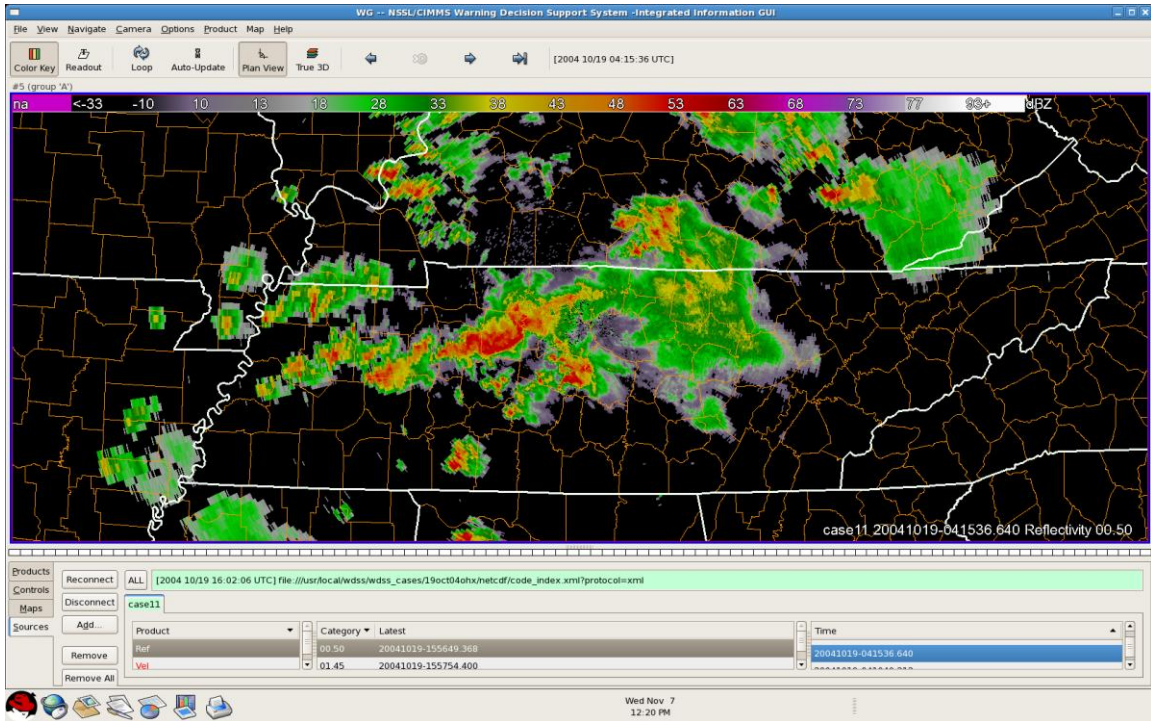


Figure 4.11: A radar composite reflectivity image from the National Weather Service OHX radar site at 0415 UTC on 19 October 2004. The radar site is located northwest of Nashville near Robertson County, TN.

4.2.6 6 November 2005: Saint Charles, MO region

The LSX radar recorded the last squall-line event in this study from 0000 UTC to 0530 UTC 6 November 2005 as an unusually strong low-pressure system tracked across the lower Great Lakes. The northeast to southwest oriented squall-line formed quickly as discrete supercells merged over central Missouri. The squall-line tracked to the east (with individual cells moving northeast along the line) producing numerous reports of hail and wind damage. Figure 4.12 shows the line (with cells merged) moving east from Missouri into Illinois during the overnight hours on 6 November 2005.

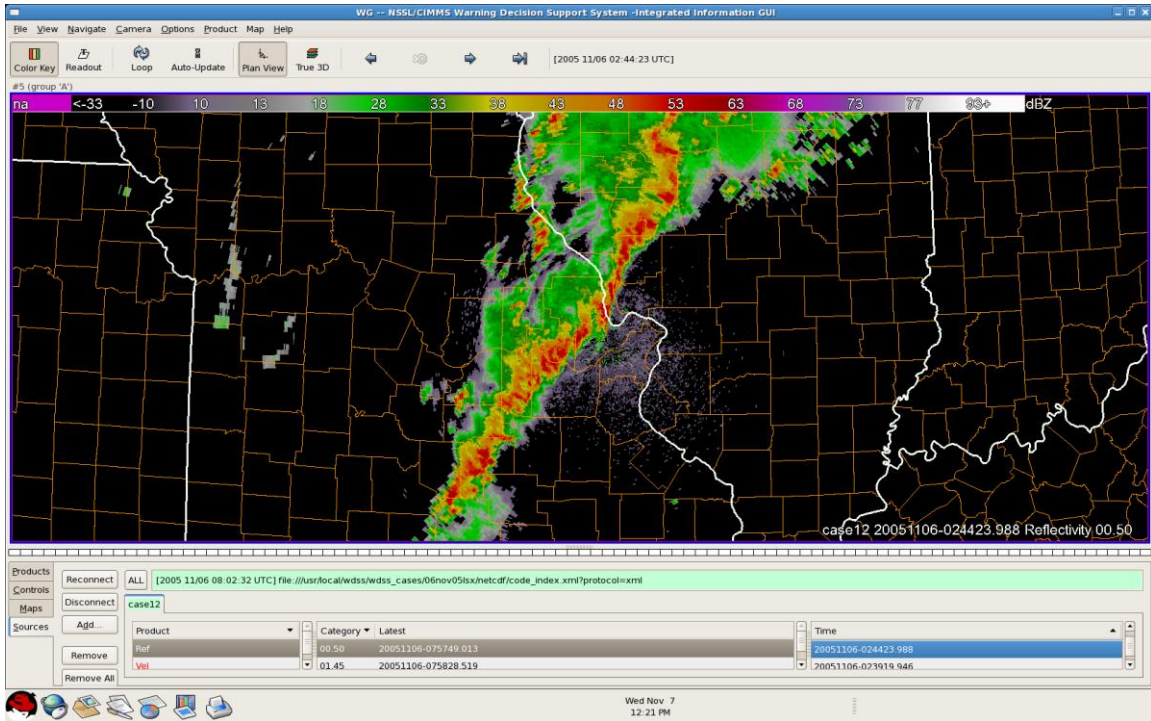


Figure 4.12: A radar composite reflectivity image from the National Weather Service LSX radar site at 0244 UTC on 6 November 2005.

4.3 Multi-cell events

4.3.1 6-7 August 2005: Fort Worth, TX region

The NWS WSR-88D radar site located in Fort Worth, TX (FWS) observed a multi-cell event from 1830 UTC 6 August 2005 to 0030 UTC 7 August 2005 as daytime instability made the environment favorable for intense vertical motion and, therefore, thunderstorms. Since wind speeds at all levels were weak, multi-cell thunderstorms were the main type of convective mode. Figure 4.13 shows generating and collapsing cells to the west and east of the Fort Worth radar site. Since the cells moved very slowly, the risk for flash flooding was enhanced.

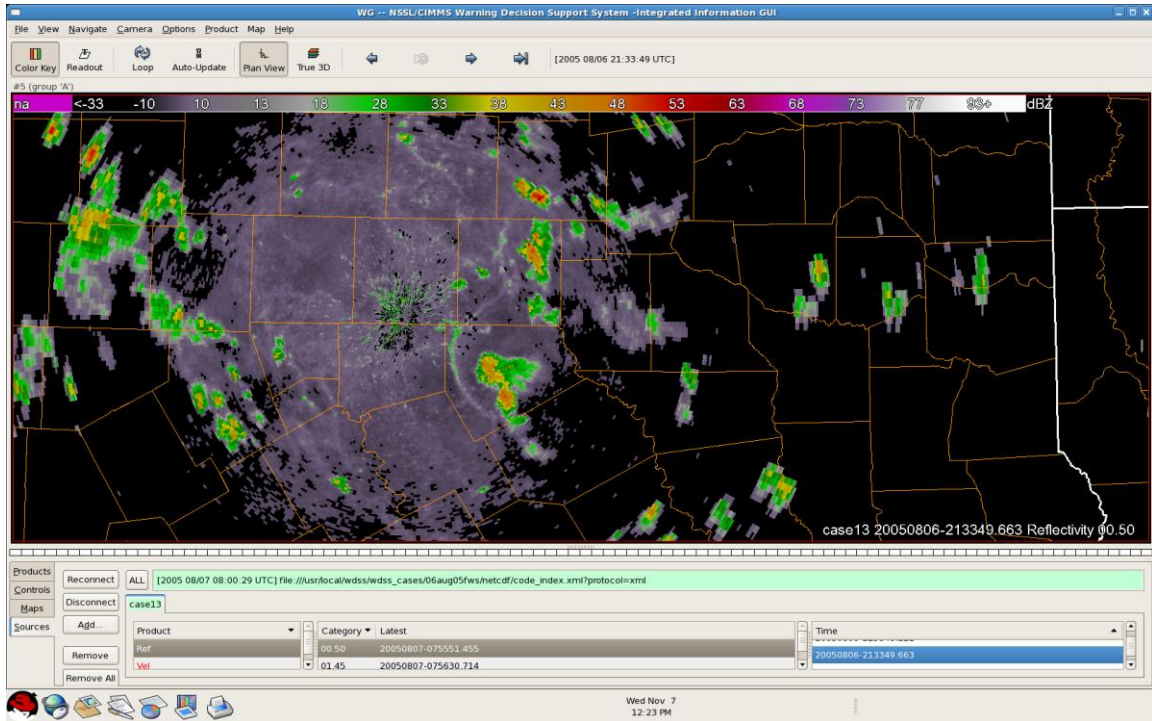


Figure 4.13: A radar composite reflectivity image from the National Weather Service FWS radar site at 2133 UTC on 6 August 2005. The radar site is located south of Fort Worth near Johnson County, TX.

4.3.2 19-20 June 2006: Jackson, MS region

The 19-20 June 2006 multi-cell event occurred from 1800 UTC 19 June 2006 to 0000 UTC 20 June 2006 in the Jackson, MS region of the DGX radar site. The storm propagated across the western side of the radar area as multi-cell thunderstorms formed across central Mississippi and moved west into central Louisiana. Outflow boundaries are a significant contribution to the event as they initiated the storms. Figure 4.14 shows the cells moving west through Mississippi towards Louisiana along the outflow boundary.

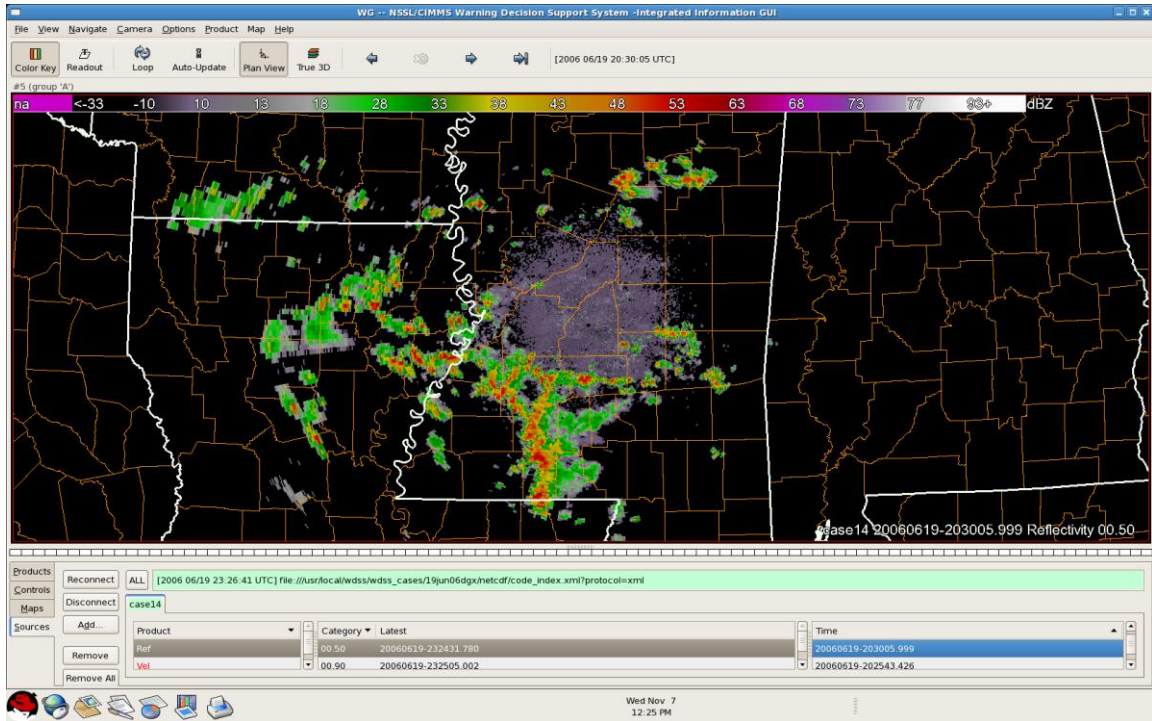


Figure 4.14: A radar composite reflectivity image from the National Weather Service DGX radar site at 2030 UTC on 19 June 2006. The radar site is located east of Jackson near Brandon in Rankin County, MS.

4.3.3 2 July 2006: Tampa Bay, FL region

The mid-summer sea breeze was responsible for these storms as they moved into the Tampa Bay, Florida region and radar site (TBW). The storms moved from east to west (with the surface-925-mb flow) along an outflow boundary easily noticed on radar imagery from 1500 UTC to 2300 UTC. Some of the stronger storms in the case produced hail just to the north of the Tampa Bay metropolitan area. Figure 4.15 shows the cells moving west along the west-moving outflow boundary, produced by the sea breeze earlier in the day, towards the Tampa metropolitan area.

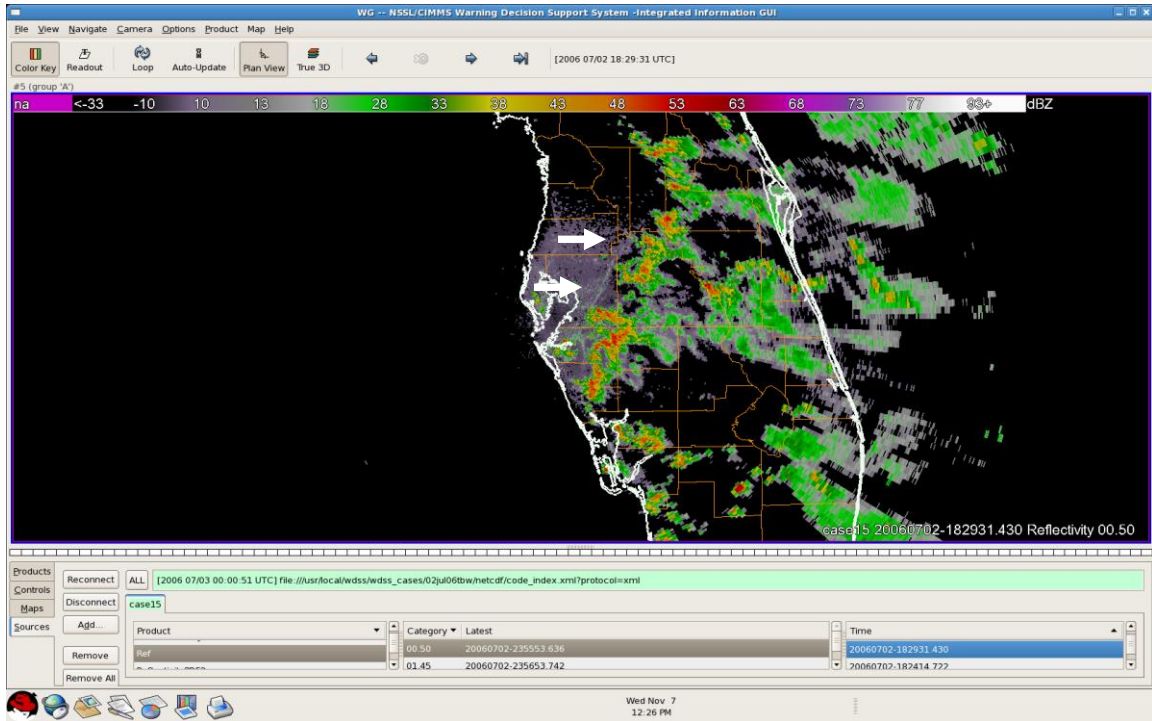


Figure 4.15: A radar composite reflectivity image from the National Weather Service TBW radar site at 1829 UTC on 2 July 2006. The main outflow boundary is indicated with arrows. The radar site is located south of Tampa in Hillsborough County, FL.

4.3.4 28 July 2006: State College, PA region

The fourth case of this type occurred in the State College, Pennsylvania region and near the CTP radar site as a cold front moved from west to east across the region. Multi-cellular storms formed in central Pennsylvania and moved to the east along the front from 1530 UTC to 2030 UTC, staying discrete as they moved through much of eastern Pennsylvania. Figure 4.16 shows cells moving east through Pennsylvania along and ahead of the front on 28 July 2006.

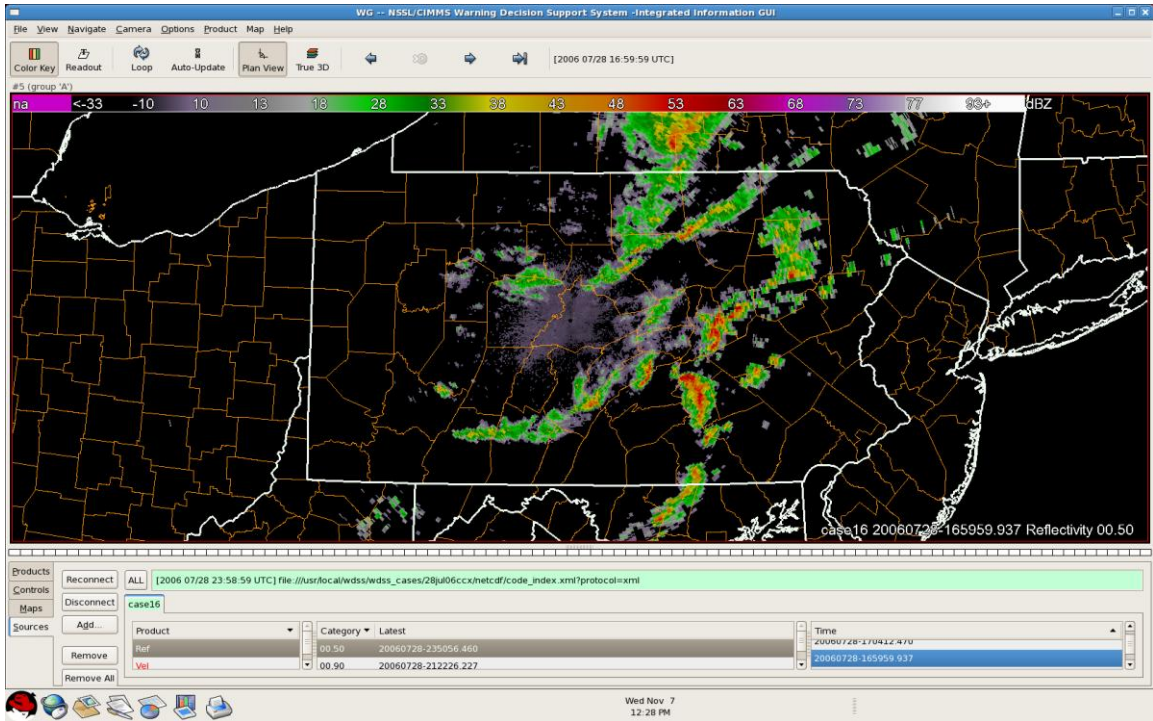


Figure 4.16: A radar composite reflectivity image from the National Weather Service CCX radar site at 1659 UTC on 28 July 2006. The radar is located west of State College in Centre County, PA.

4.3.5 5 July 2004: Baltimore, MD/Washington, DC region

On 5 July 2004 multiple multi-cell storms affected the Baltimore, Maryland/Washington, DC area and were detected by the LWX radar from 1730 UTC to 2330 UTC. An upper-level low moving across eastern West Virginia late in the morning became the focus for initiation later at mid-day, with two distinct cells moving in different directions in northern Virginia late in the afternoon. Figure 4.17 shows the cells tracking in different directions through West Virginia, Maryland, and Virginia during 5 July 2004.

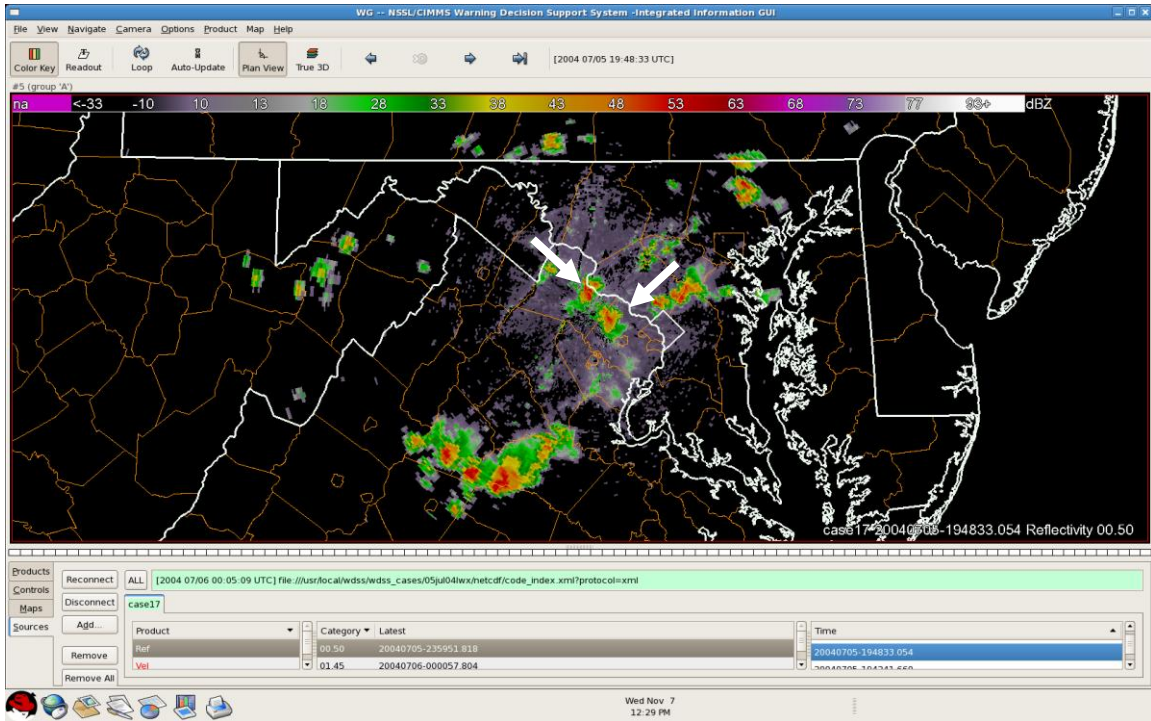


Figure 4.17: A radar composite reflectivity image from the National Weather Service LWX radar site at 1948 UTC on 5 July 2004. The two cells mentioned in the case study description are indicated with arrows. The radar is located northwest of Sterling near Loudoun County, VA.

4.3.6 13 June 2004: Memphis, TN region

NWS NQA radar detected multi-cell thunderstorms in this case on 13 June 2004 which moved west to east across the state. Outflow boundaries are the focus of the case, evident in radar imagery throughout the duration of the event from 1700 UTC to 2330 UTC.

4.4 Summary

This study examined eighteen different supercell/squall-line/multi-cell thunderstorm events, six of each type. There were 25 days worth of radar data, in which 9 were in the supercell category, 8

were in the linear category, and 8 were in the multi-cell category. A total of 53 cells in the following 12 cases were selected for classification:

Date	Site	Radar	# of Cells	Type
12-Mar-2006	Kansas City, MO	EAX	5	Supercell
2-Apr-2006	Memphis, TN	NQA	4	Supercell
28-Mar-2007	Amarillo, TX	AMA	4	Supercell
21-Apr-2007	Amarillo, TX	AMA	5	Supercell
7-Apr-2006	Memphis, TN	NQA	6	Supercell
19-July-2006	Saint Louis, MO	LSX	6	Linear
21-July-2006	Saint Louis, MO	LSX	5	Linear
6-Nov-2005	Saint Louis, MO	LSX	3	Linear
6-Aug-2005	Fort Worth, TX	FWS	3	Multicell
19-Jun-2006	Jackson, MS	JAN	4	Multicell
2-Jul-2006	Tampa Bay, FL	TBW	5	Multicell
28-Jul-2006	State College, PA	CCW	3	Multicell

Table 4.1: Cases and their identified cells (n=53) used for classification in the study.

Out of the 53 cells tracked, 24 were supercells, 14 were linear cells, and 15 were multicells.

Chapter 5

Results

This study uses several different case studies of supercell, linear, and multi-cell events. For each type, there are multiple comparisons which include the mixed-layer convective available potential energy (MLCAPE), 0-3 km storm relative helicity (SRH), 0-6 km mean wind speed, 0-6 km wind shear, average thunderstorm motion and speed, the vorticity generation parameter (VGP), level of the 0°C, -10°C, and -20°C isotherms, and lastly, the u and v-components of the wind at those levels. The first section will explain the process of cell classification by the statistical classifier using pre-existing storm environmental conditions. Next, the isothermal wind method will be compared to other predictive cell motion methods. Third, assessments of parameters by storm type will be made. Finally, the performance of the isothermal wind method will be explored.

5.1 Classification of Cells with Parameter Information by Statistical Classifier

In order to create a dataset for classification, the cells in the study had to be subjectively identified prior to running the classifier. The initial dataset consisted of 12 different dates from 2006-2007 with

53 individually identified cells covering various geographical regions with the majority in the Midwest and South. As in Lack (2007), the cases span different seasons so the classifier would identify storm type independent of time of year and that cases only deal with warm-season precipitation.

Three different classification types were used in the study and are summarized in Table 5.1. The rationale for using the types is explained in Chapter 3.

Classification Type	Description
Pulse Thunderstorm (Multicell)	Low Shear, CAPE, VGP, SRH
Severe QLCS (Linear)	Medium Shear, SRH; Sig. CAPE, VGP
Supercell	Sig. Shear, SRH; Medium CAPE, VGP

Table 5.1: The three classification types used within the classification tree study.

Once the storms were individually identified, a table was generated with all storm attributes and tagged with one of the three categories. This information was used to determine the best use of parameters to determine cell type. The results are classified as a “tree” with nodes at each branch with represents the best “split” of the data (Lack 2007). The result is a deterministic solution that labels the cell in a certain class. For information on the classification tree scheme, consult Lack (2007), Breiman *et al.* (1984), or Burrows (2007).

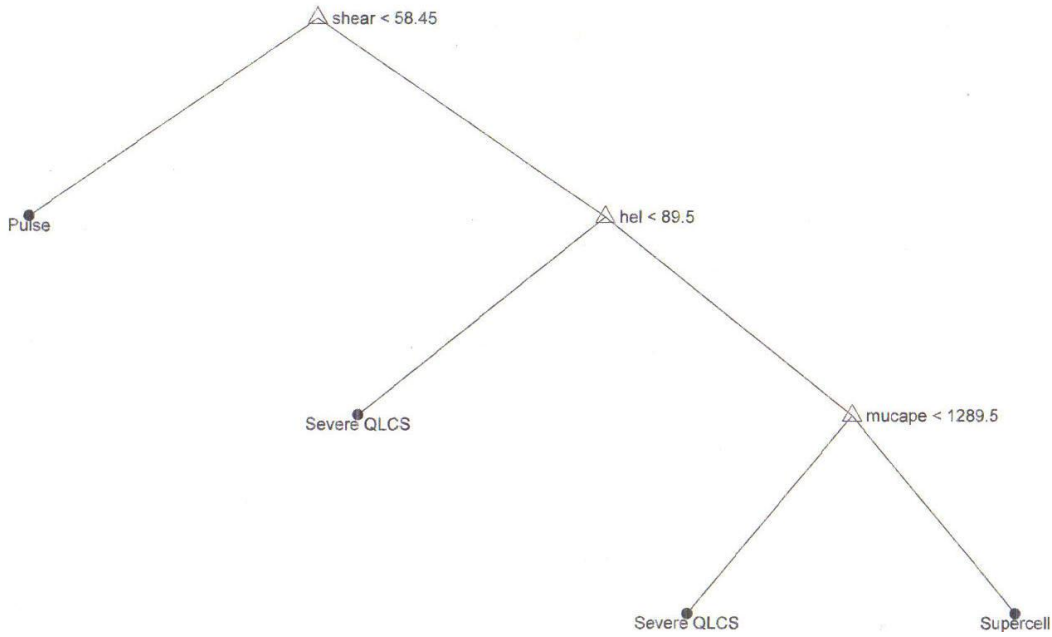


Figure 5.1: Cell classification tree for the 53 cells in the study.

Figure 5.1 shows the classification tree derived from the information obtained of the 53 cells in the study. The first split using a 0-6 kilometer wind shear value of 58.45 kts results in a separation of multicell or pulse thunderstorms (low shear) from severe linear cells and supercells (high speed and/or directional shear), resulting in a correct analysis of all 15 multicells in the study. Table 5.2 is the cell array for the multicells used in the study.

The second split using a 0-3 kilometer storm relative helicity value of $89.5 \text{ m}^2 \text{ s}^{-2}$ separates linear cells with helicities less than $89.5 \text{ m}^2 \text{ s}^{-2}$ from linear cells with helicities greater than $89.5 \text{ m}^2 \text{ s}^{-2}$ or supercells. This split separated weakly rotating from strongly rotating

storms and resulted in a correct analysis of 22 of the 24 supercells used in the study. Table 5.3 is the supercell array for the study.

CAPE (J kg^{-1})	VGP	HEL ($\text{m}^2 \text{s}^{-2}$)	0-6 Shear (kts)	Correctly Identified
840	0.174	20	56.8	Y
1448	0.140	0	39.9	Y
815	0.086	0	35.5	Y
1578	0.123	7	37.4	Y
1129	0.169	19	55.3	Y
1185	0.124	11	37.0	Y
894	0.150	-11	49.7	Y
2888	0.262	34	49.7	Y
3312	0.278	33	47.8	Y
2957	0.179	6	31.4	Y
3174	0.168	-4	30.1	Y
1577	0.142	-5	39.1	Y
270	0.080	39	46.9	Y
1237	0.200	71	56.3	Y
1674	0.254	29	56.9	Y

Table 5.2: Selected output fields for multicells used in the study. VGP is a dimensionless parameter.

The third and last split of the tree using a MLCAPE value of 1289.5 J kg^{-1} designated cells with helicities greater than $89.5 \text{ m}^2 \text{s}^{-2}$ and MLCAPE values of less than 1289.5 J kg^{-1} as linear cells with the rest being supercells. This resulted in a correct classification of 9 of the 14 linear cells. One reason for the drop in accuracy is the severity of the linear cases and the large MLCAPE and SRH values for some of the linear cells, which ultimately were not classified correctly. Table 5.4 is the linear cell array for the study.

CAPE (J kg^{-1})	VGP	SRH (m^2s^{-2})	0-6 Shear (kts)	Correctly Identified
1945	0.370	206	76.7	Y
2997	0.392	190	69.3	Y
3112	0.393	292	67.3	Y
3898	0.319	415	89.9	Y
1629	0.332	187	88.1	Y
1491	0.334	112	87.2	Y
1709	0.313	114	81.0	Y
1664	0.357	265	79.5	Y
2137	0.411	316	81.2	Y
1878	0.361	216	74.5	Y
1500	0.388	318	93.3	Y
2090	0.371	229	87.4	Y
2400	0.415	260	78.1	Y
1945	0.343	230	85.1	Y
1348	0.416	435	103.8	Y
3381	0.380	138	61.1	Y
3303	0.391	159	61.9	Y
2985	0.352	154	63.0	Y
2760	0.488	236	74.0	Y
891	0.191	65	66.2	N
981	0.206	91	65.2	N
1808	0.301	251	65.4	Y
2427	0.367	255	70.2	Y
1890	0.423	402	87.1	Y

Table 5.3: Selected output fields for supercells used in the study. VGP is a dimensionless parameter.

CAPE (J kg^{-1})	VGP	HEL(m^2s^{-2})	0-6 Shear (kts)	Correctly Identified
4876	0.471	59	63.1	Y
5518	0.548	88	67.2	Y
5429	0.522	79	66.6	Y
4005	0.427	61	60.0	Y
5039	0.457	60	63.4	Y
3599	0.523	27	79.7	Y
1374	0.376	37	97.3	Y
2388	0.397	35	73.7	Y
1475	0.37	32	87.5	Y
983	0.255	274	75.1	N
1231	0.251	206	70.8	N
942	0.207	250	77.7	N
744	0.214	239	69.0	N
423	0.229	266	96.7	N

Table 5.4: Selected output fields for linear cells used in the study. VGP is a dimensionless parameter.

The tree which was created with uneven populations of storms satisfied the hypothesis proposed by Lack (2007) in which smaller-scale storms are classified more accurately as the population becomes more uneven. Of the 53 cells, 46 were classified correctly.

5.2 Comparison of Parameters by Cell Type

Figure 5.2 is a box-and-whiskers plot of MLCAPE values for the 53 cells tracked. Average MLCAPE is highest for linear systems, next highest for supercells, and lowest for multicells. The maximum value, (5518 J kg^{-1}) was cell #85 of the July 19, 2006 Saint Charles, MO linear case. The minimum value, (270 J kg^{-1}) was cell #7 in the July

28, 2006 State College multicell case. The linear cells had the largest variability while the supercells had the smallest. Table 5.5 is a summary of MLCAPE values broken down into the three categories.

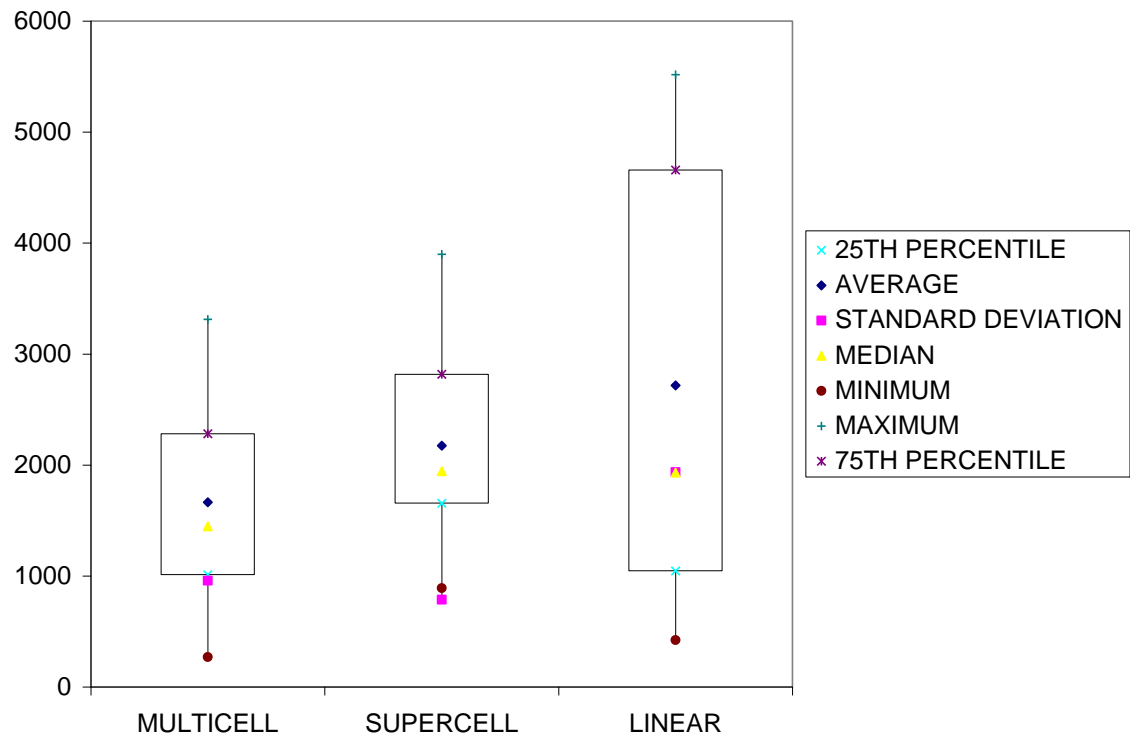


Figure 5.2: A box-and-whisker plot of Mean-Layer Convective Available Potential Energy (MLCAPE) values for cells tested in the study (n=53). Y-axis indicates MLCAPE values in J kg^{-1} .

Units in J kg^{-1}	Multicell	Supercell	Linear
Average	1665.2	2173.7	2716.1
Standard Deviation	958.5	786.8	1934.8
Median	1448.0	1945.0	1931.5
25th Percentile	1011.5	1655.25	1045.0
75th Percentile	2281.0	2816.3	4658.3
Minimum	270.0	891.0	423.0
Maximum	3312.0	3898.0	5518.0

Table 5.5: Indicates the statistical values of MLCAPE for the three types of convective systems. MLCAPE values have different levels of variability for each type.

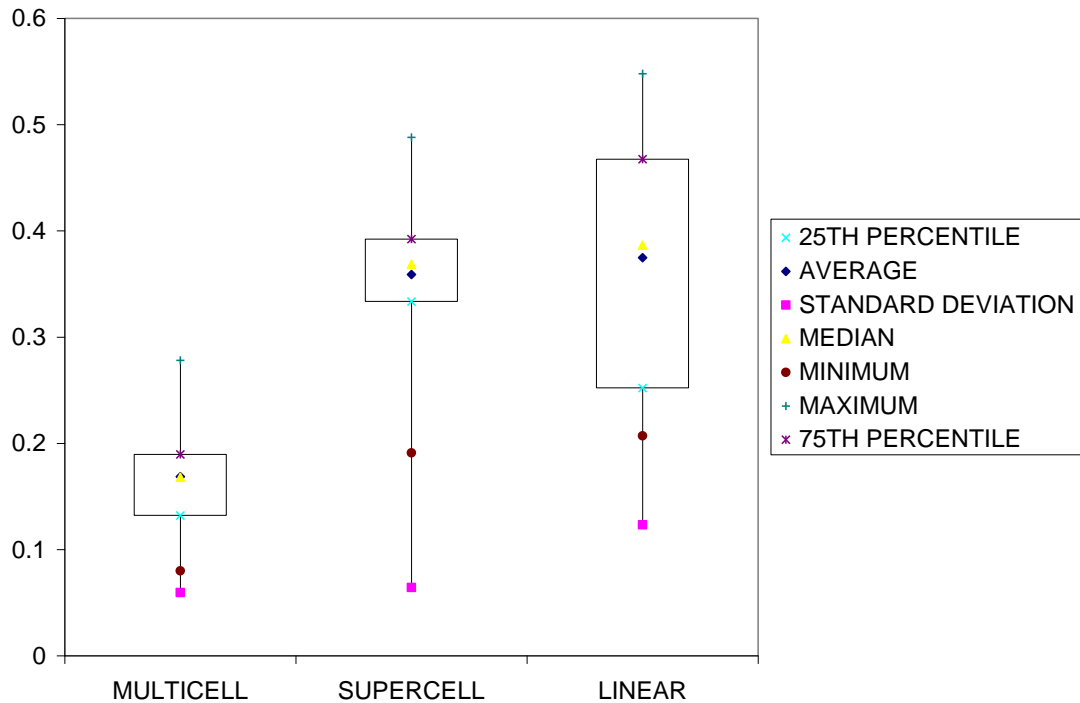


Figure 5.3: A box-and-whisker plot of Vorticity Generation Parameter (VGP) values for cells tested in the study (n=53). Y-axis indicates VGP values.

A box-and-whiskers plot of the 53 cells tracked is shown in figure 5.3. Average VGP is highest for linear systems, next highest for supercells (although the average was almost the same), and lowest for multicells. The maximum value, 0.548 (dimensionless), was again cell #85 from the July 19, 2006 Saint Charles case. The minimum value (0.08) was again from cell #7 in the State College, PA case of July 28, 2006. As with MLCAPE, the linear cells had the highest variability, while the supercells had the lowest. Table 5.6 is a summary of VGP values broken down into the three categories.

	Multicell	Supercell	Linear
Average	0.169	0.359	0.375
Standard Deviation	0.060	0.064	0.123
Median	0.168	0.369	0.387
25th Percentile	0.132	0.334	0.252
75th Percentile	0.190	0.392	0.468
Minimum	0.080	0.191	0.207
Maximum	0.278	0.488	0.548

Table 5.6: Indicates the statistical values of VGP for the three types of convective systems. VGP values have different levels of variability for each type.

Figure 5.4 is a box-and-whiskers plot of 0-3-kilometer storm relative helicity (SRH) values. Average SRH is highest for supercells, next highest for linear systems, and lowest for multicells. The maximum value ($435 \text{ m}^2\text{s}^{-2}$) was cell #6 of the March 12, 2006 Pleasant Hill case (which is the five-state supercell). The lowest value ($-11 \text{ m}^2\text{s}^{-2}$) was cell #32 of the June 19, 2006 Jackson case. Linear cells had the largest variability of SRH, while multicells had the smallest. Table 5.7 is a summary of SRH values broken down into the three types of storms.

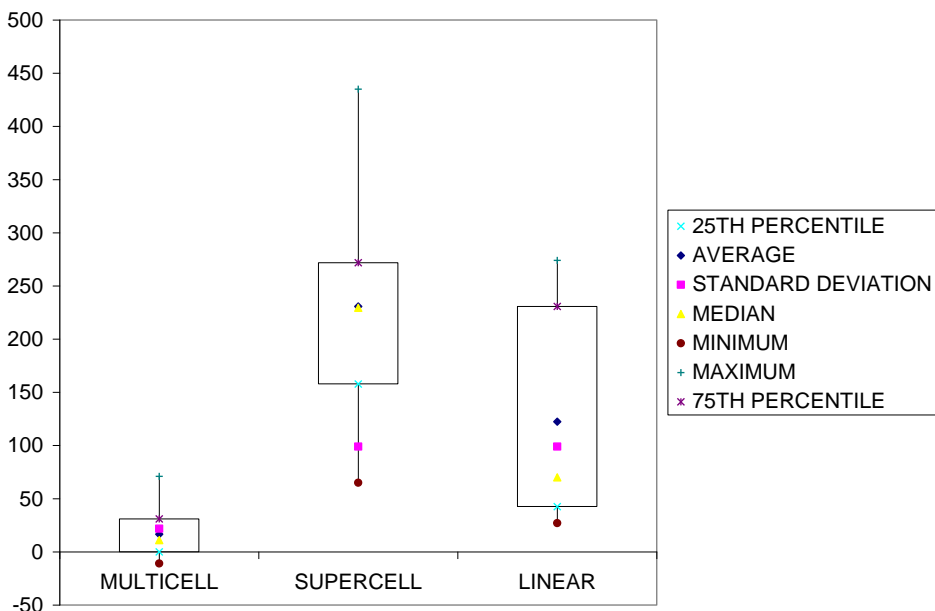


Figure 5.4: A box-and-whisker plot of 0-3 kilometer Storm Relative Helicity values for cells tested in the study ($n=53$). Y-axis indicates SRH values (m^2s^{-2}).

Units in m^2s^{-2}	Multicell	Supercell	Linear
Average	16.6	230.7	122.4
Standard Deviation	21.8	99.0	99.0
Median	11.0	229.5	70.0
25th Percentile	0.0	157.8	42.5
75th Percentile	31.0	271.8	230.8
Minimum	-11.0	65.0	27.0
Maximum	71.0	435.0	274.0

Table 5.7: Indicates the statistical values of SRH for the three types of convective systems. Supercells tend to have the highest SRH values.

Figure 5.5 is a box-and-whiskers plot for mean 0-6-kilometer wind shear for cells tested in the study. Average wind shear is highest for supercells, next highest for linear systems, and lowest for multicells. The maximum value (103.8 kts) was again cell #6 of the

March 12, 2006 Pleasant Hill, MO case. The minimum value (30.1 kts) was cell #43 of the July 2, 2006 Tampa Bay, FL case. Variability of wind shear was highest in supercells, and lowest in linear systems. Table 5.8 is a summary of wind shear values broken down into the three categories of storms.

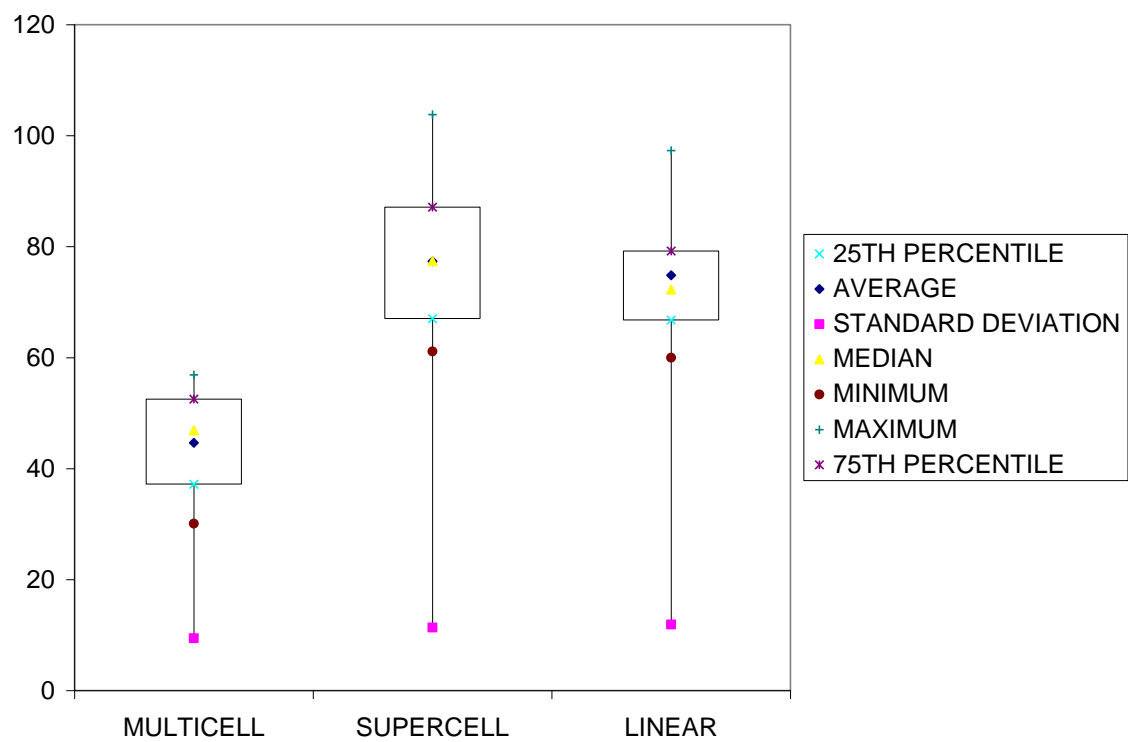


Figure 5.5: A box-and-whisker plot of mean 0-6 kilometer wind shear values for cells tested in the study (n=53). Y-axis indicates wind shear values (kts).

Units in kts	Multicell	Supercell	Linear
Average	44.7	77.4	74.8
Standard Deviation	9.4	11.4	11.9
Median	46.9	77.4	72.3
25th Percentile	37.2	67.0	66.8
75th Percentile	52.5	87.1	79.2
Minimum	30.1	61.1	60
Maximum	56.9	103.8	97.3

Table 5.8: Indicates the statistical values of wind shear for the three types of convective systems. Supercells tend to have the strongest wind shear.

Table 5.9 is a summary of the rankings for supercell, linear, and multicell storm systems for MLCAPE, VGP, SRH, and mean 0-6 kilometer wind shear. It is interesting to note that the linear systems in the study had the highest average MLCAPE and the highest maximum MLCAPE. This may be due to the relatively small sample size in the category and it may also be due to the heightened severity of the pre-existing environmental conditions prior to storm initiation in the linear cases.

	Multicell	Supercell	Linear
MLCAPE Average	3	2	1
MLCAPE Maximum	3	2	1
VGP Average	3	2	1
VGP Maximum	3	2	1
SRH Average	3	1	2
SRH Maximum	3	1	2
Mean 0-6 Wind Shear Average	3	1	2
Mean 0-6 Wind Shear Maximum	3	1	2

Table 5.9: Rankings of the three different types of storms for selected parameters in the study.

5.3 Storm Speed

The 53 cells in the study were also tested for similarities in their velocity versus the velocity of the -20, -10, and 0°C isothermal wind. Figure 5.6 is a scatterplot of supercells as compared to the -20°C isothermal wind speed; linear cells compared to the -10°C isothermal wind speed, and multicells compared to the 0°C isothermal wind speed. That is, the $y=x$ trendline corresponds to the equality of -20, -10, or 0°C isothermal wind speed versus the actual cell velocity for supercells, linear cells, or multicells, respectively. The most enlightening result of Figure 5.6 is the conclusion that with supercells, 23 of the 24 cells tested moved slower than the -20°C isothermal wind velocity, with the 24th exactly at the -20°C isothermal wind velocity. With linear cells, 7 of the 14 moved faster than the -10°C isothermal

wind velocity, 1 moved exactly with the -10°C isothermal wind velocity, and 6 moved slower than the -10°C isothermal wind velocity. Lastly, with multicells, 12 of the 15 moved faster than the 0°C isothermal wind velocity, while the other 3 moved slower. As one moves lower in the atmosphere, the more likely the cell will move faster than the isothermal wind at that level.

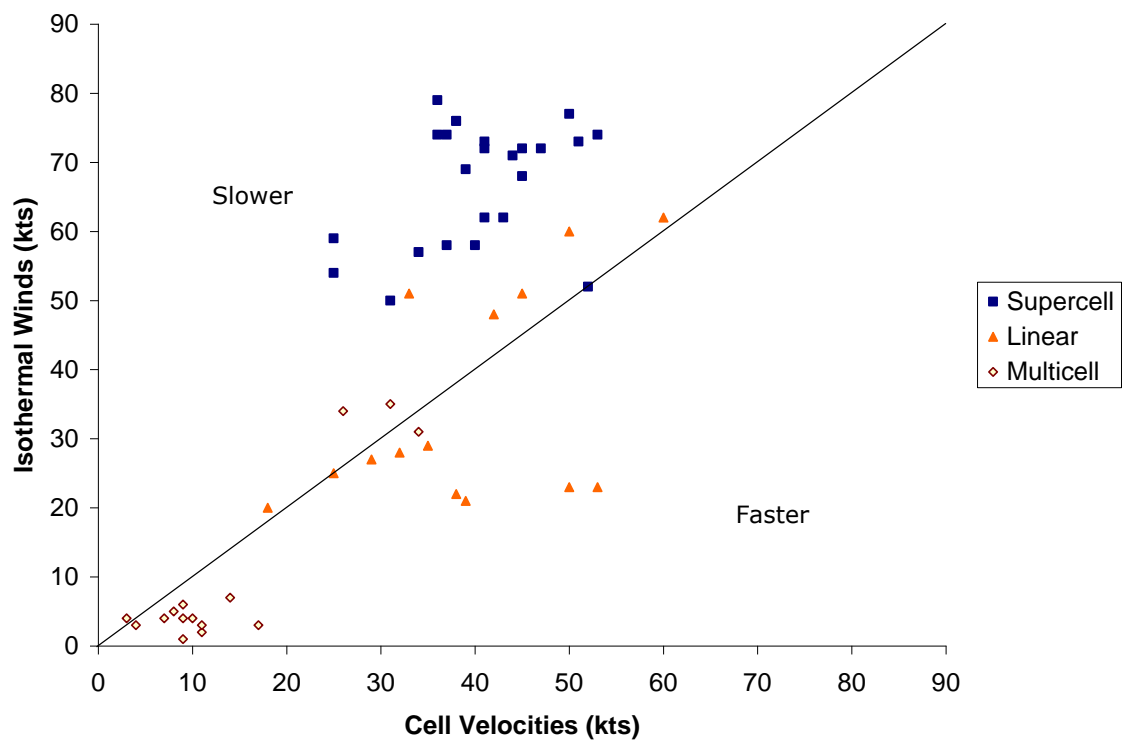


Figure 5.6: Illustration of velocities of cells tested in the study versus Isothermal winds. Y=X trendline indicates the equality of the -20 , -10 , and 0°C isothermal wind velocities to supercell, linear, or multicell velocities respectively.

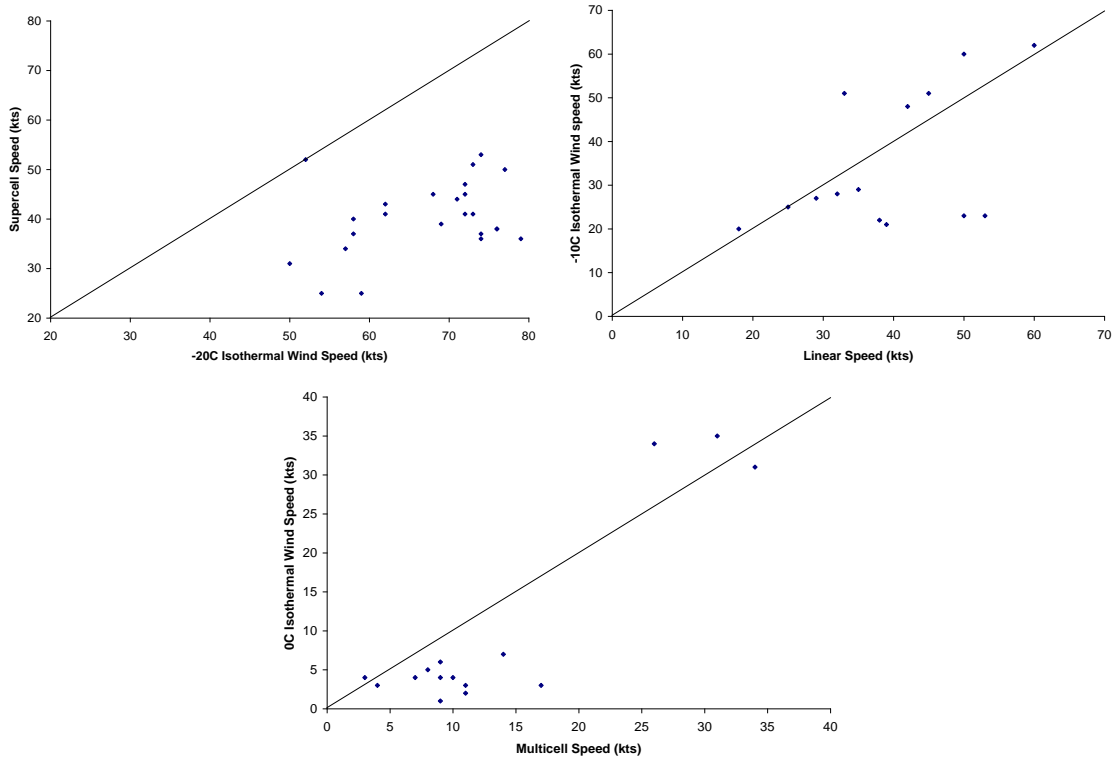


Figure 5.7: Same as Figure 5.14 for A) supercells, B) linear cells, and C) multicells.

5.4 Performance of Isothermal Wind Method

5.4.1 Direction of Motion of Supercells

As explained in Chapter 3, the height of the 0, -10, and -20°C Isotherms, the u and v-wind components at said isotherms, the mean wind speed from 0-6 kilometers, shear from 0-6 kilometers, mean layer convective available potential energy, 0-3-kilometer storm-relative helicity, and the vorticity generation parameter as near-storm environment parameters are derived from RUC-20 data ingested into WDSS-II. The storm motion and velocity data were derived from the

SCIT algorithm within WDSS-II. The conversion of u and v-wind components into degrees involved the following calculations:

$$\text{direction} = \tan^{-1} \left(\frac{u}{v} \right) \text{ if } u \geq 0, v > 0 \quad (5.1)$$

$$= \tan^{-1} \left(\frac{u}{v} \right) + 180^\circ \text{ if } u \geq 0, v < 0 \quad (5.2)$$

$$= \tan^{-1} \left(\frac{u}{v} \right) + 360^\circ \text{ if } u \leq 0, v < 0 \quad (5.3)$$

where u is the u-component of the wind (m s^{-1}) and v is the v-component. The velocity is then calculated:

$$\text{velocity} = \sqrt{u^2 + v^2} \quad (5.4)$$

and the value is converted to knots (operational unit used by NWS) by:

$$\text{knots} = \frac{\text{velocity}}{0.514}. \quad (5.5)$$

As stated earlier, previous research has shown storms with stronger (weaker) updrafts will have motion corresponding with higher (lower) critical winds. Figure 5.11 shows a comparison between actual storm motion and wind direction (in degrees) at the -20°C isotherm for 24 cells tracked in the supercell cases. It can be seen that most of the values lie close to the $y=x$ trendline (storm motion = winds at the -20°C isotherm).

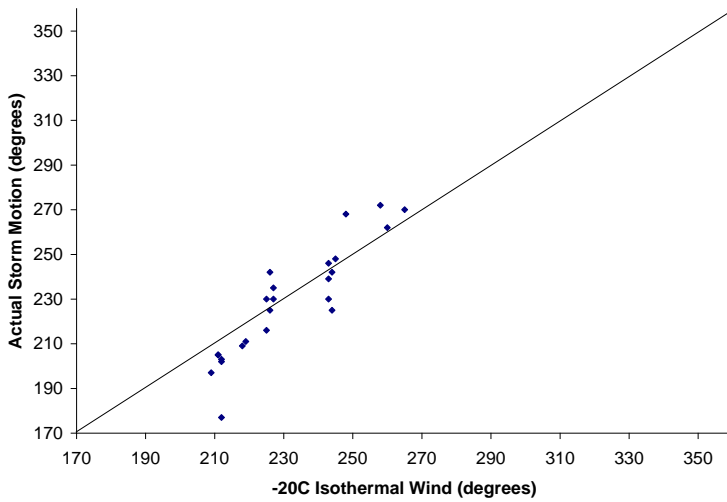


Figure 5.8: A comparison between the Actual Storm Direction of Motion (degrees) and -20°C isothermal wind (degrees) for cells tracked in supercell cases. The solid line is a trendline of equality.

There are 24 data points in Figure 5.8. The most, six, are from the April 7, 2006 case in Memphis, while five each are from the March 12, 2006 case in Pleasant Hill and the April 21, 2007 case in Amarillo. Four are from both the April 2, 2006 case in Memphis and the March 28, 2007 case in Amarillo. On average, results show the actual storm motion to be only 2.7 degrees to the left of the -20°C isothermal wind direction with a standard deviation of 11.8 degrees. A correlation coefficient of 0.91 was found between the -20°C isothermal wind direction and the actual storm motion, meaning that there is quite a similarity between the two values. This similarity demonstrates the usefulness of the -20°C isothermal wind in predicting supercell motion. Mean squared error for the values was 141.5 degrees squared.

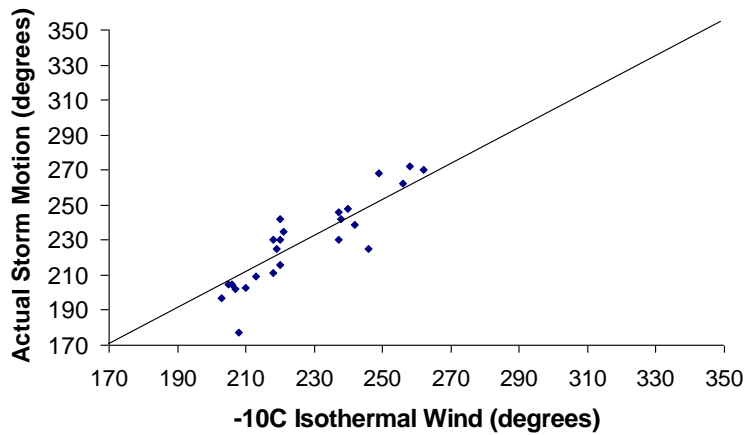


Figure 5.9: A comparison between the Actual Storm Direction of Motion (degrees) and -10°C isothermal wind (degrees) for cells tracked in supercell cases. The solid line is a trendline of equality.

Figure 5.9 shows a comparison of actual storm motion and wind direction at the -10°C isotherm for 24 cells tracked in the supercell cases. Although most of the values once again lie close to the $y=x$ trendline, the correlation coefficient of 0.89 between the -10°C isothermal wind direction and actual storm motion was not as predictive as the -20°C isothermal wind/actual storm motion comparison with a correlation coefficient of 0.91. The similarity in correlation may be due to a lack of variation in wind direction. The -20°C isotherm and -10°C isotherm existed on average at about 550 and 450 hPa, respectively, in the supercell cases where wind direction change may only be 10 or 12 degrees. The results show the actual storm motion to be only 1.6 degrees to the right of the -10°C isothermal wind on average, however, with a standard deviation of

11.9 degrees. Mean squared error for the values was 137.92 degrees squared.

The motion of cells in the supercell cases was also compared to the 0°C isothermal wind direction, which Figure 5.10 illustrates. Most of the values lie close to the $y=x$ trendline again, yet the correlation coefficient of 0.88 between the 0°C isothermal wind direction and actual storm motion was not as high as the -20°C isothermal wind/actual storm motion comparison. On average, the results show the actual storm motion to be 4.8 degrees to the right of the 0°C isothermal wind direction with a standard deviation of 11.7 degrees. Mean squared error for the values was 154.46 degrees squared.

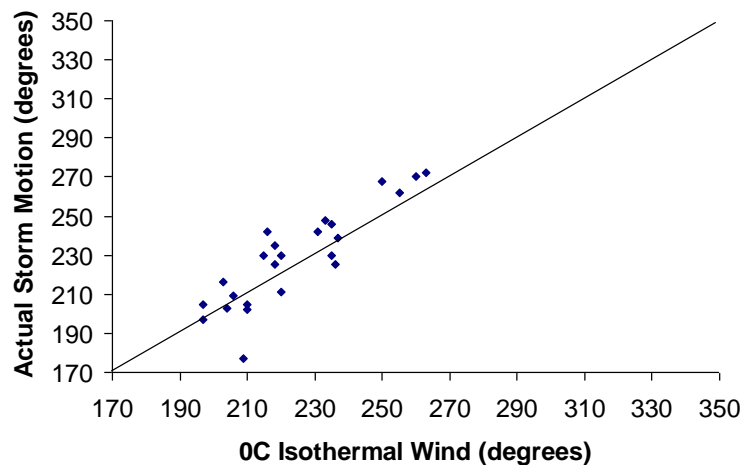


Figure 5.10: A comparison between the Actual Storm Direction of Motion (degrees) and 0°C isothermal wind (degrees) for cells tracked in supercell cases. The solid line is a trendline of equality.

5.4.2 Direction of Motion of Linear Convective Systems

Figure 5.11 shows a comparison between actual storm motion and wind direction at the -20°C isotherm for 14 cells tracked in the linear cases. The most, six, are from the July 19, 2006 case in Saint Charles, while five are from the July 21, 2006 Saint Charles case. Three are from the November 6, 2005 Saint Charles case. It can be seen that all of the values lie above the $y=x$ trendline (actual storm motion to the right of the isothermal wind), although some of the points are a close match to the -20°C isothermal wind direction. On average, results show the actual storm motion to be 28.1 degrees to the right of the -20°C isothermal wind direction with a standard deviation of 18.8 degrees. A correlation coefficient of 0.95 was found between the -20°C isothermal wind direction and linear storm motion, meaning quite a similarity between the two values. Mean squared error for the values was 1121.86 degrees squared.

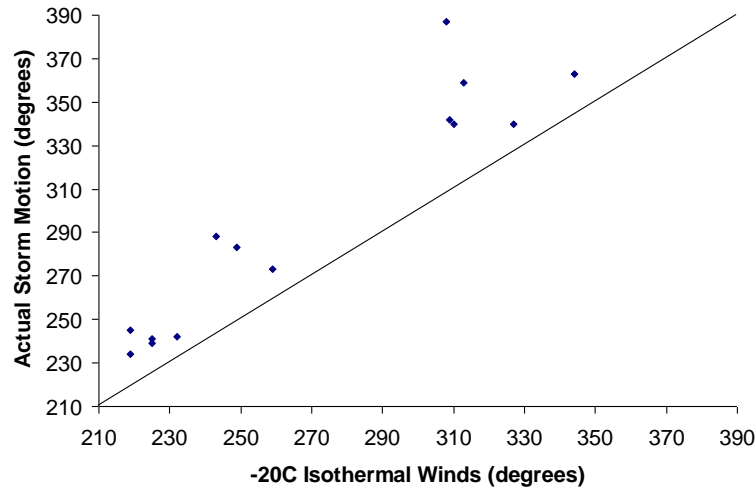


Figure 5.11: A comparison between the Actual Storm Direction of Motion (degrees) and -20°C isothermal wind (degrees) for cells tracked in linear cases. The solid line is a trendline of equality. Values over 360 degrees are cell motions near the 0/360 degree direction discriminator, with 360 degrees added for continuity.

Figure 5.12 shows a comparison of actual storm motion and wind direction at the -10°C isotherm for the 14 cells tracked in the linear cases. Once again, most of the values lie nowhere close to the $y=x$ trendline. On average, actual storm motion is 25.1 degrees to the right of the -10°C isothermal wind direction with a standard deviation of 45.5 degrees. A correlation coefficient of 0.97 was found, which had a higher amount of predictability than the -20°C isothermal wind/linear storm motion correlation coefficient. Mean squared error for the values was 858.64 degrees squared.

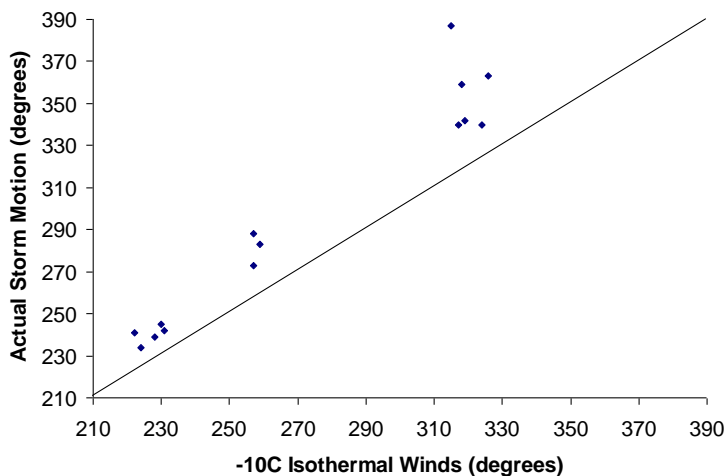


Figure 5.12: A comparison between the Actual Storm Direction of Motion (degrees) and -10°C isothermal wind (degrees) for cells tracked in linear cases. The solid line is a trendline of equality. Values over 360 degrees are cell motions near the 0/360 degree direction discriminator, with 360 degrees added for continuity.

Figure 5.13 illustrates the comparison between actual storm motion and the 0°C isothermal wind direction for the 14 linear cells. On average, the actual storm motion was 16.6 degrees to the right of the 0°C isothermal wind with a standard deviation of 15.7 degrees. The correlation coefficient of 0.97 once again shows the similarity between the 0°C isothermal wind direction and linear storm motion. Mean squared error for the values was 507.07 degrees squared.

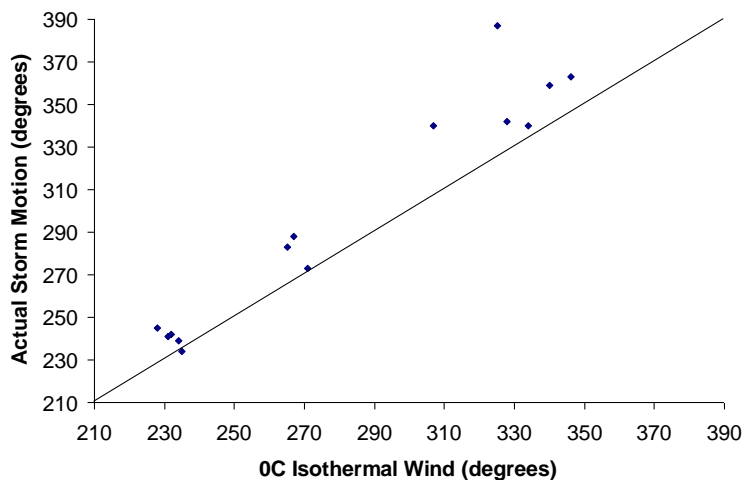


Figure 5.13: A comparison between the Actual Storm Motion (degrees) and 0°C isothermal wind (degrees) for cells tracked in linear cases. The solid line is a trendline of equality. Values over 360 degrees are cell motions near the 0/360 degree direction discriminator, with 360 degrees added for continuity.

For linear cases, the 0°C isothermal wind direction was the most successful predictor of motion, although the -10°C isothermal wind direction was successful as well. Once again this may be due to the small differences in wind direction at the two levels.

5.4.3 Direction of Motion of Multicells

Figure 5.14 shows a comparison between actual storm motion and wind direction at the -20°C isotherm for 15 cells tracked in the multicell cases. The most, five, are from the July 2, 2006 case in Tampa Bay, FL. Four are from the June 19, 2006 case in Jackson, MS, while three are from both the August 6, 2005 Fort Worth, TX case and the July 28, 2006 State College, PA case. Most of the values do not lie anywhere near the $y=x$ trendline as expected. Some of the values,

however, come very close to 0 or 360 degrees, having somewhat of a "nyquist" effect on the correlation coefficient. On average, results show the actual storm motion to be 79.9 degrees to the left of the -20°C isothermal wind direction, with a standard deviation of 102.0 degrees.

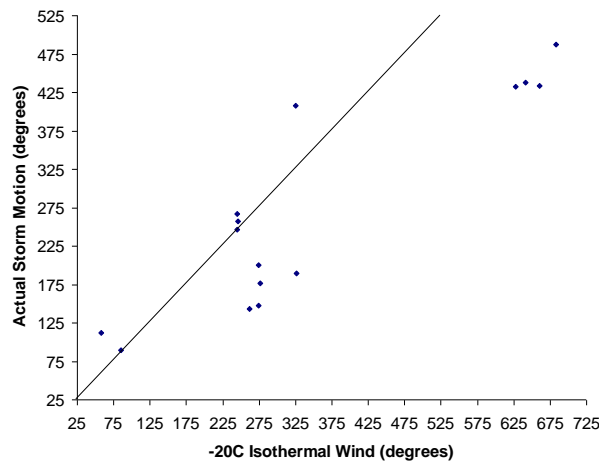


Figure 5.14: A comparison between the Actual Storm Direction of Motion (degrees) and -20°C isothermal wind (degrees) for cells tracked in multicell cases. The solid line is a trendline of equality. Values over 360 degrees are cell motions near the 0/360 degree direction discriminator, with 360 degrees added for continuity.

A correlation coefficient of 0.89 was found between the -20°C isothermal wind direction and multi-cell storm motion. Mean squared error for the values was 1.61×10^4 degrees squared.

The 15 multicells and their motions tracked in the study were then compared to the direction of the -10°C isothermal wind, which figure 5.15 illustrates. The values lie a bit closer to the $y=x$ trendline, yet have a lower linear correlation coefficient of 0.82. On average,

actual storm motion was 96.8 degrees to the left of the -10°C isothermal wind direction, with a standard deviation of 100.6 degrees. Mean squared error for the values was 1.88×10^4 degrees squared.

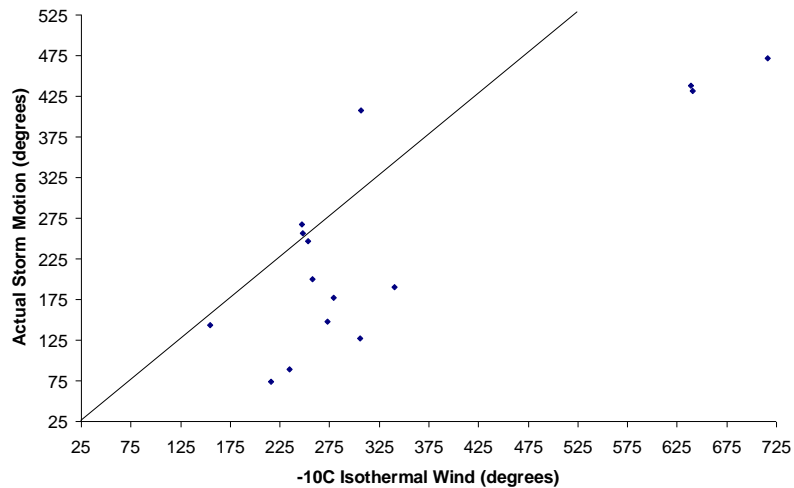


Figure 5.15: A comparison between the Actual Storm Direction of Motion (degrees) and -10°C isothermal wind (degrees) for cells tracked in multicell cases. The solid line is a trendline of equality. Values over 360 degrees are cell motions near the 0/360 degree direction discriminator, with 360 degrees added for continuity.

Figure 5.16 shows a comparison between the actual storm motion of the 15 multicells and the 0°C isothermal wind direction. This comparison had the best correlation coefficient of the three tested for multicells, at 0.91. The average storm motion was 9.1 degrees to the left of the 0°C isothermal wind direction with a standard deviation of 95.6 degrees. Mean squared error for the values was 8620.80 degrees squared. The increased success of the lower-level isotherm in predicting multicell motion backed the hypothesis stated earlier, as eight of the fifteen cells' motions were within 31 degrees of the 0°C isothermal wind direction.

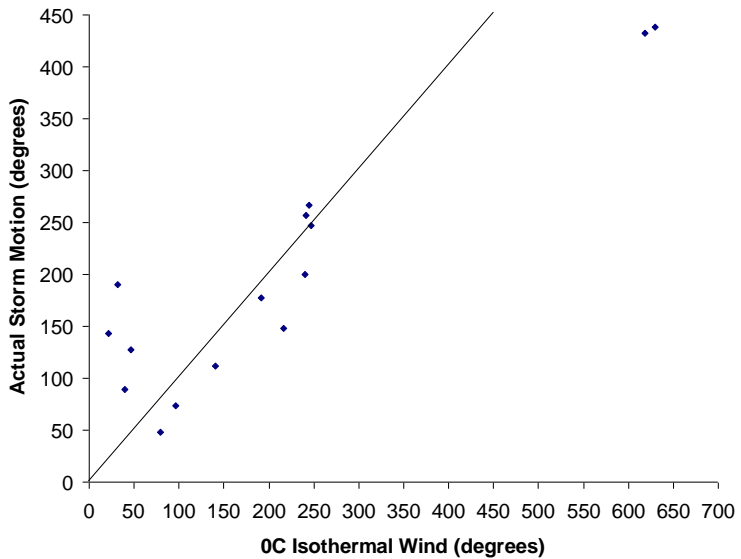


Figure 5.16: A comparison between the Actual Storm Direction of Motion (degrees) and 0°C isothermal wind (degrees) for cells tracked in multicell cases. Values over 360 degrees are cell motions near the 0/360 degree direction discriminator, with 360 degrees added for continuity. The solid line is a trendline of equality.

5.5 Comparison of Isothermal Wind Method versus Other Predictive Cell Motion Methods

As explained in Chapter 2, two of the most widely used nowcasting programs used in atmospheric science (the Spectral Prognosis, or S-PROG, and Warning Decision and Support System-Version II, or WDSS-II) instinctively use storm motion to make nowcasts of precipitation and storm intensity. They automatically track storms and extrapolate motion without regard to storm type or environmental situation. These programs could be further enhanced by classifying severe convective storms by type and subsequently

forecasting the motion of the storms from this information---along with existing environmental conditions. Other procedures for forecasting storm motion based on storm type exist (e.g. Lindsey and Bunkers 2004; hereafter LB04 for supercells, Corfidi et al. 1996 for mesoscale convective complexes; hereafter C96, and Marwitz 1972 for multicells, hereafter M72). They generally use standard-level wind vectors which may not be appropriate in every case (e.g. the 0-6 km wind, 850-300-mb wind, and the 0-10-km wind for studies mentioned earlier, respectively). These wind levels may not always be representative of the surface layer or cloud layer, but are convenient for access as long-standing standard atmospheric levels and model products. On the other hand, the rich variety of model output at numerous levels allows the use of more flexible product selection from Rapid Update Cycle (RUC) or Weather Research and Forecasting Model (WRF) output that could be more closely associated to the motion of a particular storm.

Supercells	σ	MSE
-20°C Isothermal Wind (Y=X)	11.8	141.5
-20°C Isothermal Wind (Best Fit)	7.3	104.3
LB04	10.7	150.9

Table 5.10: Comparison of the standard deviation (in degrees) and mean squared error (in degrees squared) for the Isothermal Wind Method as opposed to the LB04 0-6 kilometer mean-wind method. While the standard deviation is lower for LB04, MSE is lower for the Isothermal Wind Method.

Table 5.10 is a comparison of the standard deviation and mean squared error for two Isothermal Wind Methods versus the LB04 method. The first Isothermal Wind Method correlates the storm direction of motion versus a $y=x$ trendline (actual storm motion = isothermal wind direction at that level). The second Isothermal Wind Method correlates the storm direction of motion versus the line of best-fit for the type of storm indicated.

Figure 5.17 shows a comparison between actual storm motion and wind direction (in degrees) at the -20°C isotherm for 24 cells tracked in the supercell cases. The equation (storm direction algorithm) placed in the figure corresponds with the line of best fit. The other line with slope $m = 1$ indicates a $y=x$ relationship. The 24 supercells tested in the study were tracked using the LB04 method and compared to the Isothermal Wind Method. The Isothermal Wind Method had the same linear correlation as LBO4, with a larger standard deviation and smaller mean squared error. The supercell storm motion algorithm from the line of best fit can be expressed as

$$C_S = 1.3258d_{-20} - 78.041 \quad (5.1)$$

with d_{-20} = wind direction in degrees at the -20°C isotherm.

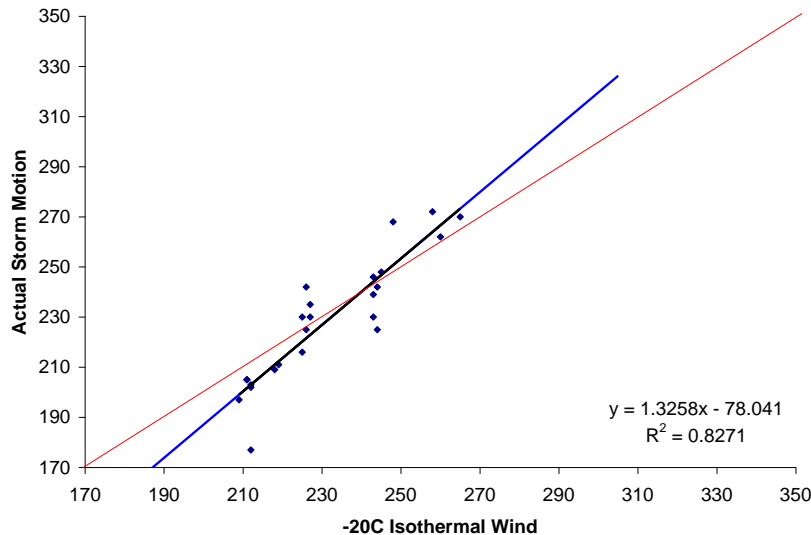


Figure 5.17: A comparison between the Actual Storm Direction of Motion (degrees) and -20°C isothermal wind (degrees) for cells tracked in supercell cases. The red line is the $y=x$ trendline, while the blue/black line is the line of best fit.

Linear Systems	σ	MSE
-10°C Isothermal Wind ($Y=X$)	16.0	858.6
-10°C Isothermal Wind (Best Fit)	9.4	191.6
C96	16.6	876.4

Table 5.11: Comparison of the standard deviation (in degrees) and mean squared error (in degrees squared) for the Isothermal Wind Method as opposed to the C96 mean 850-300 mb wind method. Standard deviation and mean square error are smaller for the Isothermal Wind Method.

Table 5.11 is a comparison of the same statistical parameters for the Isothermal Wind Method versus the C96 method. The 14 linear cells tested in the study were tracked using the C96 method. Figure 5.18 shows a comparison of actual storm motion and wind direction at the -10°C isotherm for the 14 cells tracked in the linear cases. The Isothermal Wind method again had a smaller standard deviation and mean squared error.

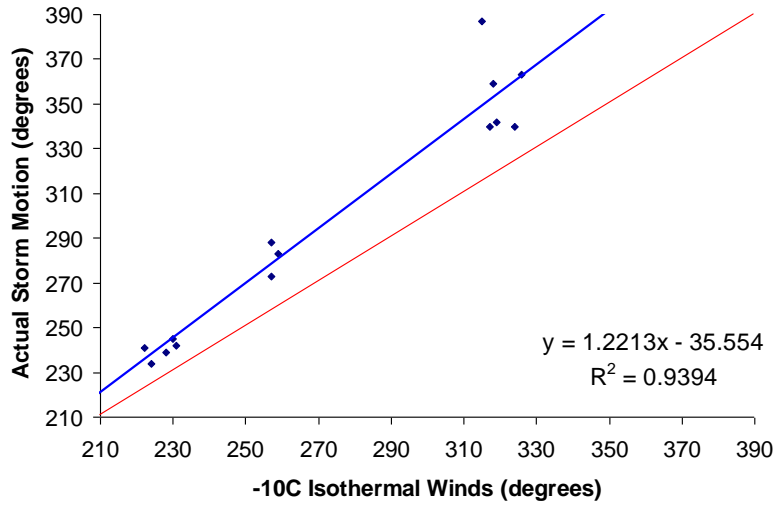


Figure 5.18: A comparison between the Actual Storm Direction of Motion (degrees) and -10°C isothermal wind (degrees) for cells tracked in linear cases. The red line is the $y=x$ trendline, while the blue line is the line of best fit. Values over 360 degrees are cell motions near the 0/360 degree direction discriminator, with 360 degrees added for continuity.

Multicells	σ	MSE
0°C Isothermal Wind ($Y=X$)	95.6	8620.8
0°C Isothermal Wind (Best Fit)	26.9	2096.9
M72	119.8	13694.5

Table 5.12: Comparison of the standard deviation (in degrees) and mean squared error (in degrees squared) for the Isothermal Wind Method as opposed to the M72 0-10 km mean wind method. The correlation coefficient is more predictive with less error using the Isothermal Wind Method.

The linear cell storm motion algorithm from the line of best fit can be expressed as

$$C_L = 1.2213d_{-10} - 35.554 \quad (5.2)$$

with d_{-10} = wind direction in degrees at the -10°C isotherm.

Table 5.12 is the comparison of the Isothermal Wind Method versus the M72 method. The 15 multicells in the study after testing by the Isothermal Wind Method were tracked again using the M72

method. Figure 5.19 shows a comparison between the actual storm motion of the 15 multicells and the 0°C isothermal wind direction. The Isothermal Wind Method had a smaller standard deviation and mean squared error.

The multi-cell storm motion algorithm from the line of best fit can be expressed as

$$C_M = 0.5625d_0 + 80.910 \quad (5.3)$$

with d_0 = wind direction in degrees at the 0°C isotherm.

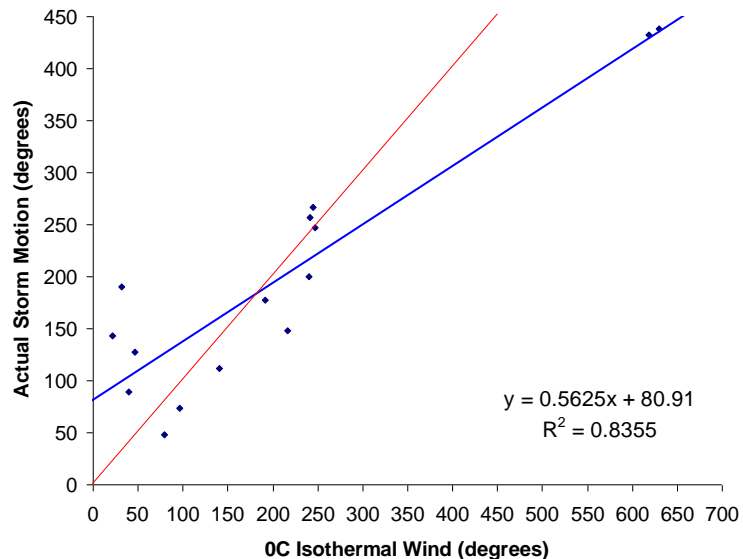


Figure 5.19: A comparison between the Actual Storm Direction of Motion (degrees) and 0°C isothermal wind (degrees) for cells tracked in multicell cases. 360 degrees is added in some cases for continuity. The red line is the Y=X trendline, while the blue line is the line of best fit.

Type of Storm	Algorithm
Supercell	$(C_S) = 1.3258d_{-20} - 78.041$
Linear	$(C_L) = 1.2213d_{-10} - 35.554$
Multicell	$(C_M) = 0.5625d_0 + 80.910$
Where	d_{-20} =wind direction in degrees at the -20°C isotherm. d_{-10} =wind direction in degrees at the -10°C isotherm. d_0 =wind direction in degrees at the 0°C isotherm.

Table 5.13: Storm direction algorithms for the three types of storms.

The derived algorithms for cell direction of motion (Table 5.13) for supercells (noted C_S), linear cells (noted C_L), and multicells (noted C_M) included the isothermal wind direction at the level inferred to have the highest linear correlation for that type of storm. These algorithms can be used in future studies to estimate storm motion. Some limitations exist within the algorithms as they were formulated using a limited number of case studies, without regard to storm speed.

The Isothermal Wind Method used for predicting cell motion had a higher level of success than previous methods. Predictability remained high no matter what the method in all cases, although multicell cases had more error. This may be a function of the particular case, or it may be a case of error within the SCIT cell-tracking algorithm, especially where storms are dominated by ambient low-level winds. If this is the case, however, one can “toggle” the Isothermal Wind Method at lower (higher) isotherms to obtain low

(high)-level wind components. This proves useful as Table 5.14 shows the range of isothermal levels in the study.

Isotherm	Pressure (hPa)
-20°C	550-675
-10°C	450-575
0°C	375-475

Table 5.14: Range of isothermal levels (hPa) for selected isotherms in the study.

5.6 Errors

During the analysis of cells selected for the study several different sources of error have surfaced. These errors exist both with the comparison of isothermal winds to storm motion as well as classification of the cells. Some errors impacted the final results, yet are useful to document for careful consideration during future studies of this type.

The first source of error is the sample size of the study; in order to obtain the ideal-sized tree, a dataset with hundreds or perhaps even thousands of cells from hundreds of cases are needed (Lack 2007). With a large dataset, the scheme of the classification tree will make better distinctions among cells with large data arrays as described in Section 5.2.

Even though the classification tree had a success rate of 0.868 (46/53), it only had a success rate of 9/14 (0.643) for the linear cells included in the study. This may be due to the fact that 4 of the 6

linear cases included in the study were hybrid cases in which the convective mode at initiation was different from the convective mode at the end of the case. Many of the linear cells in those cases were possibly at one time supercells and this contributes to their supercell characteristics. When looking at the classification tree, a distinction was made between linear cells and supercells by MLCAPE. The distinction is a way of looking at the instability throughout the entire column of the cell. Intuitively, one would guess that this value would be higher in supercells. The problem with this assumption was that many of the values of MLCAPE in the linear cells were higher than those of the supercell cases, resulting in misclassified cells. VGP was never used as a discriminator between cells in this study; it was used in the Lack (2007) study and successfully partitioned rotating storms from non-rotating storms more effectively than the 0-6 kilometer mean shear value used as a discriminator in this study.

The selection of the -20, -10, and 0°C isotherms as non-mandatory levels to look at storm motion was an effective choice. A more effective choice, however, may have been larger-spaced isothermal selection with a level closer to the surface. The linear correlation of storm motion to isothermal wind direction may be higher with selected thresholds of every 15°C, or 20°C, instead of the 10°C spacing used in this study. Furthermore, isotherms above 0°C are

situated closer to the surface, and may be able to account for the high variability of multicell motion. The small sample size also may have had an effect on the overall success of the correlations calculated.

Another source of error may include the calculation of the average direction and velocity of storm motion in the study. The method used the direction and velocity of the cell in each radar scan throughout the life of the cell and averaged those values into a “final” direction and velocity for use in statistical analysis later. For multicells and linear cells with little direction change throughout the life of the storm, this is an effective way to gauge storm motion. However, with supercells (especially high-precipitation supercells as noted by Bunkers *et al.* 2000), motion (in direction and speed) can vary, and an average amongst the whole cell life may fail to properly weigh the importance of key direction changes, splits, or mergers into and out of the cell. For example, a supercell with a low-level mesocyclone may deviate up to 20 degrees from previous motion (as shown with 2 cells in this study). A way to correct the problem would be to automate the detection of direction change within storms with a size of greater than a selected threshold for a particular case. This would give a more accurate and faster description of cell motion and velocity, allowing nowcasters more time to prepare for severe weather conditions.

Another source of error lies within the formulation of the algorithms to approximate cell motion. The algorithms were formulated using a line of best fit, yet the number of cells used to make the line of best fit was less than optimal. Outliers within a storm type may change the line of best-fit drastically, and therefore, increase the percentage of error in forecasting the motion of a specific storm type. Even with the errors that exist, the validity of the algorithms can subsequently be tested in future studies with more cases and cells.

Data assimilation within WDSS-II may have also contained errors. An incorrect selection of cells can affect or even corrupt overall results. The SCIT algorithm within WDSS tends to merge cells together when in very close proximity (Jankowski 2006, Johnson *et al.* 1998), small in length along a radial, or shallow cells not covered in consecutive radar scans. This tends to happen in linear cells with large areas of the same reflectivity, much like the cells included in this study. A way to rectify the problem is to perhaps automate the selection of cells with different mesoscale features with an area-based tracking algorithm as best described in Johnson *et al.* (1998). This algorithm can effectively delineate between cells with similar attributes.

5.7 Discussion

Examining data among the three types of cells in the study showed a strong linear correlation between the -20°C isothermal wind direction and supercell motion, a strong linear correlation between the -10°C isothermal wind direction and linear cell motion, and a significant linear correlation between the 0°C isotherm and multicell motion. Cell tracking by isothermal wind direction also performed with a higher level of predictability than previous studies. Lastly, many of the cells used in the study were correctly identified by the statistical classifier using near-storm environmental model data. Knowing the convective mode of storms at genesis helps the forecaster to make a deterministic evaluation of storm motion, velocity, severity, and duration in a given area. Thus, finding a correlation between storm type and storm motion gives forecasters the chance to make more accurate forecasts of storm type and where the storms will have an effect.

The results of the study in applying near-storm environment model data to the cells identified are summarized in the following points:

- Supercell thunderstorms tend to move with the -20°C isothermal wind direction; have the highest variability in 0-6

kilometer wind shear and move slower than the -20°C isothermal wind speed.

- Cells in linear systems were found to move with the -10°C and -20°C isothermal wind direction; have the highest variability in mean layer CAPE, 0-3 kilometer storm relative helicity, and the vorticity generation parameter and have no propensity to move slower or faster than the -10°C isothermal wind speed.
- Multicell thunderstorms have a strong linear correlation to the 0°C isothermal wind direction; typically have the lowest CAPE, shear, VGP, and SRH values and move faster than the 0°C isothermal wind speed.

The results of the study in applying classification tree techniques are summarized forthwith:

- Cell classification with smaller non-rotating storms was more accurate; the discriminators used to separate types of storms made intuitive sense.
- Cell discriminating between cells in linear systems and supercells using the MLCAPE parameter resulted in a less than desirable success rate; the use of VGP is a more successful

parameter to use as documented by Lack (2007) and other previous studies.

- Hybrid cases as theorized by Lack (2007) seem to decrease the success rate of the statistical classifier; more research is needed in the area to evaluate the significance of this claim.
- Additional storm attributes may be needed to more successfully classify types of storms.

As discussed earlier, the primary goal of evaluating storm type versus storm motion is to give forecasters a better chance of telling the public the potential dangers of a given type of storm in a forecast area. Classification can be used in real-time by forecasters to monitor particularly severe storms, or to make a historical archive of storms for different inter-annual time frames. As explained in Lack (2007), the primary goal of the classification tree scheme is to use the information given by the model data to input into nowcasting products for cell morphology purposes.

The objectives and hypotheses for this research were listed for this study in Chapter 1. The research obtained in this study first notes that different pre-existing meteorological conditions exist for supercell, linear, and multicell systems. Second, the classification tree system successfully classified different storm types in most cases. Looking at storm motion alone helps in the forecasting process, but does not

make a forecast alone. The understanding of storm morphology and the addition of storm type, if not included or even neglected in a nowcast, may mean severe conditions can be underestimated, missed, or even ignored.

Chapter 6

Summary and Conclusions

6.1 Summary

Defining conclusively storm motion by storm type has shown to be one of the least researched topics in the field of atmospheric science. The aim of this work was to discover if better forecasts of storm motion could be made by classifying storm type prior to using and selecting an appropriate nowcast scheme. Nowcasting programs such as WDSS-II can be further enhanced by classifying severe convective storms by type and subsequently forecasting the motion of the storms from this information along with pre-existing environmental conditions. This study's second purpose was to identify the pre-existing meteorological conditions associated with three different types of convective systems and to use a statistical classifier to separate cells of different type.

Several different case studies located near NWS radars in Kansas City, MO (EAX), Memphis, TN (NQA), Amarillo, TX (AMA), Saint Louis, MO (LSX), Hastings, NE (UEX), Atlanta, GA (FFC), Nashville, TN (OHX), Fort Worth, TX (FWS), Jackson, MS (JAN), Tampa Bay, FL (TBW), State College, PA (CCX), Sterling, VA (LWX), and Columbus Air Force Base, MS (GWX) were examined in this study. Of the cases

examined for cell classification, there were 5 supercell cases, 3 linear cases, and 4 multicell cases. Each of the 18 cases was analyzed using WDSS-II which uses SCIT to track a cell's velocity and direction of motion. The motion of the cells in the 12 cell-classification cases were then compared to near-storm environmental RUC-20 data of isothermal wind direction and velocity at the -20, -10, and 0°C isotherms. Although all of the cases were not used for cell-classification, the other 6 cases were used as quality-control (i.e. continuity) for values calculated in the 12 cell-classification studies. Table 6.1 is a summary of all cases in the study.

Date	Radar Site	Abbr.	Storm Type
12-Mar-2006	Kansas City, MO	EAX	Supercell
02-Apr-2006	Memphis, TN	NQA	Supercell
28-Mar-2007	Amarillo, TX	AMA	Supercell
21-Apr 2007	Amarillo, TX	AMA	Supercell
04-May 2003	Topeka, KS	TOP	Supercell
07-Apr-2006	Memphis, TN	NQA	Supercell
19-Jul-2006	Saint Louis, MO	LSX	Linear
21-Jul-2006	Saint Louis, MO	LSX	Linear
9-Jul-2004	Hastings, NE	UEX	Linear
2-May-2003	Atlanta, GA	FFC	Linear
19-Oct-2004	Nashville, TN	OHX	Linear
6-Nov-2005	Saint Louis, MO	LSX	Linear
6-Aug-2005	Fort Worth, TX	FWS	Multicell
19-Jun-2006	Jackson, MS	JAN	Multicell
2-Jul-2006	Tampa Bay, FL	TBW	Multicell
28-Jul-2006	State College, PA	CCX	Multicell
5-Jul-2004	Washington, DC	LWX	Multicell
13-Jun-2004	Memphis, TN	NQA	Multicell

Table 6.1: Cases used in the study.

Overall, the -20°C isotherm did well in predicting storm motion for all types, but did best with supercells. On average, supercells moved 2.7 degrees to the left of the -20°C isothermal wind direction with a correlation coefficient of 0.91. From looking at these values, it is concluded that wind direction at the -20°C isotherm is a proper indicator of supercell motion. The -10 and 0°C isothermal wind directions were not as predictive. However, the 0°C isotherm had

some success in predicting multicell motion. Research findings in this study also indicated that as one moves closer to the surface, the more likely the cell at that level will move faster than the winds at that same level. Multicells had the lowest variability and the lowest values of all parameters tested in the study, while supercells and linear cells had the highest.

The second objective of this cell was to determine if the statistical classifier could delineate between cells of different types based on the pre-existing environmental conditions obtained earlier in the study. Values of mean-layer convective available potential energy, 0-3 kilometer storm relative helicity, vorticity generation parameter, and 0-6 kilometer wind shear were gathered for 53 cells. The information from the cells was placed in the statistical classifier. The statistical classifier correctly identified all 15 of the multicells, 22 of the 24 supercells, and 7 of the 14 linear cells, for a total success rate of 0.830 (44 of 53 correctly identified cells).

6.2 Future Work

Future work for the evaluation of storm type versus storm motion includes the accounting and solving of several errors. Such errors as small sample size, hybrid cases, separating parameters,

selection of isotherms, calculation of parameters, and data assimilation are the foundation for future work to be conducted on this topic.

In order to obtain the ideal-sized tree, a dataset with hundreds or perhaps even thousands of cells from hundreds of cases are needed. This leads to future research of perhaps an automated system of classifying and a historical archive of thousands of cells for study. Being able to consult the historical archive for research would lead to more consistent results with storm motion and cell classification. Hybrid cases in future work could solely be used for a separate study; this would effectively evaluate the usefulness of the classifier in delineating cells of different types on an intra-case basis. Future work to the tree classification system can include parameters of azimuthal shear, as well as parameters derived from dual-polarization radar (Lack 2007). A study of merging or splitting cells may also be needed to update the classifier with those cells that may have different physical characteristics than others used in this study.

Other research that can be conducted in the future may be to divide the linear cases into the divisions made by Bluestein and Jain (1985). This allows researchers to determine the properties of back-building cells and embedded-areal cells. This may lead to an explanation of the severity of linear cells in the cases in this study. The selection of isotherms closer or further from the surface may give

nowcasters a better correlation between isothermal wind and linear/multicell systems. Lastly, the improvement of nowcasting products with increased automation will give forecasters a chance to use the data gathered in real-time, and subsequently, forecast for storm severity or hazardous weather conditions with higher levels of accuracy and timeliness.

The addition of the future work stated above, along with the research presented in this study will be more useful for a more accurate forecast of storm motion by storm type.

Appendix A: Cell Identification Matlab Script:
numberID_simp.m
(Lack 2007)

```
%individual identification change time and dates for all
load ('14jul07epz/reflectivity/T20070714_040001.txt');
for i=1:256
    for j=1:256
        if (T20070714_040001(i,j)<=0)
            T20070714_040001(i,j)=0;
        end
    end
[m n]=size(T20070714_040001);
identifycells(30,T20070714_040001);
load ('labeled.txt');
tempmax=max(labeled);
numberofcells=max(tempmax);
imagesc(labeled);
caxis([0 numberofcells]);
colorbar;
%radar data
load ('14jul07epz/echotop/ECHOTOP20070714_040001.txt');
load ('14jul07epz/mesh/MESH20070714_040001.txt');
load ('14jul07epz/posh/POSH20070714_040001.txt');
load ('14jul07epz/vil/VIL20070714_040001.txt');
load ('14jul07epz/vildensity/VILDENSITY20070714_040001.txt');
%ruc 252 data
load ('14jul07epz/mucape/MUCAPE20070714_040000.txt');
load ('14jul07epz/srhelicity/SRHelicity0_3km20070714_040000.txt');
load ('14jul07epz/uwind_0_6km/UWIND_0_6km20070714_040000.txt');
load ('14jul07epz/vwind_0_6km/VWIND_0_6km20070714_040000.txt');
load ('14jul07epz/uwind20C/UWIND20C20070714_040000.txt');
load ('14jul07epz/vwind20C/VWIND20C20070714_040000.txt');
load ('14jul07epz/muvgp/MUVGP20070714_040000.txt');
load ('14jul07epz/muncape/MUCAPE_Normalized20070714_040000.txt');
for i=1:256
    for j=1:256
        if (MUCAPE_Normalized20070714_040000(i,j)>=1 ||
        MUCAPE_Normalized20070714_040000(i,j)<=0)
            MUCAPE_Normalized20070714_040000(i,j)=0;
        end
    end
end
load ('14jul07epz/sfcprestend/RUCSfcPresTendency20070714_040000.txt');
load ('14jul07epz/muehi/MUEHI20070714_040000.txt');
load ('14jul07epz/dcape/DCAPE20070714_040000.txt');
load ('14jul07epz/lapserate/LAPSERATE20070714_040000.txt');
load ('14jul07epz/deepshear/DEEPSHEAR20070714_040000.txt');
load ('14jul07epz/meanrh/MEANRH20070714_040000.txt');
load ('14jul07epz/sfccape/SFCCAPE20070714_040000.txt');
load ('14jul07epz/wetbulbzero/WETBULB20070714_040000.txt');
```

```

load ('14jul07epz/mucin/MUCIN20070714_040000.txt');

finalarray=0;

for e=1:numberofcells
for i=1:m
    for j=1:n
        if labeled(i,j)==e
            test(i,j)= T20070714_040001(i,j);
            echotop(i,j)= ECHOTOP20070714_040001(i,j);
            mesh(i,j)= MESH20070714_040001(i,j);
            posh(i,j)= POSH20070714_040001(i,j);
            vil(i,j)= VIL20070714_040001(i,j);
            vildensity(i,j)= VILDENSITY20070714_040001(i,j);
            mucape(i,j)=MUCAPE20070714_040000(i,j);
            srhel(i,j)=SRHelicity0_3km20070714_040000(i,j);
            vgp(i,j)=MUVGP20070714_040000(i,j);
            uwind_0_6km(i,j)=UWIND_0_6km20070714_040000(i,j);
            vwind_0_6km(i,j)=VWIND_0_6km20070714_040000(i,j);
            uwind20C(i,j)=UWIND20C20070714_040000(i,j);
            vwind20C(i,j)=VWIND20C20070714_040000(i,j);
            ncape(i,j)=MUCAPE_Normalized20070714_040000(i,j);
            sfcprestend(i,j)=RUCSfcPresTendency20070714_040000(i,j);
            ehi(i,j)=MUEHI20070714_040000(i,j);
            dcape(i,j)=DCAPE20070714_040000(i,j);
            lapserate(i,j)=LAPSERATE20070714_040000(i,j);
            deepshear(i,j)=DEEPSHEAR20070714_040000(i,j);
            meanrh(i,j)=MEANRH20070714_040000(i,j);
            sfccape(i,j)=SFCCAPE20070714_040000(i,j);
            wetbulb(i,j)=WETBULB20070714_040000(i,j);
            mucin(i,j)=MUCIN20070714_040000(i,j);
        else
            test(i,j)=0;
            echotop(i,j)= 0;
            mesh(i,j)= 0;
            posh(i,j)= 0;
            vil(i,j)= 0;
            vildensity(i,j)= 0;
            mucape(i,j)=0;
            srhel(i,j)=0;
            vgp(i,j)=0;
            uwind_0_6km(i,j)=0;
            vwind_0_6km(i,j)=0;
            uwind20C(i,j)=0;
            vwind20C(i,j)=0;
            ncape(i,j)=0;
            sfcprestend(i,j)=0;
            ehi(i,j)=0;
            dcape(i,j)=0;
            lapserate(i,j)=0;
            deepshear(i,j)=0;

```

```

        meanrh(i,j)=0;
        sfccape(i,j)=0;
        wetbulb(i,j)=0;
        mucin(i,j)=0;
    end
end
%figure;
for i=1:m
    for j=1:n
        if test(i,j)>0
            numpixelstemp(i,j)=1;
        else
            numpixelstemp(i,j)=0;
        end
    end
end
numpixelstemp2=sum(numpixelstemp);
numpixelsincell=sum(numpixelstemp2);
if numpixelsincell>20
figure;
imagesc(test);
caxis([0 60]);
colorbar;
%figure;
%imagesc(mucape);
%colorbar;
%figure
%imagesc(srhel);
%colorbar;

%find max and min axes for elipse and area
for i=1:256
    for j=1:256
        if (test(i,j)>0)
            testid(i,j)=1;
        else
            testid(i,j)=0;
        end
    end
end
%imagesc(testid);
for degree=1:180
    rotimage=rotate_image( degree, testid, [1,256;1,256]);
    %figure;
    %imagesc(rotimage)
    maxaxis(degree)=max(sum(rotimage));
end
axis1=max(maxaxis);
axis2=min(maxaxis);
eliparea=pi()*(axis1/2)*(axis2/2);

testimages=[reshape(test,m*n,1)];

```

```

echotopimages=[reshape(echotop,m*n,1)];
meshimages=[reshape(mesh,m*n,1)];
poshimages=[reshape(posh,m*n,1)];
vilimages=[reshape(vil,m*n,1)];
vildensityimages=[reshape(vildensity,m*n,1)];
mucapeimages=[reshape(mucape,m*n,1)];
srhelimages=[reshape(srhel,m*n,1)];
vgpimages=[reshape(vgp,m*n,1)];
uwind_0_6kmimages=[reshape(uwind_0_6km,m*n,1)];
vwind_0_6kmimages=[reshape(vwind_0_6km,m*n,1)];
uwind20Cimages=[reshape(uwind20C,m*n,1)];
vwind20Cimages=[reshape(vwind20C,m*n,1)];
ncapeimages=[reshape(ncape,m*n,1)];
sfcprestendimages=[reshape(sfcprestend,m*n,1)];
ehiimages=[reshape(ehi,m*n,1)];
dcapeimages=[reshape(dcape,m*n,1)];;
lapserateimages=[reshape(lapserate,m*n,1)];;
deepshearimages=[reshape(deepshear,m*n,1)];;
meanrhimages=[reshape(meanrh,m*n,1)];;
sfccapeimages=[reshape(sfccape,m*n,1)];;
wetbulbimages=[reshape(wetbulb,m*n,1)];;
mucinimages=[reshape(mucin,m*n,1)];;

for i=1:numpixelsincell
    statarray(i)=0;
    statarrayechotop(i)=0;
    statarraymesh(i)=0;
    statarrayposh(i)=0;
    statarrayvil(i)=0;
    statarrayvildensity(i)=0;
    statarraymucape(i)=0;
    statarraysrhel(i)=0;
    statarrayuwind_0_6km(i)=0;
    statarrayvwind_0_6km(i)=0;
    statarrayuwind20C(i)=0;
    statarrayvwind20C(i)=0;
    statarrayvgp(i)=0;
    statarrayncape(i)=0;
    statarraysfcprestend(i)=0;
    statarrayehi(i)=0;
    statarraydcape(i)=0;
    statarraylapserate(i)=0;
    statarraydeepshear(i)=0;
    statarraymeanrh(i)=0;
    statarraysfccape(i)=0;
    statarraywetbulb(i)=0;
    statarraymucin(i)=0;

end
j=1;
for i=1:65536
    if testimages(i)>0
        statarray(j)=statarray(j)+testimages(i);

```

```

        j=j+1;
    end

end
k=1;
for i=1:65536
    if mucapeimages(i)>0
        statarraymucape(k)=statarraymucape(k)+mucapeimages(i);
        k=k+1;
    end
end
l=1;
for i=1:65536
    if srhelimages(i)>0
        statarraysrhel(l)=statarraysrhel(l)+srhelimages(i);
        l=l+1;
    end
end
o=1;
for i=1:65536
    if uwind_0_6kmimages(i)~=0
        statarrayuwind_0_6km(o)=statarrayuwind_0_6km(o)+uwind_0_6kmimages(i);
        o=o+1;
    end
end
p=1;
for i=1:65536
    if vwind_0_6kmimages(i)~=0
        statarrayvwind_0_6km(p)=statarrayvwind_0_6km(p)+vwind_0_6kmimages(i);
        p=p+1;
    end
end
y=1;
for i=1:65536
    if uwind20Cimages(i)~=0
        statarrayuwind20C(y)=statarrayuwind20C(y)+uwind20Cimages(i);
        y=y+1;
    end
end
z=1;
for i=1:65536
    if vwind20Cimages(i)~=0
        statarrayvwind20C(z)=statarrayvwind20C(z)+vwind20Cimages(i);
        z=z+1;
    end
end
q=1;
for i=1:65536
    if vgpimages(i)>0
        statarrayvgp(q)=statarrayvgp(q)+vgpimages(i);
        q=q+1;
    end
end

```

```

r=1;
for i=1:65536
    if ncapeimages(i)>0
        statarrayncape(r)=statarrayncape(r)+ncapeimages(i);
        r=r+1;
    end
end
s=1;
for i=1:65536
    if sfcprestendimages(i)~=0
        statarraysfcprestend(s)=statarraysfcprestend(s)+sfcprestendimages(i);
        s=s+1;
    end
end
t=1;
for i=1:65536
    if ehiimages(i)>0
        statarrayehi(t)=statarrayehi(t)+ehiimages(i);
        t=t+1;
    end
end
aa=1;
for i=1:65536
    if dcapeimages(i)>0
        statarraydcape(aa)=statarraydcape(aa)+dcapeimages(i);
        aa=aa+1;
    end
end
bb=1;
for i=1:65536
    if lapsrateimages(i)>0
        statarraylapsrate(bb)=statarraylapsrate(bb)+lapsrateimages(i);
        bb=bb+1;
    end
end
cc=1;
for i=1:65536
    if deepshearimages(i)>0
        statarraydeepshear(cc)=statarraydeepshear(cc)+deepshearimages(i);
        cc=cc+1;
    end
end
dd=1;
for i=1:65536
    if meanrhimages(i)>0
        statarraymeanrh(dd)=statarraymeanrh(dd)+meanrhimages(i);
        dd=dd+1;
    end
end
ee=1;
for i=1:65536
    if sfccapeimages(i)>0
        statarraysfccape(ee)=statarraysfccape(ee)+sfccapeimages(i);
    end
end

```

```

        ee=ee+1;
    end
end
ff=1;
for i=1:65536
    if wetbulbimages(i)>0
        statarraywetbulb(ff)=statarraywetbulb(ff)+wetbulbimages(i);
        ff=ff+1;
    end
end
gg=1;
for i=1:65536
    if mucinimages(i)>0
        statarraymucin(gg)=statarraymucin(gg)+mucinimages(i);
        gg=gg+1;
    end
end
hh=1;
for i=1:65536
    if echotopimages(i)>0
        statarrayechotop(hh)=statarrayechotop(hh)+echotopimages(i);
        hh=hh+1;
    end
end
ii=1;
for i=1:65536
    if meshimages(i)>0
        statarraymesh(ii)=statarraymesh(ii)+meshimages(i);
        ii=ii+1;
    end
end
jj=1;
for i=1:65536
    if poshimages(i)>0
        statarrayposh(jj)=statarrayposh(jj)+poshimages(i);
        jj=jj+1;
    end
end
kk=1;
for i=1:65536
    if vilimages(i)>0
        statarrayvil(kk)=statarrayvil(kk)+vilimages(i);
        kk=kk+1;
    end
end
ll=1;
for i=1:65536
    if vildensityimages(i)>0
        statarrayvildensity(ll)=statarrayvildensity(ll)+vildensityimages(i);
        ll=ll+1;
    end
end
meanintensityincell=mean(statarray);

```

```

maxintensityincell=max(statarray);
minintensityincell=min(statarray);
standdevincell=std(statarray);
maxechotopincell=max(statarrayechotop);
maxmeshincell=max(statarraymesh);
maxposhincell=max(statarrayposh);
maxvilincell=max(statarrayvil);
maxvildensityincell=max(statarrayvildensity);
meanmucapeincell=mean(statarraymucape);
meansfcapeincell=mean(statarraysfcape);
meansrhelincell=mean(statarraysrhel);
meanuwind_0_6kmincell=mean(statarrayuwind_0_6km);
meanvwind_0_6kmincell=mean(statarrayvwind_0_6km);
meanuwind20Cincell=mean(statarrayuwind20C);
meanvwind20Cincell=mean(statarrayvwind20C);
meanvgpincell=mean(statarrayvgp);
maxvgpincell=max(statarrayvgp);
meanncapeincell=mean(statarrayncape);
meansfcprestendincell=mean(statarraysfcprestend);
meanehiincell=mean(statarrayehi);
meandcapeincell=mean(statarraydcape);
meanmucinincell=mean(statarraymucin);
meanlapserateincell=mean(statarraylapserate);
meandeepshearincell=mean(statarraydeepshear);
meanwetbulbincell=mean(statarraywetbulb);
meanrhincell=mean(statarraymeanrh);
ratio=axis1/axis2;

```

```

finalarrayheader=char('CellID','CellSize','MaxdBZ','MeandBZ','MindBZ','StddBZ','Echo
Top','POSH','MESH','VIL','VILDENSITY','MeanUwind(km/h)','MeanVwind(km/h)','Mean
Uwind20C(km/h)','MeanVwind20C(km/h)','MeanSRHel','MeanMUCAPE','MeanSfcCape'
,'MeanMUCIN','MeanDCAPE','MUVGP','MaxVGP','NCAPE','SFCPRESTEND','EHI','lapsera
te','deep shear','wet bulb 0 z','mean RH','majaxis','minaxis','ratio','ellipseArea','storm
type 1-linear 2-svr linear 3-pulse 4-svr pulse 5-other 6-supercell 7-line w/supercell');

finalarray(e,1)=e;
finalarray(e,2)=numpixelsincell;
finalarray(e,3)=maxintensityincell;
finalarray(e,4)=meanintensityincell;
finalarray(e,5)=minintensityincell;
finalarray(e,6)=standdevincell;
finalarray(e,7)=maxechotopincell*3280.83989501;
finalarray(e,8)=maxposhincell;
finalarray(e,9)=maxmeshincell*0.03937007874;
finalarray(e,10)=maxvilincell;
finalarray(e,11)=maxvildensityincell;
finalarray(e,12)=(meanuwind_0_6kmincell*1.852/6);
finalarray(e,13)=(meanvwind_0_6kmincell*1.852/6);
finalarray(e,14)=(meanuwind20Cincell*1.852/6);
finalarray(e,15)=(meanvwind20Cincell*1.852/6);
finalarray(e,16)=meansrhelincell;
finalarray(e,17)=meanmucapeincell;
finalarray(e,18)=meansfcapeincell;

```

```

finalarray(e,19)=meanmucinincell;
finalarray(e,20)=meandcapeincell;
finalarray(e,21)=meanvgpincell;
finalarray(e,22)=maxvgpincell;
finalarray(e,23)=meanncapeincell;
finalarray(e,24)=meansfcprestendincell*-1;
finalarray(e,25)=meanehiincell;
finalarray(e,26)=meanlapserateincell;
finalarray(e,27)=meandepshearincell;
finalarray(e,28)=meanwetbulbincell;
finalarray(e,29)=meanrhincell;
finalarray(e,30)=axis1;
finalarray(e,31)=axis2;
finalarray(e,32)=ratio;
finalarray(e,33)=eliparea;

if(ratio>3.5 && maxintensityincell<53 && numpixelsincell>=500)
    finalarray(e,34)=1;
elseif (ratio>3.5 && maxintensityincell>53 && meanvgpincell<0.2 &&
numpixelsincell>=500)
    finalarray(e,34)=2;
elseif (ratio<3.5 && numpixelsincell<500 && maxintensityincell<53)
    finalarray(e,34)=3;
elseif (ratio<3.5 && numpixelsincell<500 && maxintensityincell>53)
    finalarray(e,34)=4;
elseif (ratio<3.5 && numpixelsincell>=500 && maxintensityincell>53 &&
meanvgpincell>0.2)
    finalarray(e,34)=6;
elseif (ratio>3.5 && numpixelsincell>=500 && maxintensityincell>53 &&
meanvgpincell>0.2)
    finalarray(e,34)=7;
else
    finalarray(e,34)=5;
end

statarray=0;
statarraymucape=0;
statarraysrhel=0;
statarrayuwind_0_6km=0;
statarrayvwind_0_6km=0;
statarrayuwind20C=0;
statarrayvwind20C=0;
statarrayvgp=0;
statarrayncape=0;
statarraysfcprestend=0;
statarrayyehi=0;
statarraymucin=0;
statarraydcape=0;
statarraysfccape=0;
statarraydeepshear=0;
statarraylapserate=0;
statarraymeanrh=0;
statarraywetbulb=0;

```

```
statarrayechotop=0;  
statarraymesh=0;  
statarrayposh=0;  
statarrayvil=0;  
statarrayvildensity=0;  
end  
end
```

Appendix B: Cell Matching Matlab Script: **identifycells.m** (Lack 2007)

```
function [genimage, coords,intensities]=identifycells(tol,X)
%nx = 40 ;ny = 28
%load Sakis-Z.dat %truth
%trueimage=reshape(Sakis_Z(:,8),ny,nx)';
% [testimage truecoords trueintensities]=identifycells(20,truecastimage);
%load Sakis-yS.dat %forecast
%forecastimage=reshape(Sakis_yS(:,8),ny,nx)';
% [testimage forecastcoords forecastintensities]=identifycells(20,forecastimage);
% testimage=imread('testimage.bmp')
% testimage=identifycells(.3,testimage);
% [testimage coords]=identifycells(.3,0);
% [testimage coords]=identifycells(.3,testimage);
%close all
scrsz = get(0,'ScreenSize');
figure('Position',[1 scrsz(4) scrsz(3) scrsz(4)/2])
tmp=colormap('jet');
%tmpI=flipud(tmp);
%colormap(tmpI)
colormap(tmp)
    set(gca,'Color','w')
    set(gcf,'Color','w')

if X==0
[X1,X2] = ndgrid(-5:.2:5, -5:.2:5);
X = .5*exp(-rand(1)*(X1+1+4*rand(1)).^2 - (X2+4*rand(1)).^2)+.5*exp(-
rand(1)*(X1+rand(1)).^2 - rand(1)*5*(X2+rand(1)).^2)+.5*exp(-rand(1)*2*(X1-
3+2*rand(1)).^2 - (X2-2-rand(1)*5).^2);
end

XXX=X;
oldtol=tol;
subplot(1,2,1,'align')
imagesc(X)
caxis([0 60])
%caxis([-1 4])
%caxis([-100 400])
colorbar
%axis('image')
genimage=X;
%t1 = num2str(tol);
%S1 = strvcat('tol=',t1);
%title(S1);
minval=min(min(X));
if minval<0
    X=X+abs(minval)+.000000000001;
    tol=tol+abs(minval)+.000000000001;
    minval=.000000000001;
end
maxval=max(max(X));
```

```

if tol<minval
    tol=minval;
end
if tol>maxval
    tol=maxval-.000001;
end
[m n]=size(X);

% get rid of low intensities
for i = 1:m
    for j = 1:n
        if X(i,j)<tol
            X(i,j)=minval;
        end
    end
end
[X taggedimage]=findboundaries(tol,X);

subplot(1,2,2,'align')
imagesc(X)
caxis([0 60])
%caxis([-100 400])
colorbar
%axis('image')
%t1 = num2str(tol);
%S1 = strvcat('new tol=',t1);
%title(S1);

im=X+zeros(m,n)*min(min(X));
backApprox = blkproc(im,[15 15],'min(x(:))');
backApprox = double(backApprox)/255; % Convert image to double.
backApprox256 = imresize(backApprox, [m n], 'bilinear');
%figure, imshow(backApprox256) % Show resized background image.
im = im2double(im); % Convert I to storage class of double.
I2 = im - backApprox256;
I2 = double(max(min(I2,1),0)); % Clip the pixel values to the valid range.
%figure, imshow(I2)
I3 = imadjust(I2, [0 max(I2(:))], [0 1]); % Adjust the contrast.
bw=I3>0.2; % Make I3 binary using a threshold value of 0.2.

[labeled,numObjects] = bwlabel(bw,8);% Label components.
numObjects;

%figure
%subplot(3,1,1)
%imagesc(I3);
%colorbar
%axis('image')
%subplot(3,1,2)
%imagesc(bw)
%colorbar

```

```

%axis('image')
%subplot(3,1,3)
%map = hot(numObjects+1); % Create a colormap.
%imshow(labeled+1,map); % Offset indices to colormap by 1.
%colorbar
%axis('image')

%rect = [1 1 m n];
%grain=imcrop(labeled, rect); % Crop a portion of labeled.
grain=imfeature(labeled,'all');
allgrainsarea=[grain.Area];
allgrainscenter=[grain.Centroid];
allgrainsboundingbox=[grain.BoundingBox];
%allgrainsarea;
%[boundaryi boundaryj]=find(boundary);

%do this for all grains

[t no]=size(find(allgrainsarea>40));
%figure
count=1;
sizemat=1;
coords=zeros(numObjects*m*n,3);
intensities=zeros(numObjects,3);
labeled;
%cellintensities=zeros(m*n,1);
for i=1:numObjects
% idx = find([grain.Area]==allgrainsarea(i));
if allgrainsarea(i)>40
    Y = ismember(labeled,i);
% subplot(no,1,count)
    count=count+1;
    XX=zeros(m,n)+minval;
    for i1=1:m
        for j1=1:n
            if Y(i1,j1)==1
                XX(i1,j1)=XXX(i1,j1);
            end
        end
    end
    cellintensities=findintensities(olddtol,XX);
    intensities(count-1,1)=min(cellintensities);
    intensities(count-1,2)=mean(cellintensities);
    intensities(count-1,3)=max(cellintensities);
    [Y1 taggedimage]=findboundaries(0.1,Y);
    [i2 i1]=find([taggedimage]==2);
    r=size(i1);
    coords(sizemat:(sizemat+r-1),1)=i1;
    coords(sizemat:(sizemat+r-1),2)=-i2;
    coords(sizemat:(sizemat+r-1),3)=count-1;
    sizemat=sizemat+r;
% figure
end

```

```
% imagesc(taggedimage)
% figure
% imagesc(XX)
% colorbar
% axis('image')
% grain(i)
end
end
dlmwrite('labeled.txt',labeled,' ');
imagesc(labeled)
colorbar;
coords=coords(1:(sizemat-1),:);
intensities=intensities(1:(count-1),:);

%allgrainsarea(find(allgrainsarea>3));
```

References

- Baldwin, M.E., J.S. Kain, and S. Lakshmivarahan, 2005: Development of an Automated Classification Procedure for Rainfall Systems. *Monthly Weather Review*, **133**, 844-862.
- Bluestein, H.B., and M.H. Jain, 1985: Formation of Mesoscale Lines of Precipitation: Severe Squall Lines in Oklahoma During the Spring. *J. Atmos. Sci.*, **42**, 1711-1732.
- Breiman, L., J.H. Friedman, R.A. Olshen, and C.J. Stone, 1984: Classification and Regression Trees. Wadsworth & Brooks/Cole Advanced Books and Software, Monterey, California.
- Browning, K.A., and F.H. Ludham, 1960: Radar Analysis of a Hailstorm. Tech. Note No. 5, Contract AF61 (052)-254, Dept. of Meteorology, Imperial College, London, 109 pp.
- Bunkers, M.J., B.A. Klimowski, J.W. Zeitler, R.L. Thompson, and M.L. Weisman, 2000: Predicting Supercell Motion Using a New Hodograph Technique. *Wea. Forecasting*, **15**, 61-79.
- Burrows, W.R., 2007: Dynamical-Statistical Models for Lightning Prediction to 48-hr Over Canada and the United States. Preprints: 5th Conference on Artificial Intelligence Applications to Environmental Science, San Antonio, TX.
- Charba, J., and Y. Sasaki, 1971: Structure and Movement of the Severe Thunderstorms of 3 April 1964 as Revealed From Radar and Surface Mesonet Data Analysis. *J. Meteor. Soc. Japan*, **49**, 191-214.
- Chisholm, A.L., 1966: Small-Scale Structure of Alberta Hailstorms. M.Sc. thesis, Dept. of Meteorology, McGill University, Montreal, 73 pp.
- Corfidi, S.F., J.H. Merritt, and J.M. Fritsch, 1996: Predicting the Movement of Mesoscale Convective Complexes. *Wea. Forecasting*, **11**, 41-46.
- Dixon, M. and G. Weiner, 1993: TITAN: Thunderstorm Identification, Tracking, Analysis, and Nowcasting – A Radar-based Methodology. *Journal of Atmospheric and Oceanic Technology*, **10**, 785-797.

Finley, C.A., W.R. Cotton, and R.A. Pielke Sr., 2001: Numerical Simulation of Tornadogenesis in a High-Precipitation Supercell. Part I: Storm Evolution and Transition into a Bow Echo. *J. Atmos. Sci.*, **58**, 1597-1629.

Fovell, R.G., and P.-H. Tan, 1996: Why Multicell Storms Oscillate. *Preprints, 18th Conf. Severe Local Storms*, San Francisco, CA, Amer. Met. Soc., 186-189.

Fox, N.I., G.L. Limpert, W.T. Gilmore, J.L. Miranda, A. Schnetzler, N. Miller, A. Koleiny and S.A. Lack, 2007: The Sensitivity of Object-Based Nowcasts to Object Threshold Selection. *22nd Conference on Weather Analysis and Forecasting*, Amer. Met. Soc., Park City, UT.

_____, and J.W. Wilson, 2005: Very Short Period Quantitative Precipitation Forecasting. *Atmospheric Science Letters*, **6**, 7-11.

Jankowski, D.M., 2006: Forecasting Storm Duration Using Radar Storm Tracking. M.Sc. thesis, Dept. of Soil, Environmental, and Atmospheric Sciences, University of Missouri, 97 pp.

Johnson, J.T., P.L. Mackeen, A. Witt, E.D. Mitchell, G.J. Stumpf, M.D. Elits, and K.W. Thomas, 1998: The Storm Cell Identification and Tracking Algorithm: An Enhanced WSR-88D Algorithm. *Wea. Forecasting*, **13**, 263-276.

Lack, S.A., 2007: Cell Identification, Verification, and Classification Using Shape Analysis Techniques. D.Phil. dissertation, Dept. of Soil, Environmental, and Atmospheric Sciences, University of Missouri, 147 pp.

_____, N.I. Fox and A.C. Micheas, 2007: An Evaluation of a Procrustes Shape Analysis Verification Tool Using Idealized Cases. *22nd Conference on Weather Analysis and Forecasting*, Amer. Met. Soc., Park City, UT.

Lakshmanan, V., V. DeBrunner, and R. Rabin, 2002: Nested Partitions Using Texture Segmentation. *Southwest Symposium on Image Analysis and Interpretation*, IEEE, Santa Fe, NM.

Lindsey, D.T., and M.J. Bunkers, 2004: Observations of a Severe, Left-Moving Supercell on 4 May 2003. *Wea. Forecasting*, **20**, 15-22.

Lynn, R. and V. Lakshmanan, 2002: Virtual Radar Volumes: Creation, Algorithm Access and Visualization. *21st Conference on Severe Local Storms*, Amer. Met. Soc., San Antonio, TX.

Maddox, R.A., 1980: Mesoscale Convective Complexes. *Bull. Amer. Meteor. Soc.*, **61**, 1374-1387.

Marwitz, J.D., 1972a: The Structure and Motion of Severe Hailstorms. Part II: Multicell Storms. *J. Appl. Meteor.*, **11**, 180-188.

Micheas, A.C., N.I. Fox, S.A. Lack, and C.K. Wikle, 2007: Cell Identification and Verification of QPF Ensembles Using Shape Analysis Techniques. *Journal of Hydrology*, **343**, 105-116.

Moller, A.R., C.A. Doswell III, M.P. Foster, and G. R. Woodall, 1994: The Operational Recognition of Supercell Thunderstorm Environments and Storm Structures. *Wea. Forecasting*, **9**, 327-347.

Moncrieff, M.W., 1978: The Dynamic Structure of Two-Dimensional Steady Convection in Constant Shear. *Quart. J.Roy. Meteor. Soc.*, **104**, 543-567.

Pinto, J., C. Kessinger, B. Hendrickson, D. Megenhardt, P. Harasti, Q. Xu, P. Zhang, Q. Zhao, M. Frost, J. Cook, and S. Potts, 2007: Storm Characterization and Short Term Forecasting Using a Phased Array Radar. *33rd Conference on Radar Meteorology*, Cairns, Queensland, Australia.

Rasmussen, E.N., and J.M. Straka, 1998: Variations in Supercell Morphology. Part I. Observations of the Role of Upper-Level Storm-Relative Flow. *Mon. Wea. Rev.*, **126**, 2406-2421.